

AD-A285 331



## DOCUMENTATION PAGE

Form Approved

OMB No. 2704-0198

On a estimated to average 1 hour per response, including the time for reviewing instructions, searching existing data sources, gathering and reviewing the collection of information, sending comments regarding this burden estimate or any other aspect of this collection of information, including this burden estimate, to Washington Headquarters Services, Directorate for Information Operations and Reports, 1215 Jefferson Avenue, Washington, DC 20540-1381, and to the Office of Management and Budget, Paperwork Reduction Project (2704-0198), Washington, DC 20503.

1. AGENCY USE ONLY (Leave blank)		2. REPORT DATE September 30, 1999		3. REPORT TYPE AND DATES COVERED Final Report 1/01/92-9/30/94	
4. TITLE AND SUBTITLE Nonlinear Ocean Waves				5. FUNDING NUMBERS N00014-92-J-1274	
6. AUTHOR(S) Mark J. Ablowitz, James H. Curry, J.N. Hammock, Harvey Sequer					
7. PERFORMING ORGANIZATION NAME(S) AND ADDRESS(ES) University of Colorado, Boulder				8. PERFORMING ORGANIZATION REPORT NUMBER 153-4647	
9. SPONSORING / MONITORING AGENCY NAME(S) AND ADDRESS(ES) Office of Naval Research 800 N. Quincy Street Arlington, VA 22217-5660				10. SPONSORING / MONITORING AGENCY REPORT NUMBER	
11. SUPPLEMENTARY NOTES					
12a. DISTRIBUTION AVAILABILITY STATEMENT  <div style="border: 1px solid black; padding: 5px; text-align: center;"> <b>DISTRIBUTION STATEMENT A</b>            Approved for public release            Distribution Unlimited         </div>				12b. DISTRIBUTION CODE	
13. ABSTRACT (Maximum 200 words)  See Attached  <div style="text-align: center;">   <b>94-31492</b>  </div>					
14. SUBJECT TERMS				15. NUMBER OF PAGES	
				16. PRICE CODE	
17. SECURITY CLASSIFICATION OF REPORT		18. SECURITY CLASSIFICATION OF THIS PAGE		19. SECURITY CLASSIFICATION OF ABSTRACT	
				20. LIMITATION OF ABSTRACT	

**Abstract:**

The dynamics of waves in deep water and in shallow water are quite different. In shallow water, we have shown experimentally the existence of a family of finite-amplitude waves that propagate practically without change of form in shallow water of uniform depth. The surface patterns of these waves are genuinely two-dimensional, and periodic. The waves are easy to generate experimentally, and they seem to be stable to perturbations. They are described with reasonable accuracy by an 8-parameter family of exact solutions of the Kadomtsev-Petviashvili equation.

The situation is quite different in deep water, where much of our knowledge is based on numerical simulations. An approximate model of one-dimensional, nearly monochromatic waves in deep water is the nonlinear Schrödinger equation. We find that for certain ranges of parameters in initial data, numerical solutions of the equation are so unstable that long-time simulations of the equation are not reproducible, and are quite unreliable. The equation is integrable, and not chaotic, but numerical simulations of the equation are chaotic. We call this "numerically induced chaos".

Accession No.	
1713	✓
2112	
1713	
2112	
See ADA274651	
Dist.	
A-1	

## Nonlinear Ocean Waves

Final report: 1/1/92 - 9/30/94

The scientific study of water waves dates back to the works of Newton, the Bernoullis, and Euler, but the observations and speculations of ancient mariners long preceded these works. The mathematical problem of inviscid water waves was first posed properly by Stokes (1845; see Stoker, 1957, p. 16). Stokes' equations are nonlinear, but Stokes also linearized his equations and found both linear and weakly nonlinear approximate solutions, for waves of small amplitude. Nekrassov (1921) and Levi-Civita (1925) showed that Stokes' approximate solutions represent exact solutions of the nonlinear problem.

Stokes' small-amplitude solutions notwithstanding, nonlinearity plays an essential role in the dynamics of almost all water waves. In shallow water, waves have wavelengths longer than the mean depth of the fluid, and nonlinearity leads either to wavebreaking (Airy, 1845) or to the formation of solitary waves (Russell, 1838, 1844). In deep water, waves have wavelengths shorter than the mean depth of the fluid, and Benjamin & Feir (1967) showed that the plane waves studied by Stokes and others are subject to a nonlinear instability. Thus, nonlinearity plays an essential role in the formation of almost all waves that are observed in the ocean, no matter what their wavelengths.

During the nearly three-year duration of this grant, four principal investigators (Mark Ablowitz, James Curry, Joe Hammack, Harvey Segur) and their colleagues have studied aspects of nonlinear water waves, in both shallow and deep water. Phenomena in deep water differ significantly from those in shallow water, and our studies in these two areas are distinct. These studies combine mathematical analysis, laboratory experiments, numerical computation, and field observations. In this report, we summarize our major published conclusions, and we outline briefly the current status of work in progress.

### A. Shallow water

#### 1. Published work

The focus of our work has been on spatially periodic waves of permanent form that appear to be stable in shallow water. A full discussion on this work, which will appear in *the Journal of Fluid Mechanics*, can be found in Appendix A of this report. Our main conclusions are as follows.

- Laboratory experiments demonstrate the existence of a family of gravity-induced, finite-amplitude water waves that propagate practically without change of form in shallow water of uniform depth. The surface patterns of these waves are genuinely two-dimensional, and periodic. The basic template of a wave is hexagonal, with six wave crests forming the boundary of a cell that repeats itself over and over on the water's surface. Figure 1 shows overhead photographs of two such hexagonal patterns. These waves are easy to generate in the laboratory, and they seem to be stable to perturbations.

- A nonlinear partial differential equation due to Kadomtsev & Petviashvili (1970),

$$\partial_x(\partial_t u + 6 u \partial_x u + \partial_x^3 u) + 3 \partial_y^2 u = 0, \quad (\text{KP})$$

is known to describe approximately the evolution of waves in shallow water. The equation is completely integrable, and Krichever (1977) showed that it admits huge families of exact solutions, including an eight-parameter family of solutions (called "genus 2 solutions") that are spatially periodic and have permanent form. Segur & Finkel (1985) conjectured that this family of KP solutions ought to describe all spatially periodic waves of permanent form in shallow water of uniform depth. Our experimental results support that conjecture. We have developed an algorithm to find the eight parameters of the KP solution that best fits given wave-gauge measurements for a spatially periodic wave of permanent form. For every experiment we ran, the KP solution so obtained described the measured waves with reasonable accuracy, even when the waves violated some of the hypotheses underlying KP theory. As an example, Figure 2 shows the contour lines of a KP solution of genus 2 superposed on the overhead photographs of an observed periodic waves in shallow water. As a second example, Figure 3 shows twenty seconds of data from an array of nine wave gauges, measuring the surface displacements of a spatially periodic wave of permanent form as it swept by the gauges. Also shown in Figure 3 are the corresponding surface displacements predicted by the KP solution of genus 2 that best fits these data. Both figures show good agreement everywhere, but not perfect agreement. The reader can find more information about this study in Appendix A.

## 2. Work in progress

### (i) *Obliquely reflected waves*

The waves shown in Figures 1-3 were created with a specially designed, complicated, segmented paddle at the Waterways Experiment Station in Vicksburg, MI (see Scheffner, 1988, for a description of the experimental facility there). The complexity of this facility makes one wonder if the waves require so much complexity for their generation, or if simpler mechanisms might also produce spatially periodic waves of permanent form.

Figure 4 suggests another mechanism to produce these waves. The figure is a mosaic of two simultaneous, overhead photographs of the water's surface, illuminated by a light shining towards the wavemaker. In the figure, a train of nonlinear plane waves (*i.e.*, a cnoidal wavetrain) entering the picture from the upper left, and reflects obliquely off a straight vertical wall on the far right. The incident and reflected waves interact to produce a two-dimensional wave-pattern that is spatially periodic (over a limited spatial region) and that propagates along the wall with little apparent change of form. Because oblique reflections of plane waves are common, such a mechanism would suggest that stationary, hexagonal wavepatterns like those shown in Figures 1-3 might also be common.

With this mechanism, the incoming cnoidal wave should determine the outgoing hexagonal wave, and one should be able to deduce of the parameters of the outgoing wave from those of the incoming wave. One would also like an estimate of how much distance down the wall is required for this transformation from (incoming) cnoidal waves to (outgoing) hexagonal waves.

Detailed analysis of the wave-records for the waves shown in Figure 4 indicate that the hexagonal waves observed in the figure are slowly evolving as they propagate along the wall. [This evolution is not obvious in the figure, but it can be seen in the corresponding wave-records.] Apparently the test section in the experiment shown in the figure is not long enough for the waves to reach a steady state. Plans to repeat these experiments in a different, simpler but longer facility are now under way. (See (iv) below.)

### (ii) *Analysis of ocean data*

The KP equation predicts the existence of spatially periodic waves of permanent form in shallow water of uniform depth, and laboratory experiments show reasonably good agreement with these predictions. However, neither of these statements necessarily implies that waves like these occur in real oceans. For this, one needs actual oceanic measurements. Fortunately, oceanographers at the U.S. Army Engineer Field Research Facility (FRF) in Duck N.C. have

spent several years measuring, recording and cataloguing the waves incident on their relatively flat beach. Among their data are measurements from an array of eight gauges, located about 915 m. offshore, in about 8 m. of water.

In July, 1994, we went to FRF in search of wave-records showing spatially periodic waves of permanent form. Analysis of the data is still in progress, but the first comparison is shown in Figure 5. [We are grateful to Dr. Chuck Long of FRF for allowing us to use his data for these comparisons.] The figure shows the surface displacements measured at eight gauge locations, with about 100 seconds of data at each gauge. Also shown are the predictions of the best KP solution for these data. The agreement is not perfect, and it is worse than that for the laboratory experiments. In particular, the KP solution seems to get the phase information about right, but it consistently underestimates the peak amplitudes.

Even so, we find the results in Figure 5 quite encouraging. These are actual ocean waves, measured in the field, with no averaging of wave-records. Figure 5 shows that a single KP solution of genus 2 simultaneously approximates the data from all eight gauges with reasonable accuracy. The comparison suggests that a comparatively simple model might explain some of the complex wave patterns observed nearshore. This work is continuing.

### (iii) *Waves of genus 3*

All of our work in shallow water to date has involved spatially periodic waves of permanent form, approximated by KP solutions of genus 2. However, the KP equation is integrable, so it also admits more complicated solutions. In particular, Krichever (1977) showed that the equation admits explicit, quasiperiodic solutions of any (integer) genus. A solution of genus  $N$  represents a quasiperiodic function with  $N$  independent phases. For  $N \geq 3$ , these solutions are typically unsteady in every coordinate system, so they ought to provide interesting predictions about the time-dependent dynamics of nonlinearly interacting waves in shallow water.

In practice, a KP solution of genus  $N$  is defined by an  $N$ -fold, nested Fourier series, and just calculating the solutions efficiently is nontrivial. In fact, no general algorithm is known that enables one to truncate the  $N$ -fold series to within a predetermined bound on the truncation error. A more complicated problem is to infer the parameters of the KP solution from given measurements of the wave. Bobenko & Bordag (1989) have developed a numerically efficient procedure to calculate these series for certain ranges of the parameters. Whether their procedure works over the entire range of parameters is much less clear. We have developed an alternative

procedure for waves of genus 3, which is based on earlier work of Dubrovin (1981), and which we are now implementing numerically. The disadvantage of our procedure is that it is restricted to waves of genus 1, 2 or 3, while that of Bobenko & Bordag is not so restricted. Its advantages are that it provides rigorous bounds on truncation errors, and that it computes the KP solution with as few terms as possible. A more comprehensive comparison of the two procedures awaits the completion of the numerical code for our procedure.

(iv) *Experimental work*

An 8-axis wavemaker control and power system has been configured, purchased, and integrated. The system comprises:

- (1) 8 brushless DC motor/drive packages, each capable of a continuous torque of 14.2 oz.in. at speeds up to 175 rev/s; and
- (2) a Programmable Multi-Axis Controller (PMAC) from Delta Tau Systems. The controller is a state-of-the-art system that exploits DSP (digital signal processor) technology to obtain a significant improvement in motion-control over traditional servo-controllers.

Commanded motion profiles for each axis can be calculated within the PMAC, which has a sophisticated real-time multi-tasking operating system, or they can be loaded into its dual-ported memory along a VME bus. The controller uses encoder feedback from each motor to obtain the instantaneous position, velocity and acceleration of each axis's motion. This information is used in on-the-fly computations to command the motor for the next profile move.

The 8-axis motion control will be used to drive eight piston-type wavemakers in an existing laboratory basin. (The mechanical wavemaker apparatus is still under development.) The need for this new facility is twofold. First, the large facility at the U.S. Army Coastal Engineering Research Center (Vicksburg, MS) is no longer available. Second, the high degree of control enables us to scale the experiments down in size so that more flexibility is permitted in planning and changing experiments (at much lower costs). Moreover, the smaller scale will enable us to use an existing high-speed imaging system that measures the time evolution of the water surface topography. These measurements are particularly important for investigating 2-D water-wave theories such as the KP equation.

The first set of experiments planned for the new wavemaker system involve oblique reflections of plane waves, as discussed above. The second set of experiments planned involve investigations of KP solutions of genus 3, also discussed above. Because KP solutions of genus 3 do not have permanent form, the surface imaging measurements will be particularly useful for comparing with KP theory.

## **B. Deep water**

### **1. Published work**

Numerical simulations provide much of the current knowledge of the dynamics of waves in deep water. Consequently, we have focussed our attention to date on the reliability of numerical simulations. Our work has appeared in five published papers:

- (i) Ablowitz, M.J., Schober, C.M. and Herbst, B. *Phys. Rev. Lett.*, **71**, pp. 2683-2686, 1993.
- (ii) Ablowitz, M.J. and Schober, C.M. "Effective Chaos in the Nonlinear Schrödinger Equation" in *Contemporary Mathematics* **172**, Eds. P.Kloeden and J.Palmer, AMS 1994.
- (iii) Ablowitz, M.J. and Schober, C.M. "Hamiltonian Integrators for the Nonlinear Schroedinger Equation" in Computational Physics, Ed. J. Potvin, 1994.
- (iv) Ablowitz, M.J. and Schober, C.M. "Numerical Stochasticity, Hamiltonian Integrators and the Nonlinear Schroedinger Equation", in the Three Dimensional Dynamical Systems Workshop, Ed. Dr.Kandrup, N. Y. Academy of Sciences, 1993.
- (v) Ablowitz, M.J. and C.M. Schober, "Homoclinic Manifolds and Numerical Chaos in the Nonlinear Schroedinger Equation", in Math. and Computers in Simulation on Nonlinear Wavelike Eq'ns, Eds. Vichnevelsky, Taha, Newel. Elsevier Science, 1993.

The first of these is included in this report as Appendix B. Our main results are the following.

- The (focussing) nonlinear Schrödinger equation in one spatial dimension,

$$i\partial_t A + \partial_x^2 A + 2 |A|^2 A = 0, \quad (\text{NLS})$$

arises in several physical contexts, including as an approximate evolution equation for the complex envelope of one-dimensional, nearly monochromatic waves in deep water (Zakharov, 1968). The equation is known to be integrable (Zakharov & Shabat, 1972), so its solutions are not chaotic.

- Even so, for certain parameter ranges of the initial data, small errors on the order of roundoff (*i.e.*,  $10^{-16}$ ) grow rapidly in numerical simulations and saturate at values comparable to the main wave. Because NLS is integrable, it admits several constants of motion, and these constants are preserved to a very high accuracy during the simulations. Thus, the growth of these numerical errors cannot be attributed to standard problems like inadequate numerical resolution or poor time-integration strategies.



- Instead, the numerical errors grow because of a phase instability in the numerical simulations. The instability is associated with homoclinic solutions nearby the computed solution. Similar instabilities occur in other integrable equations that admit homoclinic solutions (*e.g.*, focussing mKdV, sine-Gordon), but not in integrable equations that admit no homoclinic solutions (*e.g.*, defocussing NLS, defocussing mKdV, KdV, KP).

- The instability leads to chaotic behaviour in the numerical simulations, so one observes "numerically induced chaos". In other words, even if NLS itself is not chaotic, a perturbed NLS equation is chaotic, and tiny numerical errors produce enough chaos to completely change the character of the solution. This example demonstrates the danger of inferring that a Hamiltonian dynamical system is chaotic on the basis of numerical simulations of the system.

- To relate these results to problems in water waves, we note that the sign difference between focussing and defocussing NLS is the sign difference that determines whether or not the Benjamin-Feir instability is operative. Thus, we would expect numerically-induced chaos in numerical simulations of waves in deep water, but not for waves in shallow water.

## 2. *Work in progress*

For focussing NLS, by changing a parameter ( $M$ ) in the initial data we can excite an arbitrary number of linearly unstable modes. When  $M=2-3$  we have observed that at intermediate values of the mesh size, the standard numerical schemes break down and develop a serious spatial and temporal chaotic response (Herbst & Ablowitz, 1989, Ablowitz & Herbst, 1993). However, we have developed an algorithm that is based upon the Inverse Scattering Transform and that we call the integrable discrete NLS equation or IDNLS, which is fast and effective. In this parameter regime the IDNLS scheme does not show any signs of the joint spatial-temporal chaos that exists in the standard schemes. When the mesh is sufficiently refined, the standard schemes eventually converge to the same values as those obtained via the IDNLS scheme, although they require considerably finer mesh size.

When the number of unstable modes is larger, *e.g.*  $M=6-8$ , we have found that the numerical simulations over moderate time intervals are extremely sensitive. It is difficult to compute accurate solutions even though we use an extremely refined mesh and our numerical algorithm accurately preserves the underlying constants of motion (Ablowitz, Herbst & Schober, 1993). We find that numerical instabilities and chaos are excited even by tiny errors on

the order of roundoff. The reason is that the initial data in this parameter regime is extremely close to the homoclinic manifolds of the NLS equation. In order to show this, one needs to analyze carefully the inverse spectral theory associated with the NLS equation (Ablowitz & Schober, 1993). Perturbations in the neighborhood of homoclinic manifolds allows frequent homoclinic crossings and the ensuing chaotic dynamics. On the other hand, when we consider the defocusing NLS equation, theory tells us that there is no linear instability of the basic wavetrain and there are no associated homoclinic manifolds. In this case our numerical algorithms work well and there is no indication of a chaotic response.

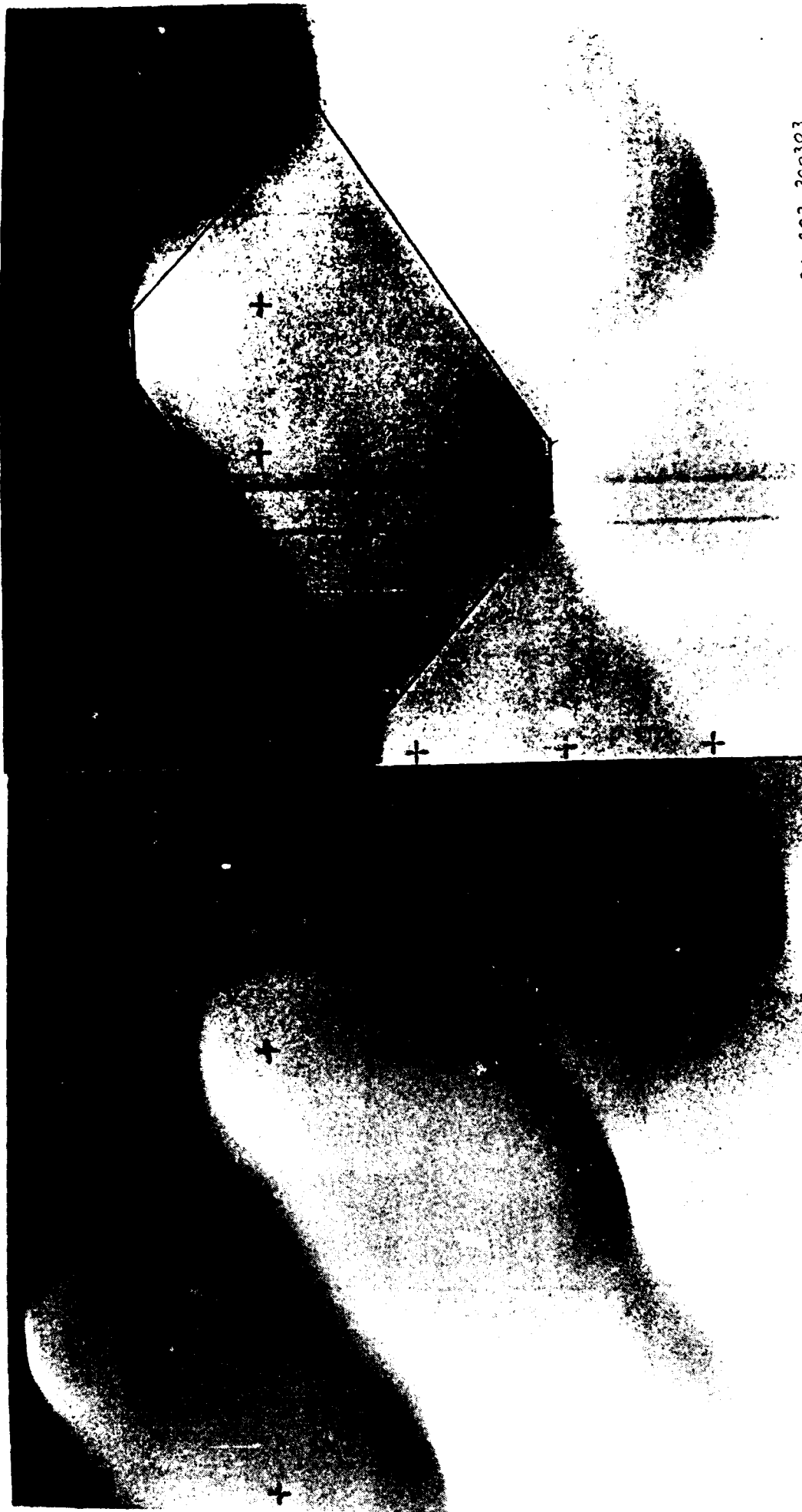
### References

- Ablowitz, M.J., B.M. Herbst, & C. Schober, *Phys. Rev. Lett.* **71**, pp. 2683-2686, 1993
- Ablowitz, M.J. & B.M. Herbst, *SIAM J. Applied Math.* **50**, p. 339, 1990
- Ablowitz, M.J. & B.M. Herbst, in Important Developments in Soliton Theory, Eds. A.S. Fokas and V.E. Zakharov, Series in Nonlinear Dynamics, Springer-Verlag, Berlin, 1993
- Ablowitz, M.J. & C.M. Schober, "Effective Chaos in the NLS Equation, *Contemp. Math.*, **172**, Eds. P.Kloeden and J.Palmer, AMS 1994
- Ablowitz, M.J. and Schober, C.M. "Hamiltonian Integrators for the NLS Equation" in Computational Physics, Ed. J. Potvin, 1994.
- Ablowitz, M.J. and Schober, C.M. "Numerical Stochasticity, Hamiltonian Integrators and the NLS Equation", in the 3-D Dynamical Systems Workshop". Ed. Dr.Kandrup, N. Y. Academy of Sciences, 1993.
- Ablowitz, M.J. and Schober, C.M. "Homoclinic Manifolds and Numerical Chaos in the NLS Equation", in Math. and Computers in Simulation on Nonlinear Wavelike Eq'ns, Eds. Vichnevelsky, Taha, Newel. Elsevier Science, 1993.
- Airy, G.B., *Tides and Waves*, Encyclopedia Metropolitana, **5**, pp. 241-396, 1845
- Benjamin, T. B. & J.F. Feir, *J. Fluid Mech.*, **27**, pp. 417-430, 1967
- Bobenko, A.I. & L.A. Bordag, *J. Phys. A: Math. Gen.* **22**, pp. 1259-1274, 1989
- Dubrovin, B.A., *Russ. Math. Surveys*, **36**, pp. 11-92, 1981
- Ercolani, N., M.G. Forest, & D.W. McLaughlin, *Physica D* **43**, p. 349, 1990
- Herbst, B.M. & M.J. Ablowitz, *Phys. Rev. Lett.*, **62**, p. 2065, 1989
- Kadomtsev, B.B. & V.I. Petviashvili, *Sov. Phys. Doklady*, **15**, pp. 539-541, 1970

- Krichever, I.M., *Russ. Math. Surveys*, **32**, pp. 185-213, 1977  
 Levi-Civita, T., *Math. Annalen*, **93**, pp. 264-314, 1925  
 Nekrassov, A.I., *Izv. Ivanovo-Vosnesensk. Politekh. In-ta*, **3**, 1921  
 Russell, J.S., *Report of the committee on waves*, 7th meeting of British Ass'n for Advancement of Science, pp. 417-496, 1838  
 Russell, J.S. *Report on waves*, 14th meeting of British Ass'n for Advancement of Science, pp. 311-390, 1844  
 Scheffner, N.W., *Misc. Paper CERC-88-4*, U.S. Army Engineer Waterways Experiment Station, Vicksburg, MS, 1988  
 Segur, H. & A. Finkel, *Stud. App. Math.*, **73**, pp. 183-220, 1985  
 Stoker, J.J., *Water Waves*, Wiley Interscience, Inc. N.Y., 1957  
 Zakharov, V.E., *Sov. Phys. J. Appl. Mech. Tech. Phys.*, **4**, pp. 190-194, 1968  
 Zakharov, V.E. & A.B. Shabat, *Sov. Phys. JETP*, **34**, pp. 62-69, 1972

### Figure Captions

- Figure 1. Mosaic of two overhead photographs, showing surface patterns of waves in shallow water. Experiment: (a) KP400203-300303; (b) KP220203-110403. Each of these wave patterns has a basic hexagonal template; one such template is shown in Figure 1a.
- Figure 2. For experiment KP220203-110403, contour lines of the best KP solution are superimposed on the photograph shown in Figure 1b. The direction of propagation of the entire pattern is also shown.
- Figure 3. Detailed comparison of measured wave records with the best KP solution, for 20 seconds of data from experiment KP220203-110403.
- Figure 4. Mosaic of two overhead photographs, showing a cnoidal wavetrain from the upper left impinging obliquely on a vertical wall at the far right. The incident and reflected waves interact to produce a hexagonal wave pattern that has nearly permanent form as it propagates along the wall towards the bottom of the photo.
- Figure 5. This figure shows 105 seconds of data, measured on 23 September, 1990 at 8 wave gauges situated in 8 m. of water offshore of FRF in Duck, N.C. Also shown superposed on these data are the predictions of a KP solution of genus 2. The KP solution was chosen to fit the data, and this solution is compared to the data from all 8 gauges simultaneously.



KP 40203-300303

Figure 1a

KP220203-110403

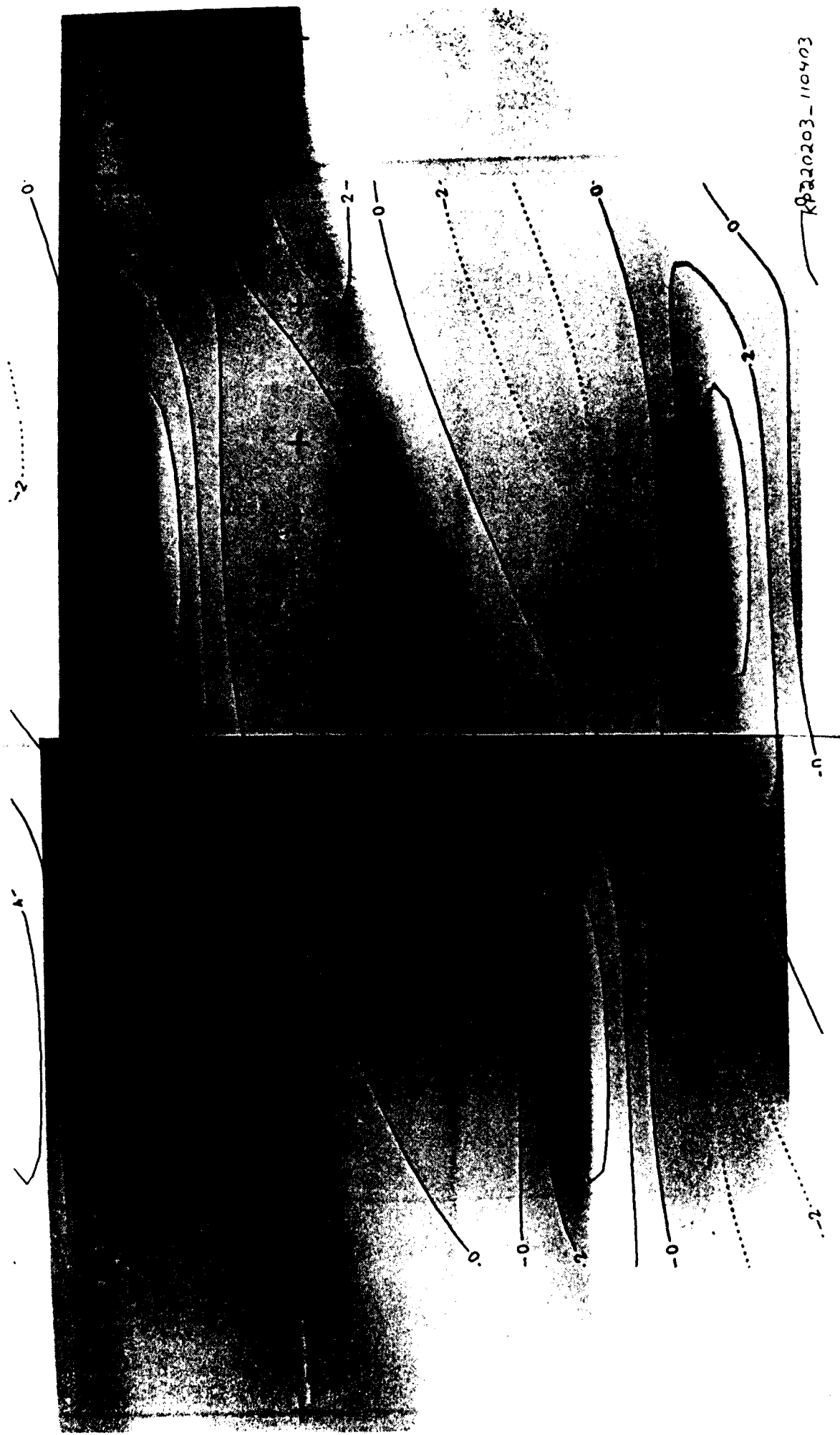


Figure 2 - KP220203\_110403

KP220203\_110403

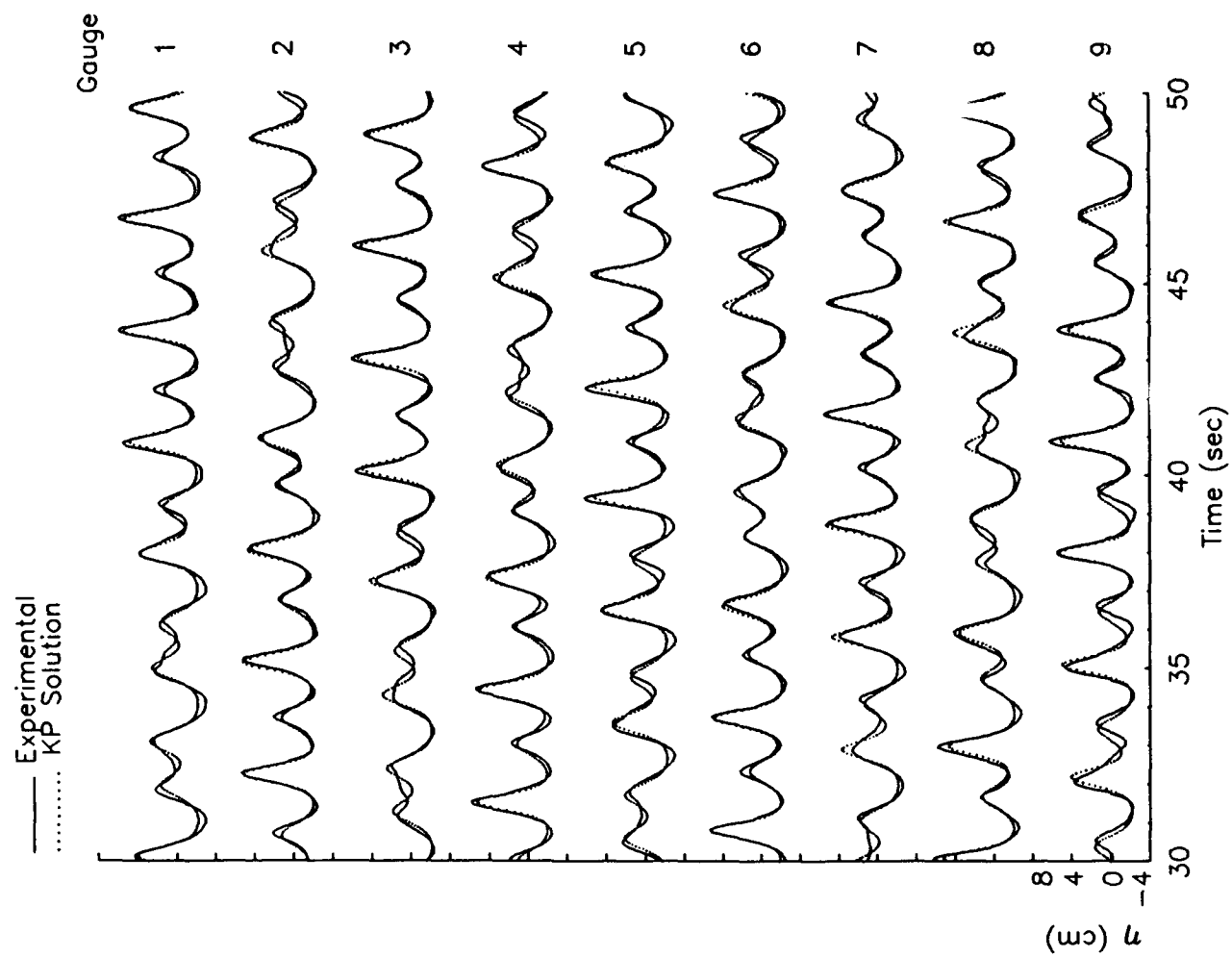


Figure 3

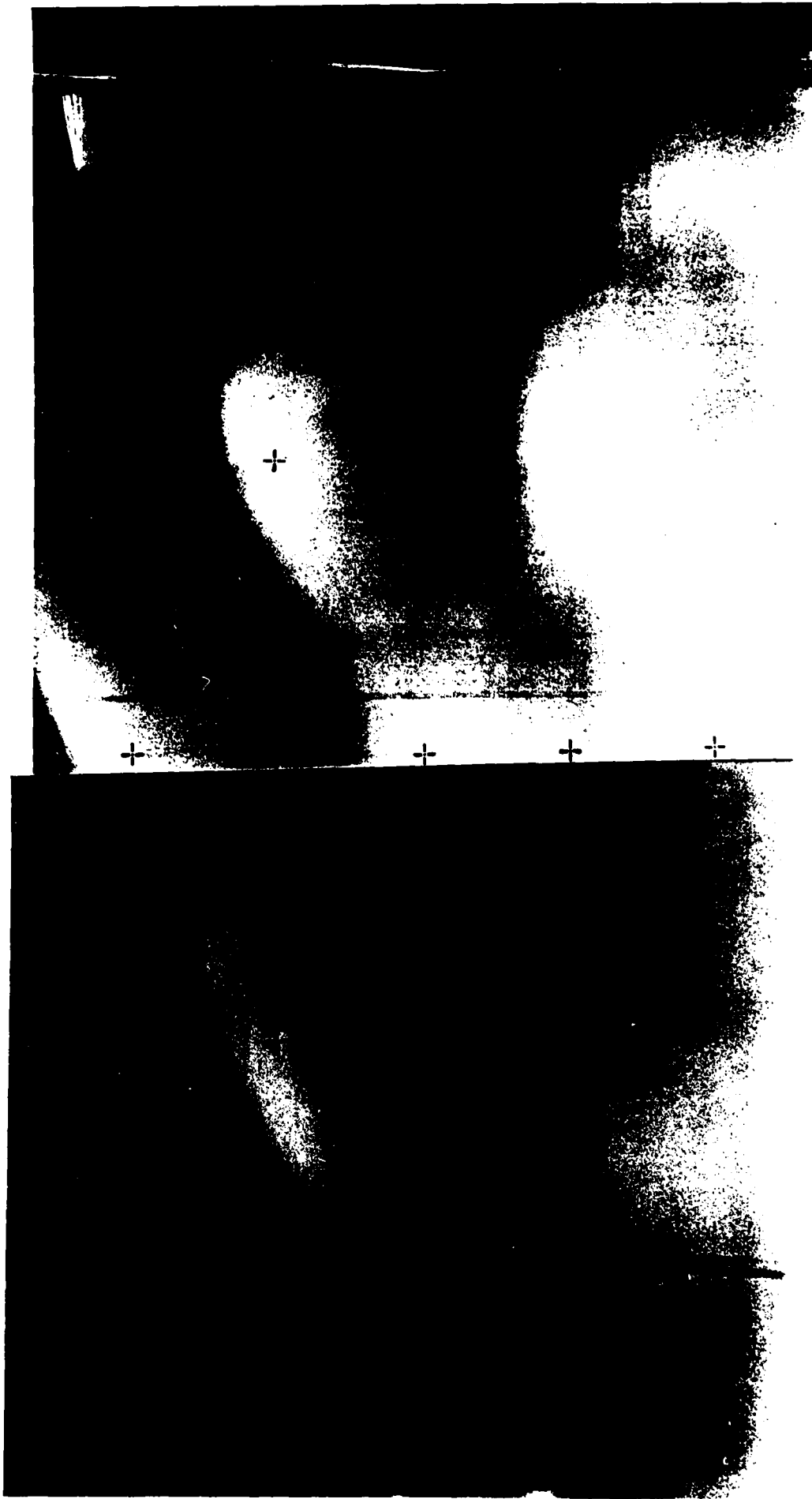
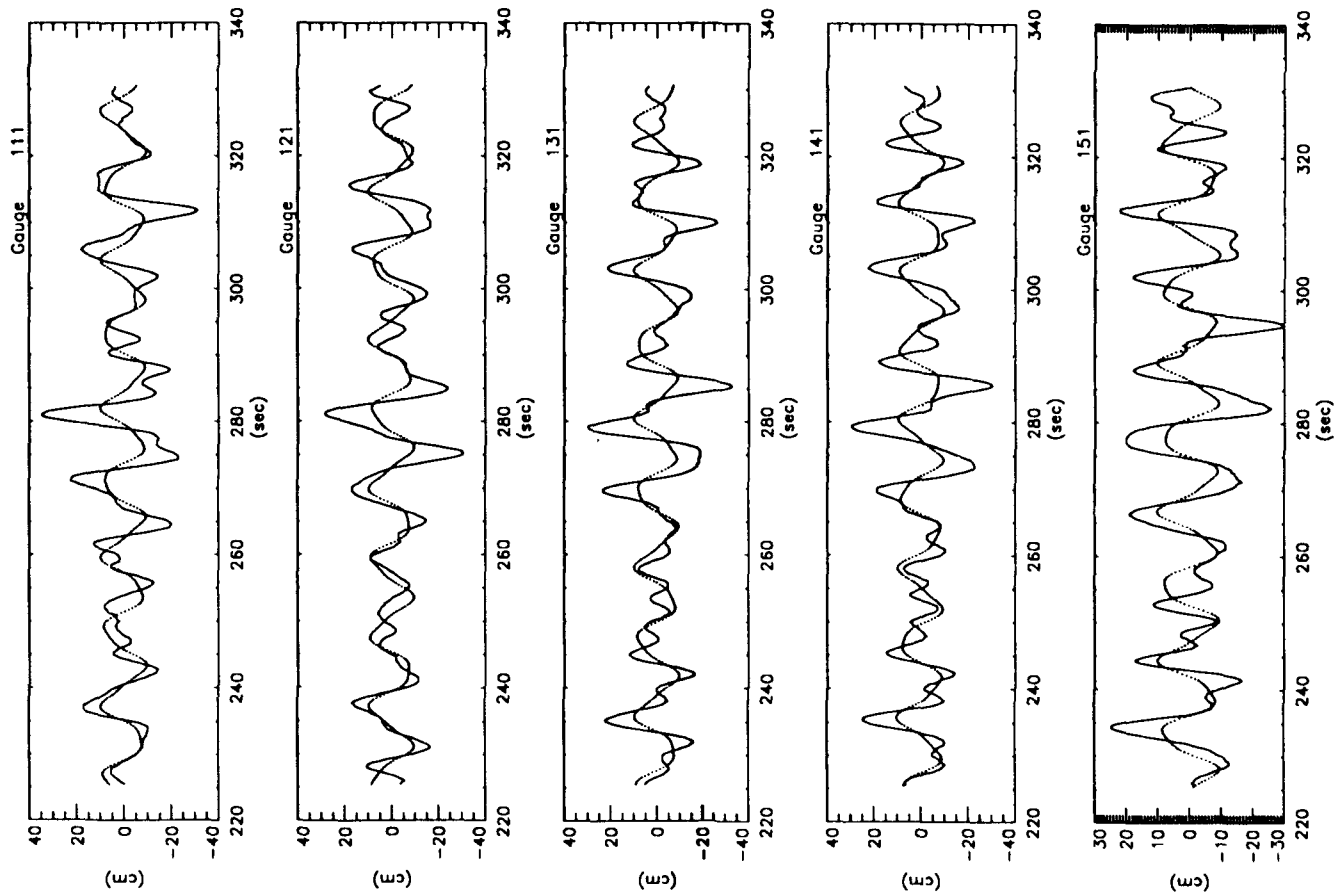


Figure 4

CN38.50204R





$b$	$= -8.60$	$\mu_1$	$= 0.528$	$\mu_2$	$= 1.300$
$\lambda$	$= 0.071$	$\nu_1$	$= 0.305$	$\nu_2$	$= -1.366$
$d$	$= -15.94$	$\omega_1$	$= 0.383$	$\omega_2$	$= -2.115$
$\sigma$	$= 0.85t$				
$f_{\max}/u_{\max}$	$= 0.293$				
				Experimental	Asymmetric KP Solution

23sep9010

Figure 5

## **Appendix A**

### **Two-dimensional periodic waves in shallow water Part 2: Asymmetric waves**

**by Joe Hammack, Daryl McCallister,  
Norman Scheffner, and Harvey Segur**

**to appear in *the Journal of Fluid Mechanics***

# **Two-dimensional periodic waves in shallow water**

## **Part 2: Asymmetric waves**

by Joe Hammack<sup>1</sup>, Daryl McCallister<sup>2</sup>,  
Norman Scheffner<sup>3</sup>, and Harvey Segur<sup>2</sup>

<sup>1</sup> Departments of Geosciences and Mathematics,  
Penn State University, University Park, PA 16802

<sup>2</sup> Program in Applied Mathematics, University of Colorado  
Boulder, CO 80309-0526

<sup>3</sup> US Army Engineer Waterways Experiment Station,  
Coastal Engineering Research Center, Vicksburg, MS 39180

### ***Abstract:***

We demonstrate experimentally the existence of a family of gravity-induced, finite-amplitude water waves that propagate practically without change of form in shallow water of uniform depth. The surface patterns of these waves are genuinely two-dimensional, and periodic. The basic template of a wave is hexagonal, but it need not be symmetric about the direction of propagation, as required in our previous studies (*e.g.*, Hammack *et al.*, 1989). Like the symmetric waves in earlier studies, the asymmetric waves studied here are easy to generate, they seem to be stable to perturbations, and their amplitudes need not be small. The Kadomtsev-Petviashvili (KP) equation is known to describe approximately the evolution of waves in shallow water, and an eight-parameter family of exact solutions of this equation ought to describe almost all spatially periodic waves of permanent form. We present an algorithm to obtain the eight parameters from wave-gauge measurements. The resulting KP solutions are observed to describe the measured waves with reasonable accuracy, even outside the putative range of validity of the KP model.

## 1. Introduction:

An earlier paper by Hammack, Scheffner & Segur (1989, hereinafter called *Part 1*) reported an experimental study of gravity-induced waves that propagate practically without change of form in shallow water of uniform depth. Those waves had finite amplitudes, and their surface patterns were periodic in two spatial dimensions and in time. The spatial pattern of the waves was a hexagon that was symmetric about the direction of wave propagation. The waves were predicted with reasonable accuracy by a family of exact solutions of an equation due to Kadomtsev and Petviashvili (1970):

$$(f_t + 6 ff_x + f_{xxx})_x + 3f_{yy} = 0, \quad (\text{KP})$$

where subscripts denote partial derivatives. In a second set of experiments (Hammack, Scheffner & Segur, 1991), more effort was made to reduce depth-variations in the laboratory basin, and the theoretical-experimental agreement improved further. Both of these studies were preceded by Peregrine (1985), who also observed hexagon-like waves of permanent form but who argued against that interpretation.

Within the KP equation, almost all real-valued, spatially periodic waves of permanent form are characterized by a family of exact solutions with eight free parameters: six dynamic parameters associated with wavelengths and wave amplitudes, plus two arbitrary phases (*cf.* Segur & Finkel, 1985). Typically, these waves have asymmetric surface patterns. The two experimental papers cited above tested only a subset of these waves, called *symmetric* waves, which have only  $(3 + 2)$  parameters. Figure 1 shows photographs of both symmetric and asymmetric water waves.

In this paper, we describe an experimental study of two-dimensional, spatially periodic, *asymmetric* waves that propagate practically without change of form in shallow water of uniform depth. [In the terminology used in this paper, surface waves are either "one-dimensional" or "two-dimensional", depending on the nature of their surface patterns. The velocity fields associated with the waves are one dimension higher.] Our three main results for asymmetric waves are consistent with our earlier results for symmetric waves:

- 1) In shallow water of uniform depth, there exist spatially periodic waves with finite amplitudes and fully two-dimensional surface patterns. These waves are easy to generate, they propagate with nearly permanent form, and they seem to be stable with respect to perturbations in initial conditions and to weak external forcing (*e.g.*,

due to viscosity or to variations in bottom depth). The amplitudes of the waves need not be small.

2) The basic template of the two-dimensional wave pattern is a six-sided figure (*i.e.*, a hexagon), with a broad, flat trough surrounded by six narrow wave crests (*e.g.*, see Figure 1). Wave crests opposite each other in this hexagon are parallel, they are equal in length and in wave amplitude, and they can be identified with each other in order to reproduce the periodic pattern.

3) Over the range of parameter values that we tested, these water waves are predicted with reasonable accuracy by the full, eight-parameter family of KP solutions of genus 2. This range extends well beyond the putative range of validity of the KP equation as an approximate model of waves in shallow water (*i.e.*, beyond the range of nearly one-dimensional waves of small amplitude in shallow water). In this sense, the KP model provides a convenient means to learn about hexagonal waves of permanent form, but their mathematical existence and stability seem to be independent of the KP model.

Our primary objective in this study is to establish experimentally the existence and properties of asymmetric hexagonal waves of permanent form in shallow water of uniform depth. To this end, we present the results of fifteen experiments, which exhibit some of the variety of waves of this form. Our secondary objective is to determine how accurately the full, eight-parameter family of KP solutions of genus 2 describe the measured waves. To this end, we present an algorithm that uses measurements from an array of wave-gauges to obtain the eight parameters of the KP solution that "best" fit the measured waves. By design, the algorithm uses only wave-gauge measurements (ignoring the known data used to program the wavemaker) so that it can be applied to gauge-array data in more complex wave environments in the laboratory and in the field. Fifteen experiments are far too few to determine the parameter range for KP theory to be applicable, and our experiments were not chosen with that objective in mind. In fact, most of our experiments have parameters that lie outside the putative range of validity of KP theory. (Some of our waves have near-breaking heights and strongly two-dimensional surface patterns.) We reiterate our belief that the KP model is convenient but not essential to describe periodic waves of permanent form in shallow water.

A summary of the contents of this paper is as follows. In §2, we review the main ideas needed to compare KP solutions of genus 2 with experimental data on waves in shallow water. We describe experimental procedures and results in §3. The procedures are

similar to those used in Part 1, but the experimental data here are more complicated. The main theoretical problem addressed in this paper is the following. Given wave-gauge data from a particular experiment, find the eight parameters of the KP solution of genus 2 that best fits these data. We present an algorithm to solve this problem in an Appendix to the paper, and we use the algorithm in §4 to compare KP theory with the results of fifteen different experiments. In a sense, our procedure can be viewed as a complicated form of surface-fitting (*i.e.*, two-dimensional curve-fitting), with no demonstrated predictive power. However, we recorded more data than we used to find the KP solution, and in §4 we also test the accuracy of some concrete predictions of the theory. The hexagonal waves studied in this paper and in part 1 seem to be the simplest nontrivial waves of permanent form that are periodic and two-dimensional in shallow water. This identification suggests that they ought to occur frequently in natural oceanic settings. In §5, we present some observations of oceanic waves similar to those discussed in this paper.

## 2. Review of KP theory

The KP equation,

$$(f_t + 6ff_x + f_{xxx})_x + 3f_{yy} = 0, \quad (\text{KP})$$

describes approximately the slow evolution of gravity-induced waves on water of uniform depth when the waves are assumed: (i) to have horizontal lengthscales much longer than the fluid depth (this assumption is also called "shallow water"); (ii) to propagate primarily in one direction (the  $x$ -direction), with only weak variations in the transverse  $y$ -direction; and (iii) to have small-to-moderate amplitudes. The KP equation is not well-posed as it stands ( $f \equiv 0$  and  $f = t$  both solve KP, and they coincide at  $t = 0$ ), and one must interpret  $\{\partial_x^{-1}\}$  in order to integrate (KP) in time. All of the KP solutions discussed in this paper satisfy a constraint:

$$\oint f(x, y, t) dx = 0, \quad (1)$$

and this constraint eliminates the ambiguity of interpreting  $\{\partial_x^{-1}\}$ . Ablowitz and Villarroel (1991) studied this and related constraints.

A detailed derivation of the KP equation can be found in Segur & Finkel (1985), or elsewhere. Briefly, one begins with Stokes' (1847) equations for surface waves on an inviscid, incompressible fluid resting on a horizontal bed under a constant gravitational force,  $g$ . Imposing the three assumptions above yields at leading order the linear, one-dimensional wave equation, whose solution consists of left-going and right-going waves, each travelling with speed  $\sqrt{gh}$ , where  $h$  is the mean depth of the fluid. Each set of waves, of course, has permanent form at this order (*i.e.*, for short times). Over longer times, in a coordinate system moving with (say) the right-going waves, one observes that the right-going waves evolve slowly, due to the three small effects that were neglected at leading order. The last three terms in the KP equation represent the effect on this slow evolution of (i) weak nonlinearity, (ii) weak dispersion, and (iii) weak two-dimensionality.

Let  $\{X, Y, Z\}$  represent spatial coordinates in a fixed laboratory frame with  $Z$  vertical, let  $T$  be time, let  $\eta(X, Y, T)$  measure the elevation of the fluid surface above its mean level, and let  $\epsilon \ll 1$  be a formal small parameter related to the assumptions above. The scaled variables in (KP) can be related to the laboratory coordinates as follows:

$$\begin{aligned} x &= \sqrt{\epsilon}(X - \sqrt{gh}T)/h, & y &= \epsilon Y/h, \\ t &= \epsilon^{3/2}X/6h, & f &= 3\epsilon\eta/2h + O(\epsilon^2). \end{aligned} \tag{2}$$

This change of coordinates can be performed in more than one way; the choice used here is slightly unconventional, and it differs from that in Part 1: ordinarily one sets  $t = \epsilon^{3/2}\sqrt{gh}T/6h$ . Either choice leads to a KP equation, but the solution must be interpreted slightly differently in the two cases. The current choice is more natural for our experimental configuration, but the main motivation for this choice is that it simplifies the surface-fitting algorithm presented in the Appendix.

As noted above, the KP equation is an approximate model of water waves for  $\epsilon \ll 1$ . In order to compare with definite experiments, we set  $\epsilon = 1$  in this paper. To justify this prescription ( $\epsilon=1$ ), we note that the KP equation is invariant under the scaling:

$$x \rightarrow \alpha x, \quad y \rightarrow \alpha^2 y, \quad t \rightarrow \alpha^3 t, \quad f \rightarrow \alpha^{-2} f. \tag{3}$$

Applying this scaling to (2) without the  $O(\epsilon^2)$  terms, with  $\alpha^2 = \epsilon$ , amounts to setting  $\epsilon = 1$  there. As a consequence, some free parameters in the solutions described below must be small for the validity of the approximation.

Krichever (1977) showed that the KP equation admits a huge family of exact solutions in the form

$$f(x, y, t) = 2 \partial_x^2 \ln \Theta, \quad (4)$$

where  $\Theta$  is a Riemann theta function of genus  $N$ . Here  $N$  identifies the number of independent phases in the solution, and  $f$  is a quasi-periodic function of these  $N$  phases. (Recall that "quasi-periodic" means that  $f$  is periodic in each of the  $N$  phases, if the other  $N-1$  phases are held fixed.) In the simplest case,  $N = 1$  and (4) reproduces the familiar cnoidal wave (e.g., Wiegels, 1960). The solutions of interest in this paper have  $N = 2$ , and  $\Theta$  is given by a double Fourier series:

$$\Theta(\phi_1, \phi_2; B) = \sum_{m=-\infty}^{\infty} \sum_{n=-\infty}^{\infty} \exp\left[\frac{1}{2}(m^2 b + 2mn b \lambda + n^2(b\lambda^2 + d)) + i(m\phi_1 + n\phi_2)\right], \quad (5)$$

where the phases  $\phi_1$  and  $\phi_2$  are given by

$$\phi_j = \mu_j x + \nu_j y + \omega_j t + \Phi_j, \quad (j = 1, 2) \quad (6)$$

$\{\Phi_1, \Phi_2\}$  are arbitrary phase constants, and the real-valued parameters  $\{b, \lambda, d\}$ , which define the elements of the Riemann matrix (see Segur and Finkel, 1985), satisfy the following constraints:

$$-\infty < b < 0, \quad 0 < \lambda < 1, \quad -\infty < d \leq b(1-\lambda^2). \quad (7)$$

Actually, the constraint on  $\lambda$  can be tightened to  $[0 < \lambda \leq 1/2]$ . Even so, we use (7) because it allows us to assume that  $\mu_1/\mu_2 \geq 0$ , which simplifies the algorithm in the Appendix. For solutions of genus 2, formal asymptotic validity of the KP model of water waves requires the limit  $\{\mu_j \rightarrow 0, \text{ with } (\nu_j/\mu_j^2) \text{ and } (\omega_j/\mu_j^3) \text{ finite}\}$ . However, we will demonstrate reasonable agreement between theory and experiment even for values of  $\{\mu_1, \mu_2\}$  that are not very small.

The eight free parameters of a real-valued KP solution of genus 2 are  $\{b, \lambda, d, \mu_1, \mu_2, \nu_2; \Phi_1, \Phi_2\}$ . As noted by Dubrovin (1981) and by Segur & Finkel (1985), the parameters can be selected as follows:



- (i) choose  $\{b, \lambda, d\}$  to satisfy (7);
- (ii) choose  $\mu_2$  as an arbitrary positive number, and  $v_2$  as an arbitrary real number;
- (iii) choose  $(\mu_1/\mu_2)$  so that a sixth-order polynomial in  $(\mu_1/\mu_2)$  is positive (the polynomial can be found in Dubrovin (1981) or in Segur & Finkel (1985)); then the square root of the polynomial yields  $v_1$ ;
- (iv) once  $v_1$  is known, then  $\omega_1$  and  $\omega_2$  can be found explicitly in terms of  $\{\mu_1, \mu_2\}$ ;
- (v) choose  $\{\Phi_1, \Phi_2\}$  as arbitrary real numbers, but since they are phase constants, it is sufficient to permit only

$$0 \leq \Phi_j < 2\pi. \quad (j = 1, 2)$$

Every such choice of parameters yields a KP solution of genus 2 that is real-valued, that is periodic in two spatial directions and in time, and that propagates without change in form. The velocity of propagation (in KP coordinates) is given by

$$\frac{dx}{dt} = \frac{v_1\omega_2 - v_2\omega_1}{\mu_1v_2 - \mu_2v_1}, \quad \frac{dy}{dt} = \frac{\mu_1\omega_2 - \mu_2\omega_1}{\mu_2v_1 - \mu_1v_2}. \quad (8)$$

We obtain KP solutions using a FORTRAN code named DELTA. The code is available to interested readers through an anonymous ftp site; see Appendix A for details.

*Symmetric* solutions of genus 2 are obtained by imposing three additional restrictions on these parameters:

$$d = b(1-\lambda^2), \quad (\mu_1/\mu_2) = 1, \quad v_2 = -v_1. \quad (9)$$

It follows from these that  $\omega_2 = \omega_1$ , and that the KP solution is invariant under the transformation  $\{y \rightarrow -y, x \rightarrow x, t \rightarrow t\}$ . Among the KP solutions of genus 2, symmetric waves are special in at least three ways:

- (i) a symmetric wave propagates purely in the  $x$ -direction, because  $dy/dt = 0$  in (8);
  - (ii) a symmetric wave is specified by only  $\{3+2\}$  free parameters, instead of by  $\{6+2\}$ , because of (9); and
  - (iii) a symmetric wave is periodic in the  $x$ - and  $y$ -directions.
- Symmetric solutions were the main focus of the work in Part 1, but not here.

### 3. Experimental program & typical results

The experimental program was similar to that described in Part 1 and identical to that described briefly in Hammack, Scheffner & Segur (1991). Experiments were performed at the Coastal Engineering Research Center (CERC), U.S. Army Engineer Waterways Experiment Station, Vicksburg MS. We used a basin, whose planform is shown schematically in Figure 2, that comprised a uniform-depth section 12.55m long and 26.52m wide, and a section with a gently sloping (1:30) beach that absorbed most of the incident wave energy. In the uniform-depth section, the still water depth was  $20\text{cm} \pm 3\text{mm}$ .

A segmented wavemaker with 58 piston-type paddles, each 45.7 cm wide, spanned the wide wall opposite the beach. The wavemaker was described in detail by Scheffner (1988), and the wavemaker motion was described in Part 1. Briefly, the wavemaker was programmed to generate a superposition of two cnoidal wavetrains with different directions of propagation. In the current experiments, we allowed the wavelengths and/or amplitudes of the two cnoidal waves to differ, so that the resulting two-dimensional wave patterns would be asymmetric. The nomenclature of our experiments, *e.g.* KPaabbcc-AABBCC, is based on programming parameters for the wavemaker. The aa and AA represent the phase lags in degrees between adjacent paddles of the segmented wavemaker for each of the cnoidal wavetrains; the bb and BB are the wavelengths in meters for each of the cnoidal wavetrains; and the cc and CC are crest amplitudes (*i.e.*, maximum elevations above the mean water level) in cms for each of the cnoidal wavetrains. Ordinarily, the wavelengths and amplitudes of the two-dimensional wave patterns that resulted from these inputs differed slightly from these values. A 10s-ramp was applied to the start of each command signal driving the wavemaker to protect the mechanical system from sudden starts. Hence, there is a 10s transient period at each site in the basin before the programmed waves arrived.

Our primary means of wave measurement was a linear array of nine wave gauges that was parallel to, and 8m from, the wavemaker astride the basin centerline. (See Figure 2.) The nine capacitance-type gauges, spaced at 2m intervals, measured the elevation of the water surface. A second array of similar gauges was placed normal to the wavemaker along the basin centerline. It contained eight gauges (one shared with the first array) in the uniform-depth section; seven spaced at 0.5m intervals beginning 6.5m from the wavemaker, and one 2m from the wavemaker. (This array also contained two gauges in the sloping-beach section; data from these gauges are not reported here.) The wave gauges were

calibrated and recording began in a quiescent basin immediately prior to starting the wavemaker. Continuous-time signals for 100s were obtained from all 18 gauges; these signals were low-pass filtered using an 8-pole butterworth filter with a 10Hz cutoff, and then digitized to produce 25Hz discrete-time data. The algorithm to fit KP solutions to wave data, described in detail in Appendix B, is based solely on data from the nine-gauge array; *i.e.*, we make no use of the wavemaker parameters, which are given in the experiment label. As stated earlier, the algorithm was designed in this way so that it could also be used for waves of unknown origin. Data from the second array are used in §4 to test predictions of the fitted solutions.

Wavefields were also measured qualitatively using two Hasselblad cameras, placed 6m apart astride the basin centerline and 7m above the nine-gauge array. The cameras took simultaneous overlapping pictures of the water surface in a darkened room using four 880 W-s strobe lights located on the beach and pointing toward the wavemaker. (The wave gauges were removed from the basin during photography.) The two photographs were then combined to form a mosaic, like those in Figure 1. All photographs were printed so as to maintain the same horizontal scale, which is indicated by the (+) marks painted on the basin floor at 1m intervals. The small, but measurable, differences in spacing between (+) marks apparent in Figure 1 resulted from optical distortions by the waves, which acted like moving lenses. This distortion prevented us from using the overhead photographs to measure spatial wavelengths quantitatively.

Fifteen experiments on asymmetric waves were conducted in the set under discussion. In each experiment, a two-dimensional, spatially periodic wave pattern was created at one end of the tank. The entire wave pattern propagated across the tank with nearly permanent form, it was recorded as it swept by the array of gauges, and then it was mostly absorbed on the sloping beach.

Figure 1 shows clear photographic evidence that two-dimensional, approximately periodic waves exist in shallow water. Photographs of three different wave patterns, corresponding to three experiments, are shown. Each wave pattern propagates from top to bottom in the photos; the front of each wave crest appears bright, while the back appears dark. Some of the bright-dark boundaries in Figure 1a are particularly sharp, indicating that these wave crests are particularly steep, and close to breaking. Close inspection of Figure 1a also shows that on the front faces of these steep waves are capillary waves that appear to be radiating from the crests, as

expected for near-breaking waves. Thus, even though the KP equation is asymptotically valid only for waves of small amplitude, Figure 1a clearly demonstrates that two-dimensional, approximately periodic waves exist even at large amplitudes. The existence and stability of these waves seem to persist well beyond the putative range of validity of the KP model.

The wave pattern in Figure 1a is symmetric, like those discussed in Part 1, and the pattern propagates directly downward in the photograph, *i.e.* in the  $x$ -direction. The wave pattern in Figure 1b is slightly asymmetric, and that in Figure 1c is strongly asymmetric. Asymmetric waves propagate in directions oblique to the  $x$ -direction. A feature common to all of the waves in all of our experiments, including those in Figure 1, is the basic hexagonal shape of the wave pattern. The basic template has a broad, flat trough surrounded by six relatively narrow wave crests. One such hexagon is drawn in Figure 1b. The wave crests opposite each other in this hexagon are parallel, they are equal in length and in wave amplitude, and they can be identified with each other in order to reproduce the periodic pattern, *i.e.*, one can tile the plane with copies of this basic hexagon.

Figure 3 shows typical data obtained from the nine-gauge array for three experiments on asymmetric waves, including two that were photographed in Figures 1b,c. (Note that the waves shown in Figures 1b,c represent about 3 seconds of data in Figures 3a,b.) The 100s records show an initially quiescent water level and the subsequent arrival of the generated wave pattern, whose first 10s exhibit a transient caused by the ramped start of the wavemaker. Data taken during these intervals are excluded in subsequent analysis. (We note also that some wave reflection undoubtedly occurs on the 1:30 sloping beach, leading to small standing-wave components in the wave records. No attempt has been made to remove reflected waves from the data.) At first glance, data at each gauge site may appear to be periodic, especially in Figure 3b; however, careful examination shows that the periodicity is not exact, which is characteristic of quasi-periodic waves.

Figure 4 shows the amplitude-frequency spectrum of each of the wave records shown in Figure 3b. [The spectral amplitude is the modulus of the fast Fourier transform, or FFT, of the data. For convenience, we will refer to these amplitudes as FFTs.] To save space, we omit the spectra for the other experiments shown in Figure 3, but these spectra are qualitatively similar to those shown here. Figure 4 shows clearly the characteristic signatures of two-dimensional, nonlinear, two-phase waves: each of the three FFTs shows two dominant frequencies, plus their harmonics and some

sum- and difference-frequencies. As one moves from the FFT of one wave record to another within each experiment, the amount of energy (*i.e.*, square of the spectral amplitude) at each frequency changes, but the total energy is always distributed among the same two frequencies, plus their harmonics. In this way, the FFTs for each experiment show that all of the gauges measured one-dimensional slices through the same two-dimensional wave pattern. The photographs in Figures 1b,c show clearly the spatial pattern of two-dimensional, two-phase waves, so one expects temporal FFTs like those in Figure 4. However, based solely on the FFTs of wave-gauge data we could infer the following information directly:

- (i) the wave pattern has two phases (or possibly more than two in degenerate cases, but with only two independent frequencies among the phases);
- (ii) the wave pattern is nonlinear, because energies at harmonics as well as at the sum- and difference-frequencies are significant.

The fact that the same two frequencies are measured at every gauge, with different energy levels, suggests that the wave pattern might be two-dimensional, but it does not establish the two-dimensionality conclusively. If the wave pattern is genuinely two-dimensional with exactly two phases, then necessarily it is stationary in some uniformly translating coordinate system; *i.e.*, it must be a wave of permanent form.

Figure 4 also lists the numerical values of the two fundamental frequencies measured in the experiment. The two-dimensional wave patterns shown in Figure 1 are periodic, but the one-dimensional wave records in Figure 3 are not periodic unless these two frequencies are rationally related. Since the frequencies listed in Figure 4 were obtained numerically, they are necessarily rationally related. However, for experiment KP220203-110403, the period implied by the two frequencies exceeds 600 seconds, so this exact periodicity is irrelevant for the 100 seconds of recorded data, which are effectively quasi-periodic.

We note finally that quasi-periodic functions also arise in the theory of dynamical systems (*e.g.*, Guckenheimer & Holmes, 1983), where quasi-periodic behaviour often suggests incipient instability and chaos (Piexoto, 1962). No such instability is suggested from the quasi-periodicity seen in Figure 3. These data are quasi-periodic only because the data are taken from a doubly periodic function, along a line at an irrational angle from a direction of periodicity. The water waves being measured seem to be remarkably stable.

#### 4. Comparison of theory and experiment

In Appendix B, we present an algorithm to find the KP solution of genus 2 that best fits experimental data like those shown in Figure 3. Here is a brief summary of the algorithm. Recall from §2 that a KP solution of genus 2 is specified by eight real-valued parameters. Four of these ( $\mu_1, \mu_2, \nu_1, \nu_2$ ) are wavenumbers that determine the overall spatial structure of the wave pattern. Two of them are easy to find: ( $\mu_1, \mu_2$ ) are proportional to the two frequencies identified in Figure 4. Once the spatial structure is known, then one varies ( $b, d, \lambda$ ) in order to match (as closely as possible) the observed maximum and minimum amplitudes, and the known spatial structure. Then one determines the two phase constants ( $\Phi_1, \Phi_2$ ) by minimizing the rms (or  $L_2$ ) error for the entire wave pattern. Finally, with good approximations to the eight KP parameters determined in this way, one selects final values for all eight parameters by minimizing the rms-error for the wave pattern again. (Thus, the KP solution found in this way is "best" in the sense of least rms-error.)

This algorithm was used to find the best KP solution for each of fifteen experiments with asymmetric wave patterns. We begin our discussion of results with the question: How accurately does the best KP solution represent the data used to select that solution? For conciseness, we concentrate on the three experiments shown in Figure 3.

##### a) Surface-fitting

For the experiment shown in Figures 1b and 3a, Figure 5 shows a comparison between the measured data with the best KP solution at the same locations, for 20 seconds of data, and for all of the gauges in the nine-gauge array. (Most of our comparisons begin 30 seconds into the recorded data in order to exclude the quiescent and transient intervals, and last for 20 seconds. The agreement between theory and experiment is largely independent of when we start the comparison and how long we compare.) The agreement between KP theory and experimental data in Figure 5 is perfect nowhere, but it is fairly good everywhere. The KP solution captures the overall structure of the wave pattern; it describes the phase information, such as zero-crossings, particularly well. Note especially the amplitudes of the waves in Figure 5. From Figure 3, the maximum crest-to-trough height ( $H$ ) for this wave pattern is 11.23 cm., which corresponds to a wave height-to-depth ratio ( $H/h$ ) of 0.56. Peregrine (1983) discusses criteria for wave-breaking in shallow water (e.g.,  $H/h = 0.77$  at breaking). The wave pattern shown here is not breaking, but it is not far from the range of breaking waves;

certainly the wave amplitudes are not especially small. This result is similar to that found in Part 1 for symmetric waves: KP theory agrees well with experimental measurements well outside its putative range of validity.

Figure 6 shows another comparison of theory and experiment, for the wave pattern shown in Figures 1c and 3b. This pattern is strongly asymmetric, but again the best KP solution gives good agreement everywhere. Figure 3b shows that these waves are almost periodic, with an almost-period of about 20 seconds. Figure 6 shows that the KP solution has essentially the same behaviour. [In fact, the comparison-time of 20 seconds was chosen to contain the almost-period of these waves.] Because this experiment was also photographed (in Figure 1c), we can compare the KP solution with the photograph as well. In Figure 7, contour lines of the best KP solution are superimposed on the photograph. This comparison contains different information than that in Figure 6:  $X$  is held fixed while  $T$  and  $Y$  vary in Figure 6, whereas  $T$  is held fixed while  $X$  and  $Y$  vary in Figure 7. Moreover, the photograph was not used to find the KP solution, so Figure 7 is *not* surface-fitting. Even so, Figure 7 leads to a conclusion similar to that obtained from Figures 5 and 6: the best KP solution describes the observed wave pattern with reasonable accuracy everywhere.

The last detailed comparison, for KP300102-30•803, has been included because the wave records from gauges 3 and 7 showed a slow increase in amplitude over the course of this experiment, as seen in Figure 3c. While it is clear that the data in Figure 3b are almost periodic, this is much less clear in Figure 3c, so this experiment provides a strong test of the theory. Figure 8a shows a comparison of the measured wave records with the best KP solution, for 20 seconds of data starting at 30 seconds. These waves have smaller amplitudes than those in other experiments in this series, so the waves are more nearly sinusoidal, and the agreement between theory and experiment is slightly better than average. Note that the wave amplitudes for gauges 3 and 7 increase, even in this 20-second interval. Note also that for gauge 3, the KP solution captures this behaviour.

Figure 8b shows a second comparison for the same experiment, KP300102-30•803, starting at 70 seconds. It is important to note that the KP solution used here is *the same* KP solution as that in Figure 8a, except that the two phase variables,  $\Phi_1$  and  $\Phi_2$ , were re-optimized for the new data, which were measured during a different time interval. In other words, Figure 8b is not a surface-fit; it is a prediction of the theory, based on the surface-fit shown in Figure 8a.

Figure 3c shows that the data measured at 20 seconds differ considerably from those measured at 70 seconds, but the same KP solution describes both data sets with reasonable accuracy. This good agreement implies that the data in Figure 3c are almost periodic, but the almost-period is so much longer than the 80 seconds of data that this feature is not apparent in the measured data. We mention that we also applied the optimization algorithm to the data in Figure 8b, to find the best KP solution for those data. The KP solution found was nearly identical with that obtained from the data in Figure 8a, except for changes in  $\Phi_1$  and  $\Phi_2$ .

*b) Analysis of errors*

Table 1 summarizes the comparisons between KP theory and experiments for fifteen experiments involving asymmetric waves. The parameters of the best KP solutions are listed, as well as the maximum and minimum measured wave amplitudes, and two measures of error, which we now define.

For a given experiment, let  $u(x, y, t)$  denote the measured wave amplitude at location  $(x, y, t)$ , normalized as in (2), and let  $f(x, y, t)$  denote the value of the best KP solution at the same location. One measure of their discrepancy is  $\sigma$ , where

$$\sigma^2 = \frac{\sum_{i=1}^9 \int_0^L [f(x,y,t) - u(x,y,t)]^2 dx}{\sum_{i=1}^9 \int_0^L [u(x,y,t)]^2 dx}, \quad (10)$$

the sum is taken over the wave records from the nine-gauge array, and  $L$  is the length of the measured wave records. (We generally used 20 seconds of data, but varying the length of the data string did not significantly affect  $\sigma$ .) A second measure of error is  $f_{max}/u_{max}$ , the ratio of maximum wave amplitudes according to theory and experiment. (Step 4 of the optimization algorithm effectively minimizes  $(1-f_{max}/u_{max})^2$ , but then the last step of the algorithm usually forces it away from its minimal value, leaving  $f_{max}/u_{max}$  as a nontrivial measure of error.)

According to Table 1, the KP model along with the optimization algorithm consistently underpredicted the maximum wave amplitude. This error was more serious in some experiments than in others, but the model predicted a maximum amplitude that was too small in every experiment. This consistent underprediction was



apparently caused by using the norm in (10). In Part 1 we used a different norm, and matched the maximum amplitudes well. Beyond this simple observation, we found no striking trends in the data. For all fifteen experiments,  $\sigma$  stayed within a fairly narrow range:

$0.235 \leq \sigma \leq 0.402$ , with a mean value of  $E(\sigma) = 0.302$ . (For comparison, note that the trivial theory, in which  $f(x, y, t) \equiv 0$ , gives  $\sigma=1$  in (10).) We do not suggest from this relatively narrow range of values that the theory never breaks down, but only that our experiments did not demonstrate the breakdown.

As mentioned in §2, the KP model of water waves is based on three assumptions: (i) moderate wave amplitudes; (ii) shallow water; and (iii) nearly one-dimensional wave propagation. An important question is how  $\sigma$  depends on each of these three effects. Consider first the wave amplitudes, which we characterize by the maximum crest-to-trough height, divided by the undisturbed water depth, which was 20 cm in these experiments. (This choice is based on the columns entitled  $\eta_{max}$  and  $\eta_{min}$  in Table 1, and is somewhat arbitrary. We also tried using  $\eta_{max}$ , with similar results. Using  $\sigma$ , instead of  $\sigma^2$  or some other measure of error, is also arbitrary.) For the  $j^{\text{th}}$  experiment, let

$$A_j := [\eta_{max, j} - \eta_{min, j}]/h. \quad (11)$$

From Table 1,  $0.341 \leq A_j \leq 0.561$ , with a mean value,  $E(A) = 0.492$ . The correlation coefficient between  $A$  and  $\sigma$  in our fifteen experiments is

$$\rho(A, \sigma) := \frac{\sum_{j=1}^{15} [A_j - E(A)] * [\sigma_j - E(\sigma)]}{\left\{ \sum_{j=1}^{15} [A_j - E(A)]^2 * \sum_{j=1}^{15} [\sigma_j - E(\sigma)]^2 \right\}^{1/2}} = 0.39. \quad (12)$$

This positive correlation shows that KP theory becomes less accurate as wave amplitudes increase, as expected.

It remains to test the assumptions of shallow water, and of nearly one-dimensional waves. Unfortunately, our data set (based on fifteen experiments) was too small to carry out these tests conclusively.

### c) Predictions

Knowing that the KP model provides reasonably accurate descriptions of the measured wavefields, we now turn to other

comparisons between theory and experiments. For each experiment, the best KP solution is now fixed, with no remaining free parameters; hence, the comparisons that follow involve predictions of the theory, rather than just surface-fitting.

A fundamental assertion in this paper is that the waves under study propagate with nearly permanent form. Yet data from the nine-gauge array cannot test this assertion, because all nine gauges are the same distance from the wavemaker. Limited insight into possible wave evolution is provided by the second gauge array, which was placed perpendicular to the first array (see Figure 2). We show next that to within our experimental error, the waves did not evolve significantly over the 7.5 m span of the second array. Again, for simplicity, we concentrate on the three experiments shown in Figure 3.

For each experiment, the second gauge-array provides eight wave records like those in Figure 3. Figure 9 shows the temporal FFT of each of the seven new wave records for experiment KP220203-110403, featured in Figures 1c, 3b, and 4. (Note from Figure 2 that gauge 5 was included in both arrays. In presenting the data from the second array, we omit gauge 5 because its data were already presented. We also omit the data from the other experiments, which data were qualitatively similar to those shown in Figure 9.) Note that every gauge in the second array recorded the same two dominant frequencies, and therefore the same values for  $\mu_1$  and  $\mu_2$ ; in other words,  $\mu_1$  and  $\mu_2$  showed no measurable evolution as the waves propagated away from the wavemaker.

Figure 10 shows the actual wave records from the seven new gauges, for experiment KP220203-110403. The KP solution that was already selected, based on data from the nine-gauge array, predicts the data that each of these seven gauges should measure; these predictions are also shown in Figure 10. We emphasize that no free parameters were available in the comparisons in Figure 10; these are predictions rather than surface-fits. The overall error ( $\sigma_X$ ) for the seven-gauge array is comparable to that for the nine-gauge array ( $\sigma$ ), even though data from the latter array were used to select the KP solution. For all fifteen experiments on asymmetric waves, Table 2 lists an overall error ( $\sigma$ ) for the nine-gauge array used to select the KP solution, and another ( $\sigma_X$ ) for the seven-gauge array, whose measurements were predicted by that KP solution. Within each experiment, these errors are comparable; usually  $\sigma_X$  is slightly larger than  $\sigma$ , but for experiment KP400203\_300303, the error for the seven-gauge array ( $\sigma_X$ ) is actually smaller than that for the nine-

gauge array ( $\sigma$ ). This comparison supports the claim that the measured waves did not evolve significantly over the length of our test section.

Approximate wavelengths in the X-direction for a KP solution can be obtained from  $\{\mu_1, \mu_2\}$ , using  $L_i \approx 2\pi h/\mu_i$ . For experiment KP220203\_110403, this gives X-wavelengths of about 2 m and 4 m, consistent with the cnoidal wavelengths input to the wavemaker. Note that gauge 10 is only 2 m. from the wavemaker, so Figure 10 shows that the wave being measured achieved its apparently permanent form within one wavelength of the wavemaker, and then retained that form at least for the length of the test section of the tank (7.5 m). In all fifteen experiments, we always found that the wave patterns achieved their apparently permanent form within 2 m of the wavemaker, and then retained that form over the length of our test section. We found no clear evidence of wave evolution.

Next, we consider the (constant) velocity of propagation of the waves. This velocity cannot be inferred from the photographs in Figure 1. The KP model predicts it, in (8), and the velocity vector shown in Figure 7 was found in this way. However, the velocity also can be obtained directly from the wave records, without using (8), as follows. For a particular experiment, find the KP solution that best fits the data measured during a 20 second interval starting at time (T). If the wave has permanent form, then at a slightly later time (T +  $\Delta T$ ), this wave pattern will have translated in space, and what had been observed at location (X -  $\Delta X$ , Y -  $\Delta Y$ ) in the fixed (laboratory) frame now will be observed at (X, Y), for some  $\{\Delta X, \Delta Y\}$ . In order to measure  $\{\Delta X, \Delta Y\}$ , use (2) to replace (6) by

$$\phi_j = \mu_j(x - \Delta X/h) + v_j(y - \Delta Y/h) + \omega_j(t - \Delta X/6h) + \Phi_j, (j = 1,2) \quad (13)$$

and then minimize  $\sigma^2$  at the new time (i.e., over 20 seconds starting at T +  $\Delta T$ ) by varying  $\{\Delta X, \Delta Y\}$ , holding fixed all the other parameters of the solution. In this way, one obtains empirically  $\{\Delta X, \Delta Y\}$  for a given  $\Delta T$ . For a wave of permanent form,  $(\Delta X/\Delta T)$  and  $(\Delta Y/\Delta T)$  do not depend on  $\Delta T$ , and it follows from (2) that

$$\frac{dx}{dt} = 6(1 - \sqrt{gh} \frac{\Delta T}{\Delta X}), \quad \frac{dy}{dt} = 6 \frac{\Delta Y}{\Delta X}. \quad (14)$$

Because the KP solution is spatially periodic,  $\{\Delta X, \Delta Y\}$  are ambiguous in the sense that one can add to them an integer number of spatial

periods of the wave pattern. One eliminates this discrete ambiguity by requiring that  $\Delta X \rightarrow 0, \Delta Y \rightarrow 0$  as  $\Delta T \rightarrow 0$ ; then  $(\Delta X, \Delta Y)$  are unambiguous for  $\Delta T$  small enough. On the other hand, small measurement errors become relatively important if  $\Delta T$  is too small. Balancing these competing effects, we chose  $\Delta T = 1.2$  seconds for these experiments.

Table 2 lists the two components of the velocity of propagation of the wave pattern, according to KP theory (8) and according to direct measurement (14), for all fifteen experiments. The agreement is remarkably good; in many cases, the two velocities agree to within a few percent. The agreement becomes even more impressive when one recalls that these velocities are themselves the small deviations from the basic wave speed,  $\sqrt{gh}$ , which is inherent in the (moving) KP coordinate system.

### 5. *Oceanic observations of hexagonal waves in shallow water*

The central point of this paper is the following. In shallow water of uniform depth, there exist two-dimensional periodic waves with finite amplitudes and nearly permanent form. The spatial pattern of these waves is hexagonal, as shown in Figure 1. The waves are easy to generate in the laboratory, and they are apparently stable.

KP solutions of genus 2 describe these waves with reasonable accuracy over a range of parameters that is larger than the putative range of validity of the KP model. The robustness of the KP model is a pleasant surprise, but we suspect that the existence of these waves is independent of the validity of the KP model. Rather, we conjecture that the hexagonal wave pattern observed in Figure 1 is the basic qualitative pattern for periodic waves of permanent form in shallow water. More precisely, we conjecture that if one seeks genuinely two-dimensional wave patterns of finite amplitude that are periodic and that propagate with permanent form in shallow water of uniform depth, then one will almost certainly find hexagonal wave patterns with flat troughs and narrow crests, like those in Figure 1. If this conjecture is correct, then one would expect to find waves like these in oceanic settings. In this section, we present some oceanic observations suggesting that wave patterns like these actually occur. *Remark:* Some apparent counter-examples to this conjecture are actually limiting cases of it. We mention specifically: (i) cnoidal waves, in which the wave period in one direction becomes infinitely long; (ii) waves of infinitesimal amplitude, for which the hexagon degenerates to a parallelogram, and the waves become sinusoidal; and (iii) the oblique interaction of two solitons, which is not periodic, but is another limiting case of hexagonal waves.

The first example, shown in Figure 11, is an aerial photograph of the coastal zone taken near Jones Inlet on Long Island near New York City. At the top of the photograph one can identify a road, some buildings, the beach, and the surf zone in which waves are breaking. Beyond the surf zone, in the bottom half of the photograph, one sees clearly that the surface wave patterns are two-dimensional and approximately periodic, like the waves in Figure 1, and that many of the wave patterns are hexagonal.

The second example, shown in Figure 12, is a now well-known photograph taken by Terry Toedtemeier of two waves interacting in shallow water off the Oregon coast. This photograph is often shown to illustrate the interaction of two solitons, with the required phase shift (*i.e.* a spatial shift of each wave crest as a result of the nonlinear interaction of the two waves). However, each of the most prominent

wave crests in Figure 12 is actually part of a train of periodic waves. The next crest in each train is discernible in the figure, but the strongest evidence of the periodicity of the wavefield is that Mr. Toedtemeier told us that the waves were periodic. He also noted that none of the other wave interactions, before or after the one shown in Figure 12, was nearly as dramatic as the one shown. Thus, these waves were only approximately periodic, but they were certainly two-dimensional, and they exhibited flat troughs and sharp crests. In our model, the two long crests and the one short crest shown in the figure should be viewed as the sides of two adjacent hexagons.

The last example, shown in Figure 13, is an aerial photograph of waves off the outer banks of North Carolina taken by Carl Miller during a major storm (the "Hallowe'en storm of 1991"). The waves in this photograph were enormous—wave gauges located in 10m deep water measured waves with heights exceeding 5m and periods of 20s. If we take the wave speed to be  $\sqrt{gh}$  as a rough approximation, then a wave period of 20s corresponds to a wavelength of about 200m. (Assigning a width of 5 m. to the road visible along the coast and then scaling also suggests wavelengths on the order of 100-200 m.) The photograph itself suggests that virtually every wave crest was breaking, and that the beach on the right of the photo was completely flooded. These waves were apparently far outside the range of validity of the KP model. Moreover, these waves undoubtedly did not have permanent form, so that KP solutions of genus 2 would be too simple to describe them. Nevertheless, the waves in Figure 13 exhibit some of the same features that we have now seen repeatedly: two-dimensional wave patterns with flat troughs and sharp crests, and with many of the crests forming hexagonal wave patterns.

The photographs in Figures 11, 12 and 13 suggest that approximately periodic, hexagonal wave patterns occur in the ocean. Without a systematic study of oceanic observations of waves in shallow water, we do not know whether these waves are common or uncommon. We suspect that they are more common than is usually believed.

### *Acknowledgements*

We are grateful to Boris Dubrovin and James Curry for useful comments and encouragement, and we thank Terry Toedtemeier and Carl Miller for permission to use the photographs in Figures 12 and 13, respectively. Laura Mather and David Deininger provided useful programming assistance. We gratefully acknowledge the support and cooperation of the Coastal Engineering Research Center, US Army Engineer Waterways Experiment Station in Vicksburg, MS, which made these experiments possible, and we thank the Office, Chief of Engineers, US Army Corps of Engineers for authorizing publication of this research. This work was supported in part by ONR grant N00014-92-J-1274. Finally, we were saddened to learn that V.I. Petviashvili passed away in July, 1993.

### *Appendix A: To obtain the program DELTA*

The KP solutions used in this paper were computed using a FORTRAN program named DELTA. The following instructions show how to use the UNIX ftp utility to transfer the file "delta.f" from the anonymous site "ftp.colorado.edu:/cuboulder/appm". The indented lines are keyboard commands, with <cr> = carriage return.

To log onto the ftp site, type

ftp ftp.colorado.edu <cr>

You should get a prompt for a username. Type

anonymous <cr>

You will then be prompted for a password. Enter your complete email address. At this point, you should be logged onto the ftp site.

You need to go to the subdirectory /cuboulder/appm. Type

cd cuboulder/appm <cr>

To transfer the file, type

get delta.f <cr>

To quit the ftp utility, type

quit <cr>

*Appendix B: An algorithm to find the best KP solution for a set of wave-gauge data*

A KP solution of genus 2 is defined by (6+2) parameters  $\{b, \lambda, d, \mu_1, \mu_2, v_2; \Phi_1, \Phi_2\}$ , from which the other parameters of the solution  $\{v_1, \omega_1, \omega_2\}$  can be deduced. The objective of this Appendix is to provide an effective algorithm to identify a "best" set of KP parameters for a given set of wave records, like those in Figure 3. The algorithm has six steps, and it makes explicit use of the fact that the time-variation of a quasi-periodic function, like that of (5) and (6), corresponds to straight-line motion on a two-dimensional torus.

*Step 1: Find  $\mu_1$  and  $\mu_2$ .*

If the measured wave amplitudes can be represented by a KP solution of genus 2, then it follows from §2 that we seek a function of the form

$$f(x, y, t) = F(\mu_1 x + v_1 y + \omega_1 t, \mu_2 x + v_2 y + \omega_2 t),$$

where  $F$  is periodic in each argument. Without loss of generality, we can require that each period be  $2\pi$ ; otherwise, the precise form of  $F$  does not affect step 1. In terms of laboratory coordinates, after using (1) with  $\epsilon = 1$ ,

$$f = F(\mu_1(X - \sqrt{gh}T)/h + v_1 Y/h + \omega_1 X/6h, \mu_2(X - \sqrt{gh}T)/h + v_2 Y/h + \omega_2 X/6h). \quad (15)$$

Each wave gauge records data as  $T$  varies, with  $X$  and  $Y$  fixed. If it records a function in the form (15), then the FFT of the wave record shows energy at two frequencies,  $\sqrt{gh}/h \mu_1$  and  $\sqrt{gh}/h \mu_2$ , plus harmonics and sum- and difference-frequencies. In other words, one can read  $|\mu_1|$  and  $|\mu_2|$  directly from FFTs of the wave records, like those in Figure 4. Because of (7), one can always require  $\mu_1/\mu_2 \geq 0$ . Because  $\Theta$  is even [ $\Theta(\phi_1, \phi_2) = \Theta(-\phi_1, -\phi_2)$ ], one can always take  $\mu_1 \geq 0, \mu_2 \geq 0$ . These two symmetries allow us to determine  $\mu_1$  and  $\mu_2$  from FFTs.

*Remark:* The advantage of the choice of variables in (2) is that it permits direct measurement of  $\mu_1$  and  $\mu_2$ . With the usual choice,  $t = \epsilon^{3/2} \sqrt{gh} T/6h$ , the FFTs yield  $(\mu_1 - \omega_1/6)$  and  $(\mu_2 - \omega_2/6)$  and one must solve to find  $\mu_1$  and  $\mu_2$ . We have tried both approaches; the final results differ only slightly, and the logic of the current approach is simpler.

*Step 2: Find  $|v_1|$  and  $|v_2|$ .*



In these experiments we used only nine gauges at different locations in Y, so a Fourier transform in Y of the data at fixed (X, T) would yield only crude estimates of  $|v_1|$  and  $|v_2|$ . We obtain more precise estimates of  $|v_1|$  and  $|v_2|$  when the wave height is a quasi-periodic function of two variables, as follows.

Let  $F(\phi_1, \phi_2)$  be continuous and quasi-periodic. Along the line  $[\phi_1 = \alpha\phi_2 + \beta]$  in the  $(\phi_1, \phi_2)$ -plane,  $F(\phi_1, \phi_2)$  is periodic if and only if  $\alpha$  is rational. If  $\alpha$  is irrational, then along this line  $F(\phi_1, \phi_2)$  never repeats exactly, but it comes arbitrarily close to every value taken by  $F(\phi_1, \phi_2)$  in the periodic square. Now compare this situation to that in Figures 1 and 3. Figure 1 shows a periodic function of two variables, and each wave record shown in Figure 3 is taken along a straight line defined by the direction of travel of the wave pattern as it sweeps past the gauges. It follows that if the data in each record are not periodic, then a sufficiently long string of data from a single gauge would eventually record the entire two-dimensional wave pattern, to any desired accuracy. Moreover, the nine gauges sweep out nine parallel line-segments in the  $(\phi_1, \phi_2)$ -plane. If the data are not periodic, then to any desired accuracy, one can think of these nine line-segments as segments on the same (infinite) line, with different starting points.

For example, in Figure 3b, the data recorded on gauge 9 nearly coincides with that recorded on gauge 3, but with a time-shift of 36.8 seconds. This can be seen directly, by laying a record from gauge 9 over that from gauge 3 (but shifted by 36.8 seconds) and observing that the data nearly coincide. More quantitatively, the two data sets (with the first 20 seconds of each data-set deleted, to remove quiescent and transient intervals) have a correlation coefficient of  $\rho = 0.966$ , where

$$\rho = \frac{\int_0^L \eta_i(t) \eta_j(t) dt}{[\int_0^L \eta_i(t)^2 dt \int_0^L \eta_j(t)^2 dt]^{1/2}}, \quad (16)$$

and where  $\eta_i(t)$  and  $\eta_j(t)$  each have zero mean. Moreover, using the same time-shift (36.8 seconds), the data from gauge 8 correlate with those from gauge 2 (with  $\rho = 0.966$ ), and gauge 7 reproduces the data from gauge 1 (with  $\rho = 0.975$ ). In other words, with an error

corresponding to a correlation coefficient of about 0.97, a shift in  $Y$  of 12 m (the distance between correlated gauges) is equivalent to a shift in  $T$  of 36.8 seconds. We have just demonstrated this with three pairs of gauges:  $9 \rightarrow 3$ ,  $8 \rightarrow 2$ ,  $7 \rightarrow 1$ . By this reasoning, had there been a "virtual" gauge 10 in the shore-parallel array, it would have measured a signal (nearly) equal to that measured by gauge 4, but shifted by 36.8 seconds. Moreover, virtual gauge 11 would have measured a signal corresponding to that of gauge 5, and so on. Eventually, when we return to gauge 9 (at virtual gauge 15), we could start over by comparing its signal to that of gauge 3 again. This entire process can be repeated until we have shifted (in time) to the end of the data-records. In addition, the data from a single gauge can be matched to itself in a second, independent way, and between these two shifts we can extend the data indefinitely. Referring again to Figure 3b, note that the data from any one gauge are almost periodic, with an almost-period of 41.84 seconds. In particular, in Figure 3b the correlation coefficient between the data, and the data shifted by 41.84 seconds, averages about 0.99 for gauges 4-9. By making use of these two kinds of shifts, one can create as many virtual gauges as desired. Each shift introduces a small error, whose size is related to  $(1 - \rho)$ . In principle, one should stop adding virtual gauges when the accumulation of these errors exceeds the increased precision obtained from adding more gauges. Preliminary tests suggested that the break-even point for these data occurs at about 200 gauges; in practice, we always stopped at 200 gauges, including the 9 original gauges.

Now take a FFT in  $Y$  at fixed  $(X, T)$ , based on 200 data; the results are shown in Figure 14, for experiment KP220203-110403. As in Figure 4, the energy is concentrated in two dominant "frequencies", plus harmonics and sum- and difference-frequencies. Assuming that the data represent a function of the form (10), then these dominant frequencies are located at  $|v_1/h|$  and  $|v_2/h|$ . In this way, the procedure provides direct measurement of  $|v_1|$  and  $|v_2|$ . This procedure does not specify which of the two values should be associated with  $\mu_1$ , and which with  $\mu_2$ . Until this has been resolved (in step 3), let us call the two values  $|v_a|$  and  $|v_b|$ , with  $|v_a| \leq |v_b|$ .

#### *Step 2a: Symmetric waves*

The essential requirements for step 2 are that the data be quasi-periodic, but not strictly periodic. If the data are periodic with a sufficiently short period, then the wave records from two different gauges might never look alike, for any time-shift. In particular, symmetric waves produce periodic wave records, and the records

from different gauges look alike only if two of the gauges happen to be an integer number of Y-wavelengths apart. For symmetric (or nearly symmetric) waves, we estimate the Y-wavelength from a FFT based on only nine gauges. This estimate is necessarily crude. Consequently, for some experiments with symmetric waves, we found it necessary to admit two or three "candidate values" for  $|v_a|$  ( $= |v_b|$  for a symmetric wave), chosen from the range allowed by the nine-gauge FFT.

The remaining steps of the algorithm assume that the wave pattern is asymmetric, that the data are not strictly periodic, and that step 2 has successfully provided  $|v_a|$  and  $|v_b|$ . [For symmetric waves,  $\mu_2 = \mu_1$ ,  $v_2 = -v_1$ , so step 3 is unnecessary. Then step 4 simplifies, because  $d = b(1 - \lambda^2)$ .]

*Step 3: Identify  $v_1$  and  $v_2$*

The next step is to find the signs of  $v_a$  and  $v_b$ , and to determine which value goes with  $\mu_1$ , and which with  $\mu_2$ . The basic idea for this step is the following. The nine-gauge array lies in the y-direction, and the data from it determine  $|v_a|$  and  $|v_b|$ . If the array were rotated slightly in the x-y plane, then the gauges would record slightly larger y-wavelengths for waves coming from one side, and slightly smaller y-wavelengths for waves coming from the other. By comparing the values of  $|v_a|$  and  $|v_b|$  obtained from the original and the rotated gauge-arrays, one could determine whether the associated waves came from the left or the right; *i.e.*, one could determine the signs of  $v_a$  and  $v_b$ .

We do not actually move the gauges to obtain the second data set, but we achieve approximately the same effect by processing data from successive gauges at successively later times. Specifically, instead of using the data from all nine gauges at the same time  $T_0$ , we use the data from the  $j^{\text{th}}$  gauge that was recorded at time:

$$T_j = T_0 + (j - 1)\Delta T,$$

where  $\Delta T$  is the time between successive measurements. ( $\Delta T = 0.04$  seconds for the 25 Hz sampling rate used in these experiments.) These data correspond approximately to data taken from a linear gauge-array whose orientation in the x-y plane is rotated from the y-axis through an angle

$$\beta = \tan^{-1}[\sqrt{gh} \Delta T / \Delta Y], \quad (17)$$

where  $\Delta Y$  is the spacing between gauges. In these experiments,  $\Delta Y = 2$  m, so  $\beta = 0.028$  rad ( $\beta = 1.6^\circ$ ). With the data rearranged in this way, we repeat step 2 to obtain  $|v_i^+|$  and  $|v_j^+|$ . The same procedure based on  $(-\Delta T)$  yields  $|v_i^-|$  and  $|v_j^-|$ . From all of these, one can identify  $\{|v_a^-, |v_a^+|\}$  and  $\{|v_b^-, |v_b^+|\}$ , because

$$|v_a| - |v_a^+| \approx |v_a^-| - |v_a|, \quad |v_b| - |v_b^+| \approx |v_b^-| - |v_b|. \quad (18)$$

The direction of effective rotation ( $\beta$ ) is known, so knowing whether  $\{|v_a^-| < |v_a| < |v_a^+|\}$  or  $\{|v_a^-| > |v_a| > |v_a^+|\}$  determines the sign of  $v_a$ ; one also finds the sign of  $v_b$  in this way. [Note: If  $|v_a|$  is small enough, then  $\{v_a^+, v_a, v_a^-\}$  are not all of the same sign, and no combination of measured values satisfies (18). In this case, one finds that either

$$|v_a| + |v_a^+| \approx |v_a^-| - |v_a|, \quad \text{or} \quad |v_a| - |v_a^+| \approx |v_a^-| + |v_a|.$$

If both  $|v_a|$  and  $|v_b|$  are small, then (18b) must be modified as well.]

The  $v$ -values obtained in this way also provide estimates for  $\{\mu_a, \mu_b\}$ , based on

$$\mu_a \approx (v_a^+ - v_a \cos \beta) / \sin \beta.$$

By comparing these estimates with the values for  $\mu_1$  and  $\mu_2$  obtained in step 1, one determines  $\{\mu_1, v_1\}$  and  $\{\mu_2, v_2\}$ .

*Step 4: Estimate  $\{b, \lambda, d\}$*

Once  $\{\mu_1, \mu_2, v_1, v_2\}$  are known, then the spatial structure of the wave pattern is fixed, and one can draw a period parallelogram in the  $(x, y)$ -plane. Next, one would like to choose, among all KP solutions of genus 2 with the same period parallelogram, the one that minimizes the rms error,

$$\tilde{\sigma}^2 = \frac{\iint [f(x, y, t) - u(x, y, t)]^2 dx dy}{\iint [u(x, y, t)]^2 dx dy}, \quad (19)$$

where  $u(x, y, t)$  represents the measured data (normalized as in (2)),  $f(x, y, t)$  represents a KP solution, and the integrals are taken over a period parallelogram. In step 6, we do essentially this.

Unfortunately,  $\tilde{\sigma}^2$  apparently has many local minima in parameter space, so that it is necessary to start the minimization routine close to the global minimum. The purpose of steps 4 and 5 is to obtain good starting values for the minimization in step 6.

Let  $u_{\max}$  denote the measured maximum value of the (normalized) wave amplitude over the entire data set for an experiment, and  $u_{\min}$  the measured minimum value. If the waves were exactly periodic, then the wave amplitude would attain its maximum and minimum values once within each period parallelogram. As discussed in §2, specifying  $\{b, \lambda, d, \mu_1, \mu_2, v_2\}$  specifies a KP solution of genus 2, up to a translation. In particular, these parameters determine the maximum ( $f_{\max}$ ) and minimum ( $f_{\min}$ ) values of the solution, and they determine  $v_1$ . Denote by  $v_{1,KP}$  the value of  $v_1$  obtained from a particular KP solution, and by  $v_{1,m}$  the value of  $v_1$  measured in steps 2 and 3. Step 4 is to minimize

$$E = (1 - \frac{v_{1,KP}}{v_{1,m}})^2 + (1 - \frac{f_{\max}}{u_{\max}})^2 + (1 - \frac{f_{\min}}{u_{\min}})^2, \quad (20)$$

by varying  $\{b, \lambda, d\}$ , subject to (7), while holding  $\{\mu_1, \mu_2, v_2\}$  fixed at the values obtained in steps 1-3. We do this numerically, using ODRPACK as described by Boggs, Byrd, Rogers, and Schnabel (1992).

*Step 5: Estimate  $\Phi_1$  and  $\Phi_2$*

The KP solution is now completely specified except for a spatial translation fixed by the phase constants  $\Phi_1$  and  $\Phi_2$ . These constants could be obtained directly from an overhead photograph of the wavefield, such as those in Figure 1, by making a contour plot of the KP solution with the same horizontal scales as the photograph, and then sliding one over the other until the phases match optimally. In the absence of such a photograph, we minimize a quantity like that in (19), by varying  $\{\Phi_1, \Phi_2\}$  while holding fixed  $\{b, \lambda, d, \mu_1, \mu_2, v_2\}$ . However, we cannot integrate over the entire period parallelogram, as in (19), but only over the nine wave records. Using ODRPACK again, we minimize

$$\sigma^2 = \frac{\sum_1^9 \int_0^L [f(x,y,t) - u(x,y,t)]^2 dx}{\sum_1^9 \int_0^L [u(x,y,t)]^2 dx}, \quad (10)$$

where  $L$  is a length of the wave record, and only  $\{\Phi_1, \Phi_2\}$  are varied. Typically, we used  $L = 20$  seconds.

*Step 6: Find final values of all eight parameters*

The final step is to minimize  $\sigma^2$  again, allowing all eight parameters  $\{b, \lambda, d, \mu_1, \mu_2, v_2; \Phi_1, \Phi_2\}$  to vary simultaneously. In this paper, therefore, the "best" KP solution for a given experiment is defined to be the one that minimizes  $\sigma^2$ . (In Part 1, we used a different definition for "best" fit of symmetric waves.) As mentioned above,  $\sigma^2$  has several local minima in this larger space, but we start near what we believe to be the global minimum by starting at the values for these parameters found in steps 1-5.

Our experience has been that this six-step algorithm found the best KP solution for each of the fifteen available data sets for asymmetric waves. The results of the algorithm are discussed in §5. (It also converged to the best solution for the data from sixteen other experiments on symmetric waves. We will present these results elsewhere.)

Our justification for this algorithm is that it works: for each experiment on which we tested it, the algorithm found a best KP solution, with an acceptable error ( $\sigma$ ). However, Boris Dubrovin has suggested another possible justification for the algorithm, as follows. [The rest of this paragraph is a series of speculations, which we hope to verify eventually.] Subject to some extra conditions like (1), the KP equation is a completely integrable Hamiltonian system, along the lines discussed by Dubrovin (1991, pp. 79-92). Every exact reduction of KP to a finite-dimensional system ought to be completely integrable as well. A KP solution of genus 2 is such a reduction, it has two phases, so it ought to correspond to an integrable Hamiltonian system with two degrees of freedom. Therefore, a specification of the general KP solution of genus 2 ought to contain two "action"-type variables, and two "angles". Steps 1-3 of this algorithm specify the spatial structure,  $\{\mu_1, \mu_2, v_1, v_2\}$ . The other four variables  $\{b, d; \Phi_1, \Phi_2\}$  describe the dynamical system. Step 4, which ignores phase information, apparently finds action-type variables  $\{b, d\}$ , while step 5 finds angles  $\{\Phi_1, \Phi_2\}$ . This argument suggests that step 4 would also work if the maximum and minimum values of the data set were replaced by two conserved integrals of the KP equation. In fact, it might work better.

## References

- M.J. Ablowitz & H. Segur, Solitons and the Inverse Scattering Transform, SIAM, Philadelphia, PA, 425 pp., 1981
- M.J. Ablowitz & J. Villarroel, *Stud. App. Math.*, **85**, pp. 195-213, 1991
- B.A. Dubrovin, *Russ. Math. Surveys*, **36**, pp. 11-92, 1981
- B.A. Dubrovin, Geometry of Hamiltonian Evolutionary Systems, (lectures at University of Naples), Bibliopolis, Naples, 129 pp., 1991
- P.T. Boggs, R.H. Byrd, J.E. Rogers, & R.B. Schnabel, User's Reference Guide for ODRPACK Version 2.01, NISTIR 92-4834, U.S. Dep't of Commerce, 1992
- J. Guckenheimer & P. Holmes, Nonlinear Oscillations. Dynamical Systems, and Bifurcation of Vector Fields, Springer-Verlag, N.Y., 459 pp., 1983
- J. Hammack, N Scheffner, & H. Segur, *J. Fluid Mech.*, **209**, pp. 567-589, 1989
- J. Hammack, N Scheffner, & H. Segur, *J. Geoph. Res.*, **96**, pp. 4909-4914, 1991
- B.B. Kadomtsev & V.I. Petviashvili, *Sov. Phys. Doklady*, **15**, pp. 539-541, 1970
- I.M. Krichever, *Russ Math. Surveys*, **32**, pp. 185-213, 1977
- D.H. Peregrine, *Ann Rev. Fluid Mech.*, **15**, pp. 149-178, 1983
- D.H. Peregrine, *Proc. Roy. Soc. London.*, **400**, pp. 1-18, 1985
- M.M. Piexoto, *Topology*, **1**, pp. 101-120, 1962
- N. Scheffner, Misc. Pap. CERC-88-4, Vicksburg, MS, 1988
- H. Segur & A. Finkel, *Stud. App. Math.*, **73**, pp. 183-220, 1985
- G.G. Stokes, *Trans. Camb. Phil. Soc.*, **8**, pp. 441-455, 1847 (*Papers*, **1**, pp. 197-219)
- R.L. Wiegel, *J. Fluid Mech.*, **7**, pp. 273-286, 1960

## Figure Captions

Figure 1. Mosaic of two overhead photographs, showing surface patterns of waves in shallow water. Experiment: (a) KP38.50204; (b) KP400203-300303; (c) KP220203-110403. Each of these wave patterns has a basic hexagonal template; one such hexagon is drawn in Figure 1b.

Figure 2. Schematic (planform) view of the wave basin, showing its segmented wavemaker ( $\Lambda\Lambda\Lambda$ ), uniform-depth section ( $h = 20$  cm), and 1:30 sloping beach section. The locations of the wave-gauges were as follows:

gauge	X(m)	Y(m)	gauge	X(m)	Y(m)	gauge	X(m)	Y(m)
1	8	-8	2	8	-6	3	8	-4
4	8	-2	5	8	0	6	8	2
7	8	4	8	8	6	9	8	8
gauge	X(m)	Y(m)	gauge	X(m)	Y(m)	gauge	X(m)	Y(m)
10	2	0	11	6.5	0	12	7	0
13	7.5	0	14	8.5	0	15	9	0
16	9.5	0	17	13	0	18	16	0

Figure 3. Data from the nine-gauge array, for three asymmetric wave patterns, including two shown in Figures 1b, c. Experiment: (a) KP400203-300303; (b) KP220203-110403; (c) KP300102-30•803.

Figure 4. FFTs (periodograms) in T of the wave records shown in Figure 3 for experiment KP220203-110403. Every FFT shows energy at the same two frequencies ( $f_1 = 0.36$  Hz,  $f_2 = 0.67$  Hz), plus their harmonics. The dominant harmonics have been identified in one FFT.

Figure 5. Detailed comparison of measured wave records with the best KP solution at the same locations, for 20 seconds of data from experiment KP400203-300303. The comparison began 30 seconds into the experiment.

Figure 6. Detailed comparison of measured wave records with the best KP solution, for 20 seconds of data from experiment KP220203-110403, beginning at 30 seconds.

Figure 7. For experiment KP220203-110403, contour lines of the best KP solution (identified in Figure 6) are superimposed on the photograph of Figure 2c. The experiment and the KP solution are the same as in Figure 6, but different data are compared. The direction of propagation of the entire wave pattern, based on (8) is also shown.

Figure 8. For experiment KP300102-30•803, a detailed comparison of measured wave records with the best KP solution, during two different time intervals. a) 20 seconds of data beginning at 30 seconds; b) 20 seconds of data beginning at 70 seconds.

Figure 9. Temporal FFTs of the seven wave records obtained from the second gauge array, for experiment KP220203-110403.

Figure 10. Superposition of the measured wave records from the seven-gauge array, and the wave pattern predicted by the KP solution chosen to fit the data from the nine-gauge array, for experiment KP220203-110403.

Figure 11. Aerial photograph of waves off the southern coast of Long Island. The beach is between Lido Beach and Point Lookout, west of Jones Inlet. Beyond the surf zone, the wave patterns are two-dimensional, and approximately periodic. They have flat troughs, sharp crests, and approximately hexagonal shape.



**Figure 12.** Oblique nonlinear interaction of two waves in shallow water, off the coast of Oregon. The interaction occurred in water about 1 m. deep. [Photograph courtesy of T. Toedtemeier]

**Figure 13.** Aerial photograph of waves in shallow water, south of the Oregon Inlet on Pea Island, off the coast of North Carolina.

[Photograph courtesy of C. Miller]

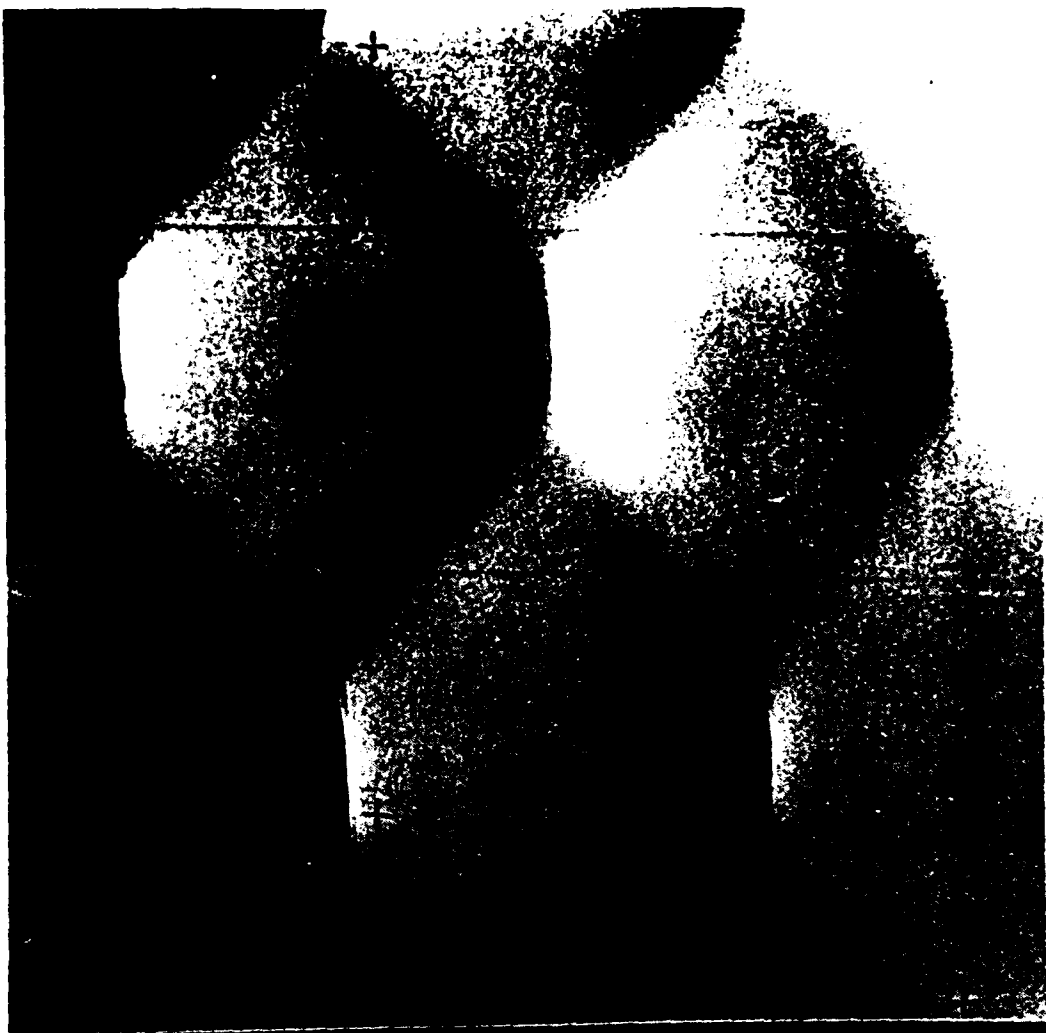
**Figure 14.** FFTs in Y of the wave records for experiment KP220203-110403, after extension as described in the text.

Table 1

Case	KP Parameters										Errors		
	-b	$\lambda$	-d	$\mu_1$	$\mu_2$	v1	v2	$\omega_1$	$\omega_2$	$\eta$ max	$\eta$ min	f max/U max	$\sigma$
000203_380203	4.56	0.403	3.95	0.602	0.600	0.004	-0.296	0.091	-0.355	5.81	-3.46	0.851	0.297
100203_150203	4.58	0.540	3.28	0.602	0.602	-0.115	0.073	0.029	0.069	5.66	-3.38	0.921	0.369
050203_050303	3.20	0.723	2.86	0.419	0.602	-0.038	0.037	-0.033	0.114	7.35	-3.24	0.666	0.402
150203_050303	3.42	0.580	3.23	0.421	0.601	-0.038	0.116	-0.052	0.029	6.84	-3.26	0.721	0.348
250203_100303	3.44	0.423	3.74	0.421	0.601	-0.076	0.191	-0.109	-0.110	7.50	-2.76	0.791	0.312
100203_250303	3.32	0.393	3.95	0.421	0.601	-0.191	0.076	-0.328	0.026	7.48	-2.56	0.815	0.305
200203_200303	3.39	0.365	3.98	0.421	0.601	-0.154	0.150	-0.237	-0.044	8.25	-2.74	0.723	0.312
300203_200303	3.44	0.295	4.11	0.420	0.601	-0.154	0.229	-0.235	-0.186	7.71	-2.90	0.789	0.267
220203_110403	2.89	0.382	4.12	0.322	0.601	-0.085	0.168	-0.139	-0.035	6.27	-3.11	0.843	0.282
350203_150303	3.49	0.302	4.14	0.421	0.601	-0.116	0.269	-0.155	-0.278	7.94	-2.83	0.755	0.283
400203_300303	3.47	0.196	4.27	0.421	0.601	-0.225	0.305	-0.414	-0.376	7.65	-3.58	0.822	0.312
300203_300102	4.46	0.377	6.29	0.601	0.933	0.232	-0.225	-0.137	0.551	5.80	-3.47	0.769	0.235
300203_300803	4.46	0.376	6.05	0.601	0.936	0.229	-0.232	-0.135	0.545	6.42	-3.77	0.720	0.311
250203_450102	4.49	0.353	6.47	0.600	0.933	0.189	-0.342	-0.045	0.342	5.48	-3.49	0.777	0.252
300102_30•803	6.50	0.413	5.97	0.933	0.932	-0.234	0.227	0.578	0.675	3.94	-2.89	0.887	0.248

Table 2

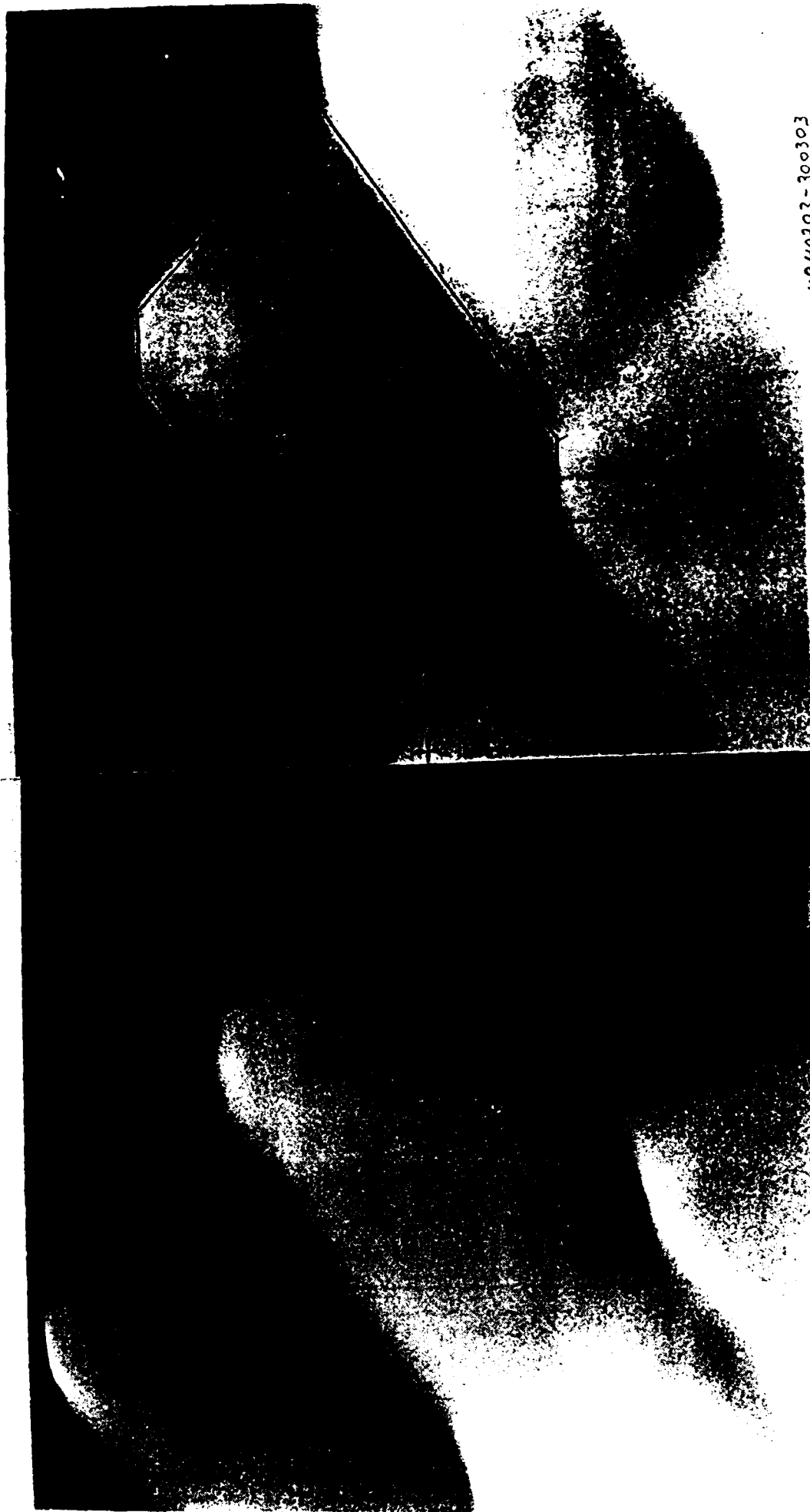
Case	Theoretical		Experimental		$\sigma$	$\sigma \chi$
	$dx/dt$	$dy/dt$	$dx/dt$	$dy/dt$		
000203_380203	-0.141	-1.484	-0.164	-1.503	0.297	0.326
100203_150203	-0.087	-0.202	-0.115	-0.171	0.369	0.403
050203_050303	-0.083	-1.771	-0.084	-1.953	0.402	0.422
150203_050303	0.067	-0.607	0.060	-0.609	0.348	0.358
250203_100303	0.231	-0.154	0.219	-0.167	0.312	0.350
100203_250303	0.123	-1.452	0.112	-1.460	0.305	0.307
200203_200303	0.271	-0.799	0.249	-0.805	0.312	0.316
300203_200303	0.436	-0.335	0.419	-0.338	0.267	0.314
220203_110403	0.251	-0.688	0.243	-0.685	0.281	0.319
350203_150303	0.403	0.133	0.387	0.126	0.283	0.299
400203_300303	0.800	-0.340	0.786	-0.333	0.308	0.282
300203_300102	-0.286	1.302	-0.291	1.308	0.235	0.287
300203_300803	-0.264	1.283	-0.277	1.293	0.311	0.316
250203_450102	-0.129	0.646	-0.144	0.663	0.252	0.305
300102_30*803	-0.618	0.008	-0.612	0.006	0.248	0.294



KP38 50204

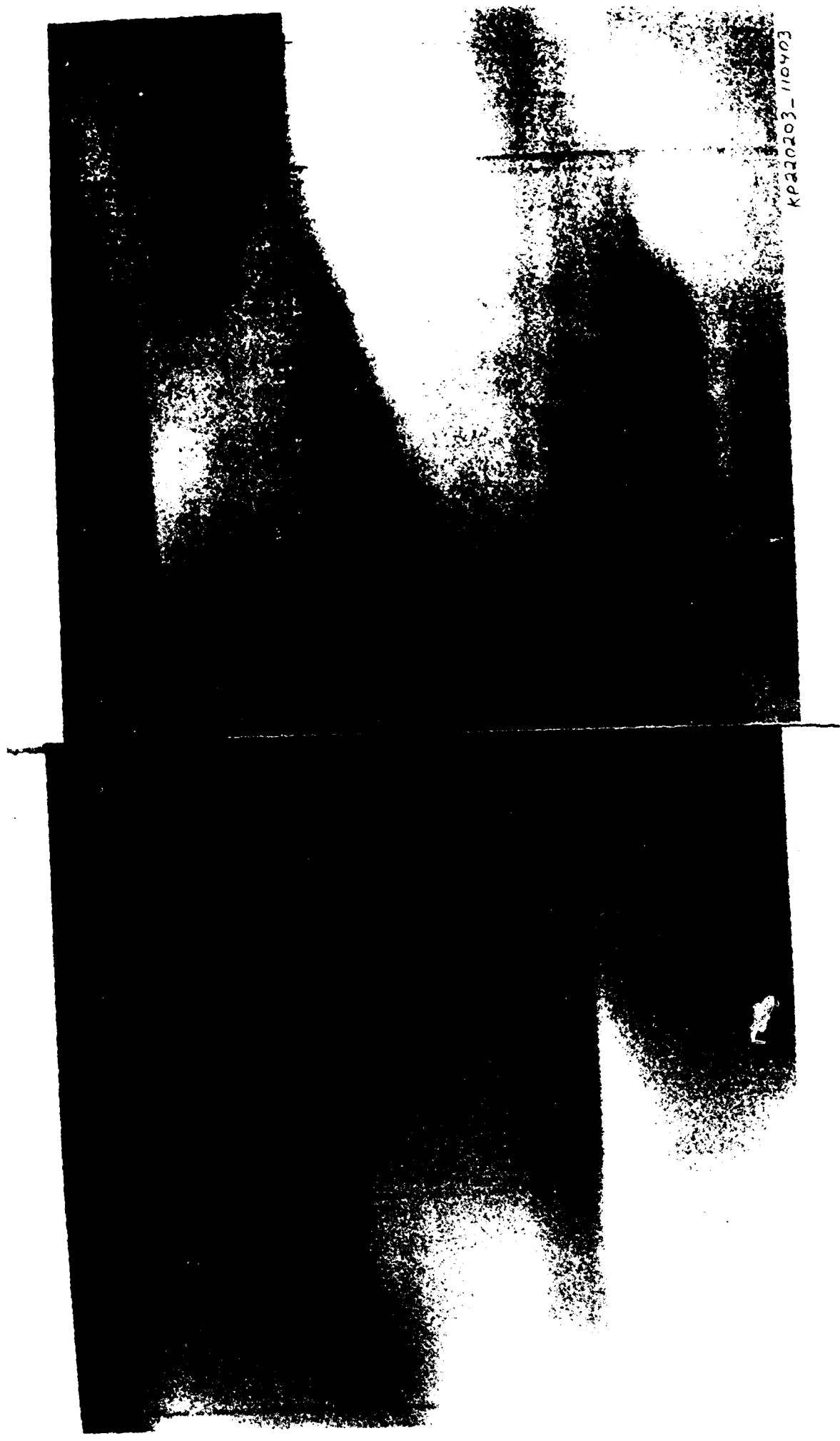


fig 1a



KP40203-300303

Fig 1b



KP220203-110403

Fig 1c

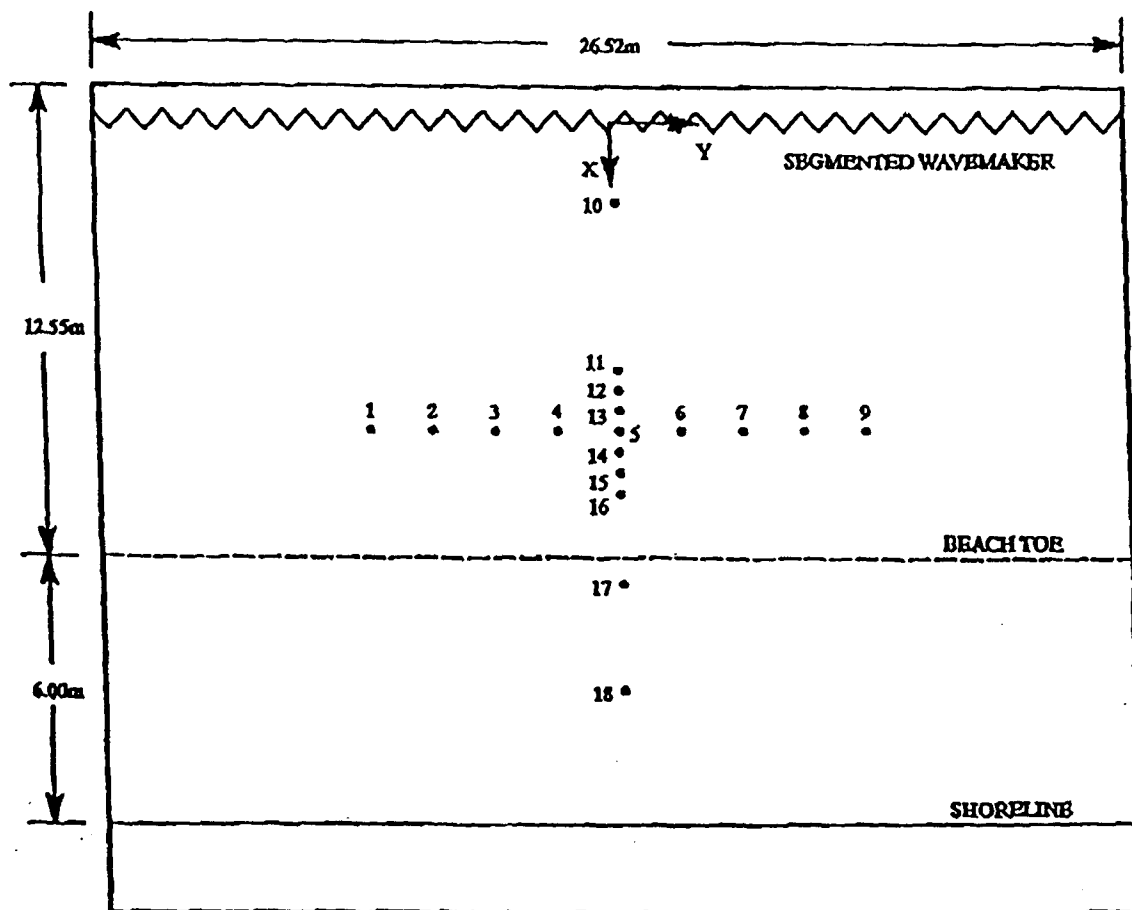
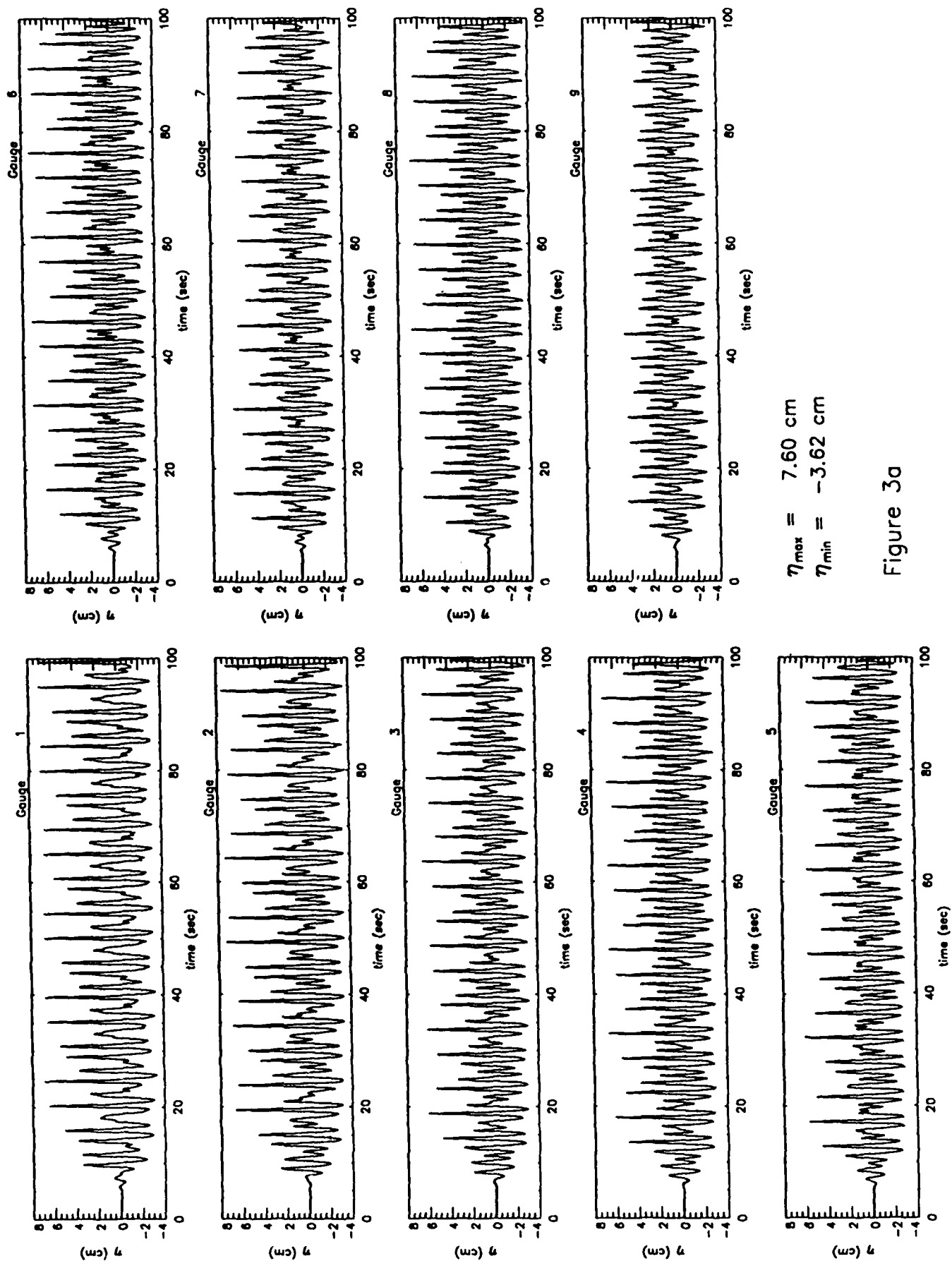


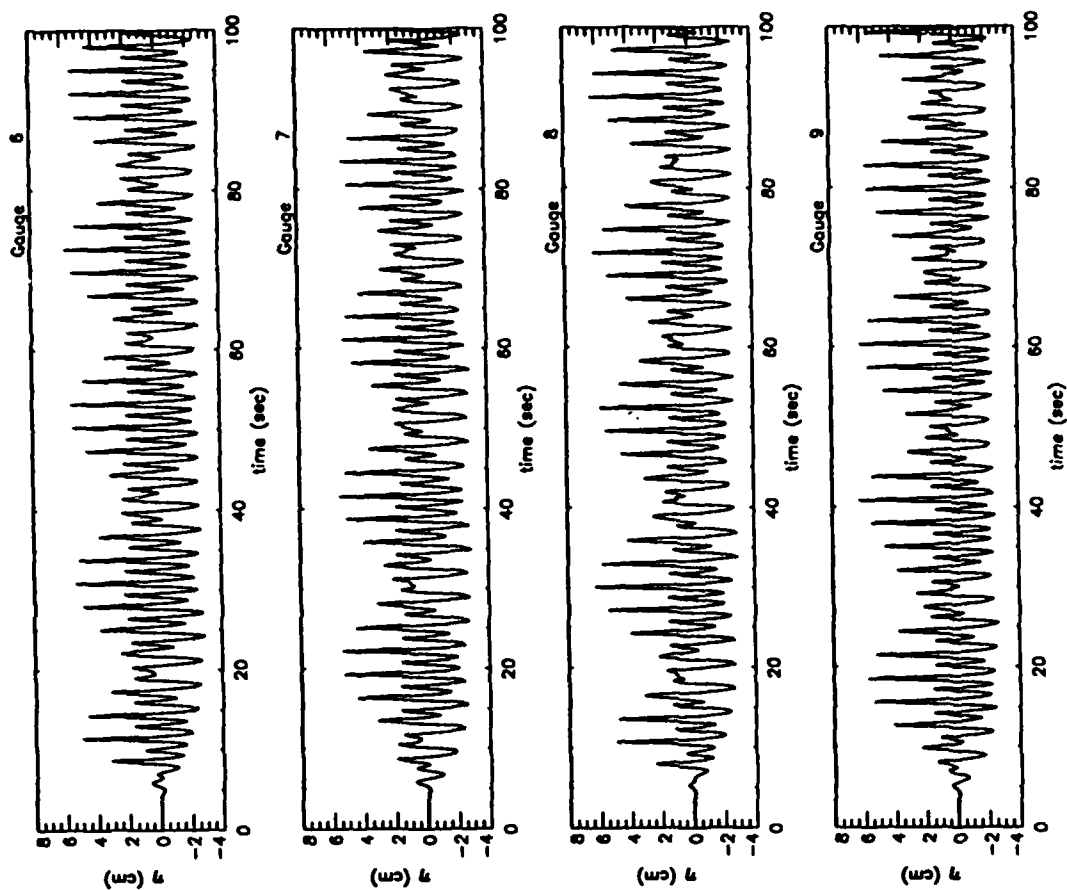
Figure 2



$\eta_{\max} = 7.60 \text{ cm}$   
 $\eta_{\min} = -3.62 \text{ cm}$

Figure 3a

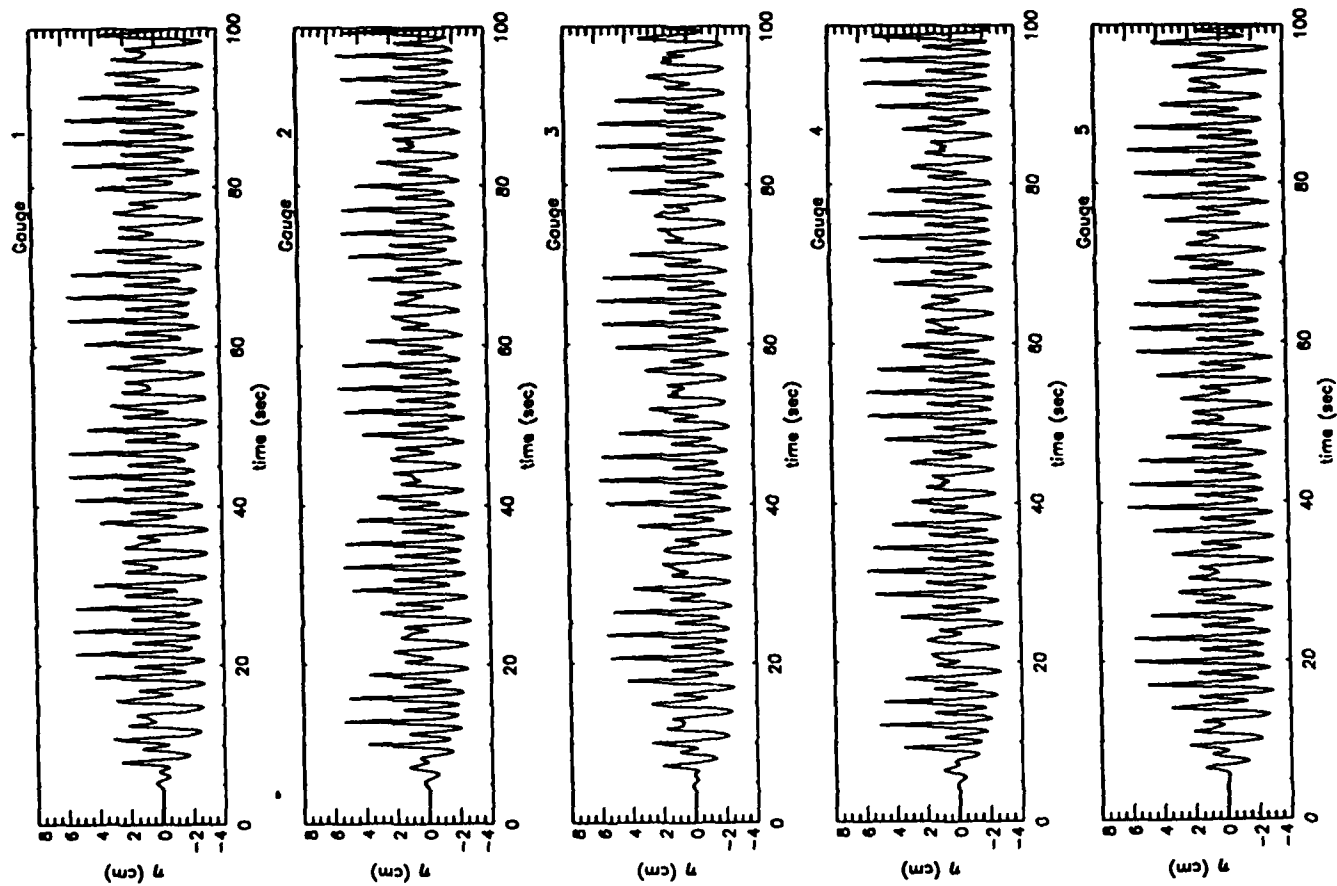


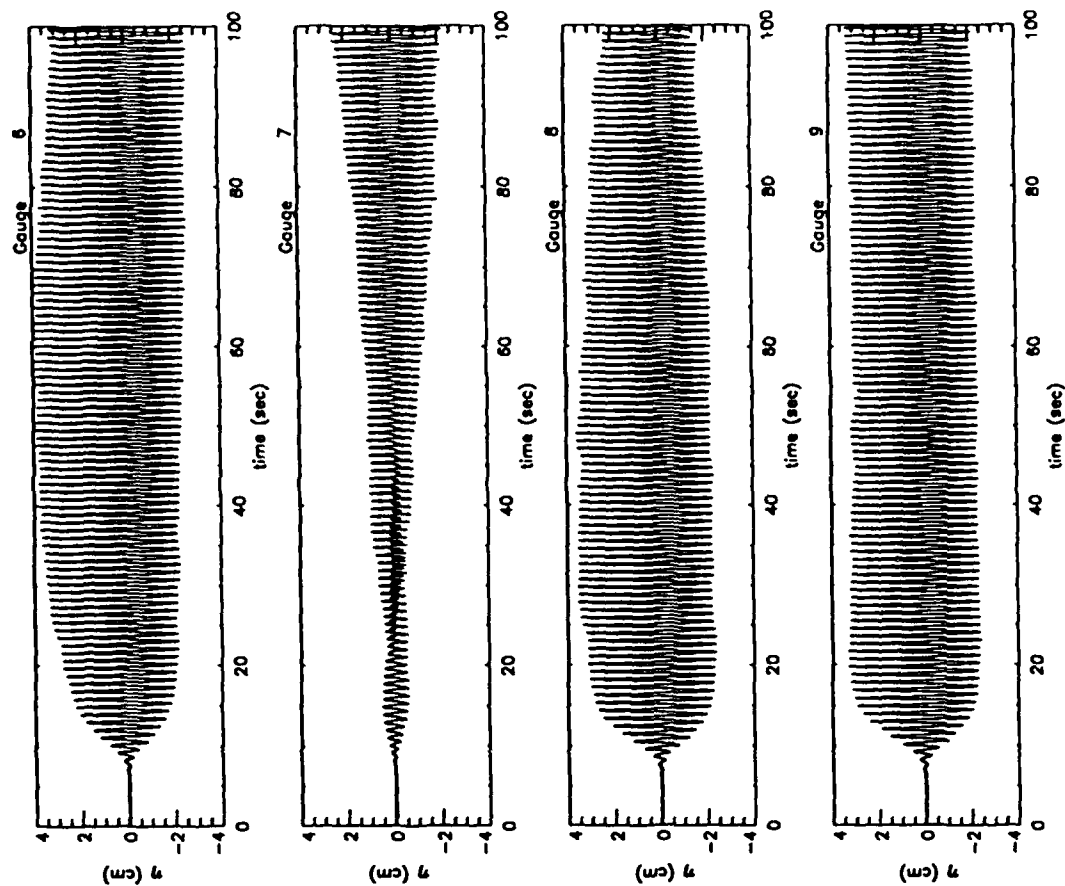
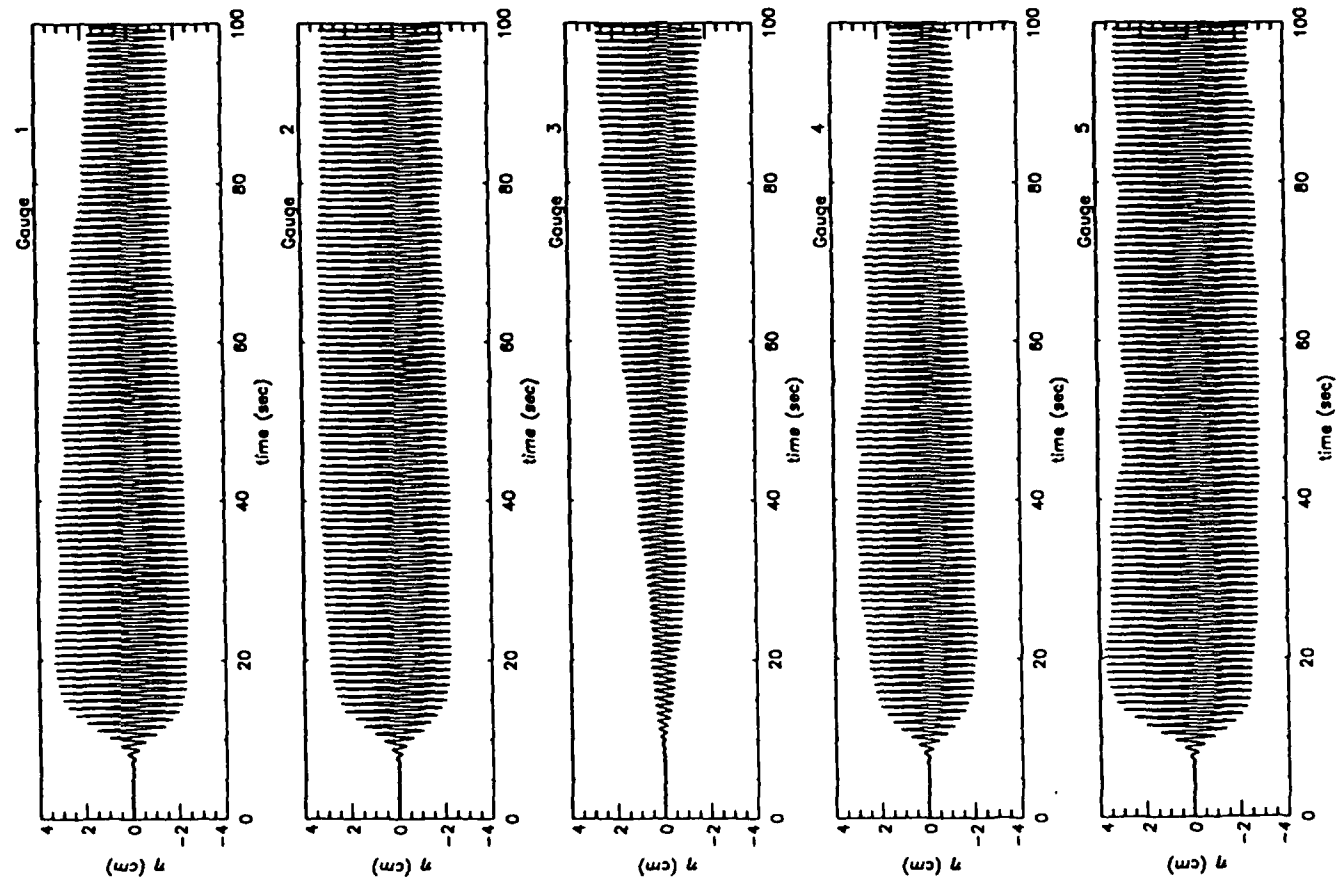


$$\eta_{\max} = 6.29 \text{ cm}$$

$$\eta_{\min} = -3.11 \text{ cm}$$

Figure 3b





$$\eta_{\max} = 3.96 \text{ cm}$$

$$\eta_{\min} = -2.88 \text{ cm}$$

Figure 3c

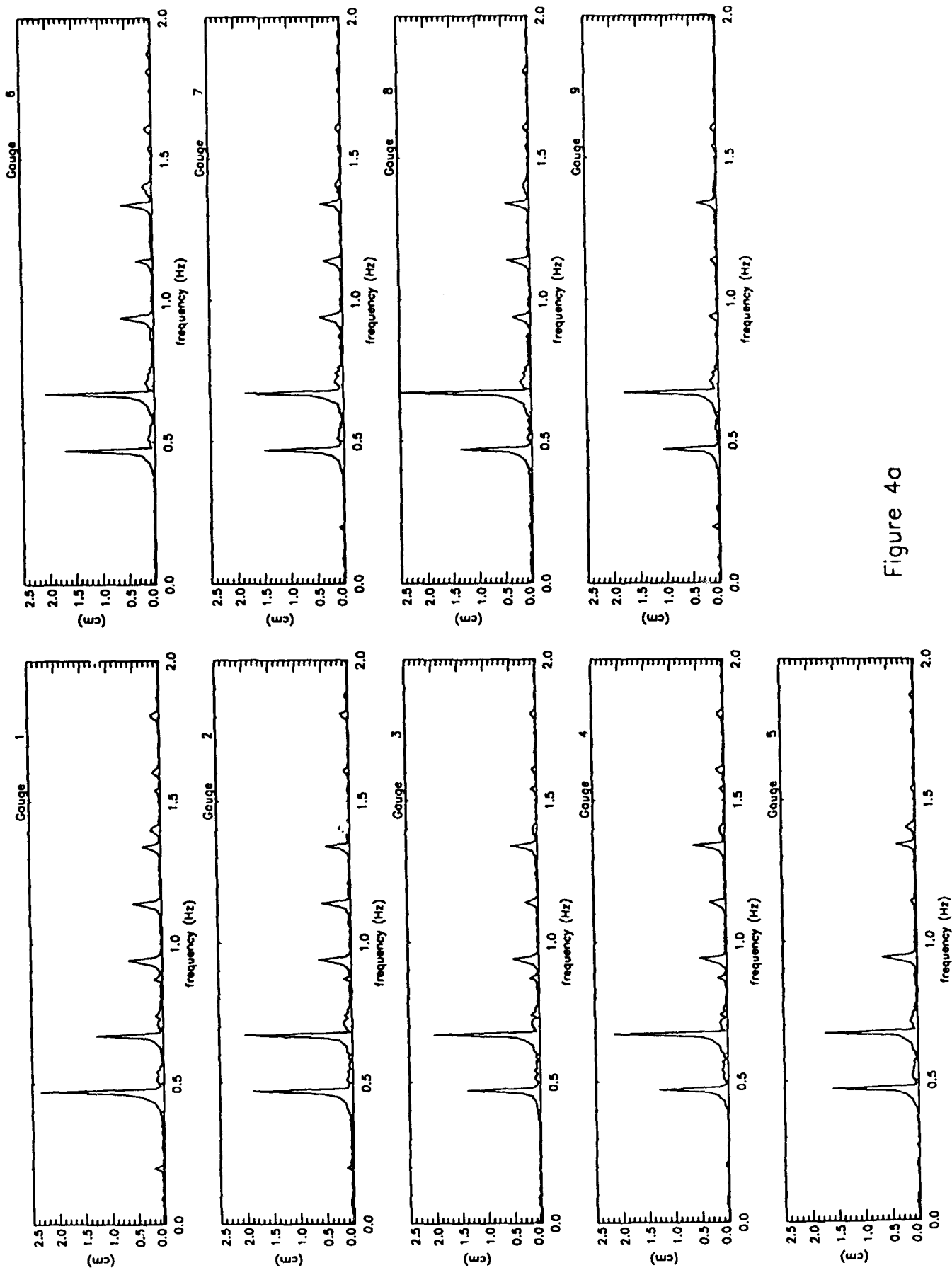


Figure 4a

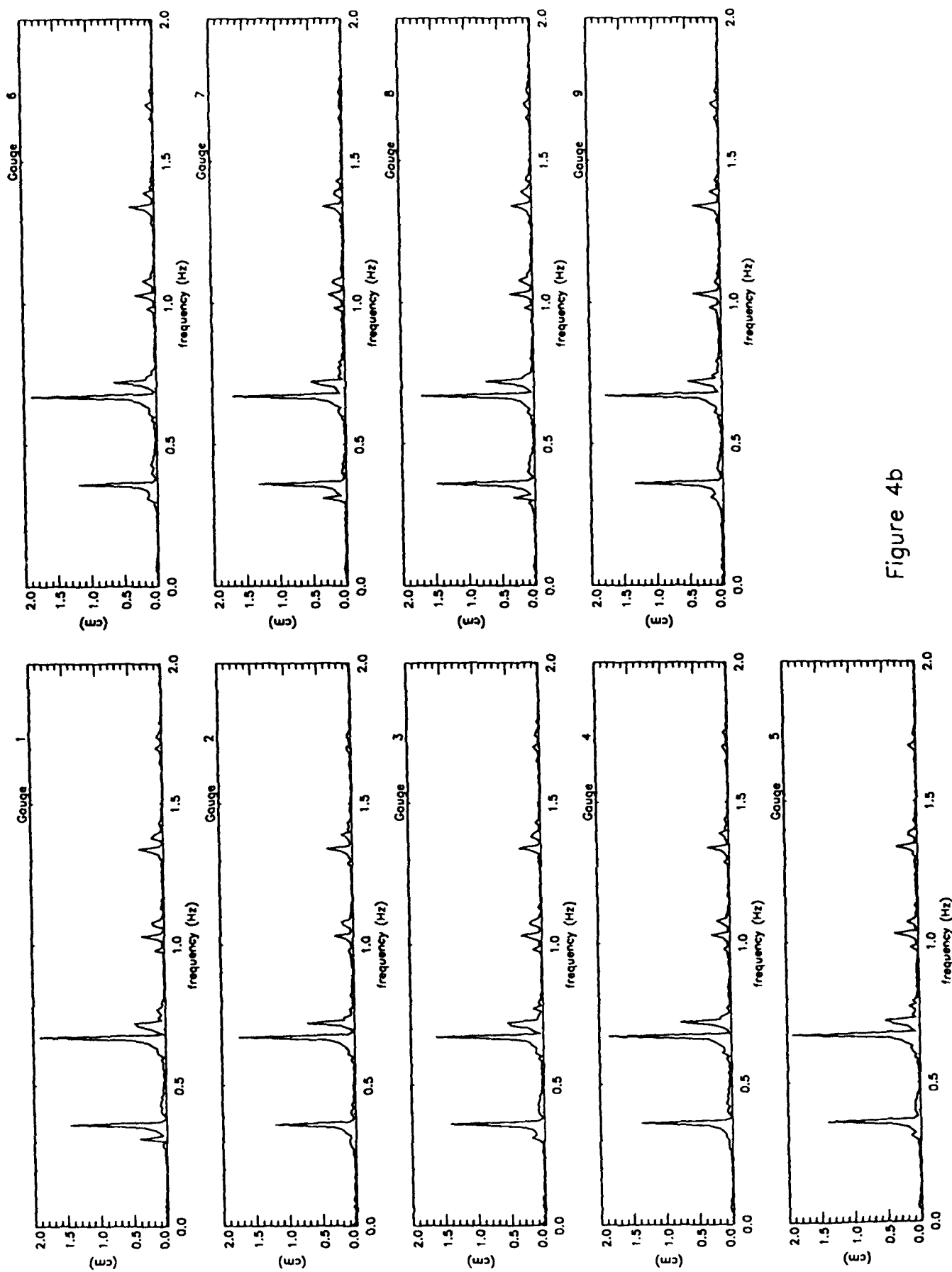


Figure 4b

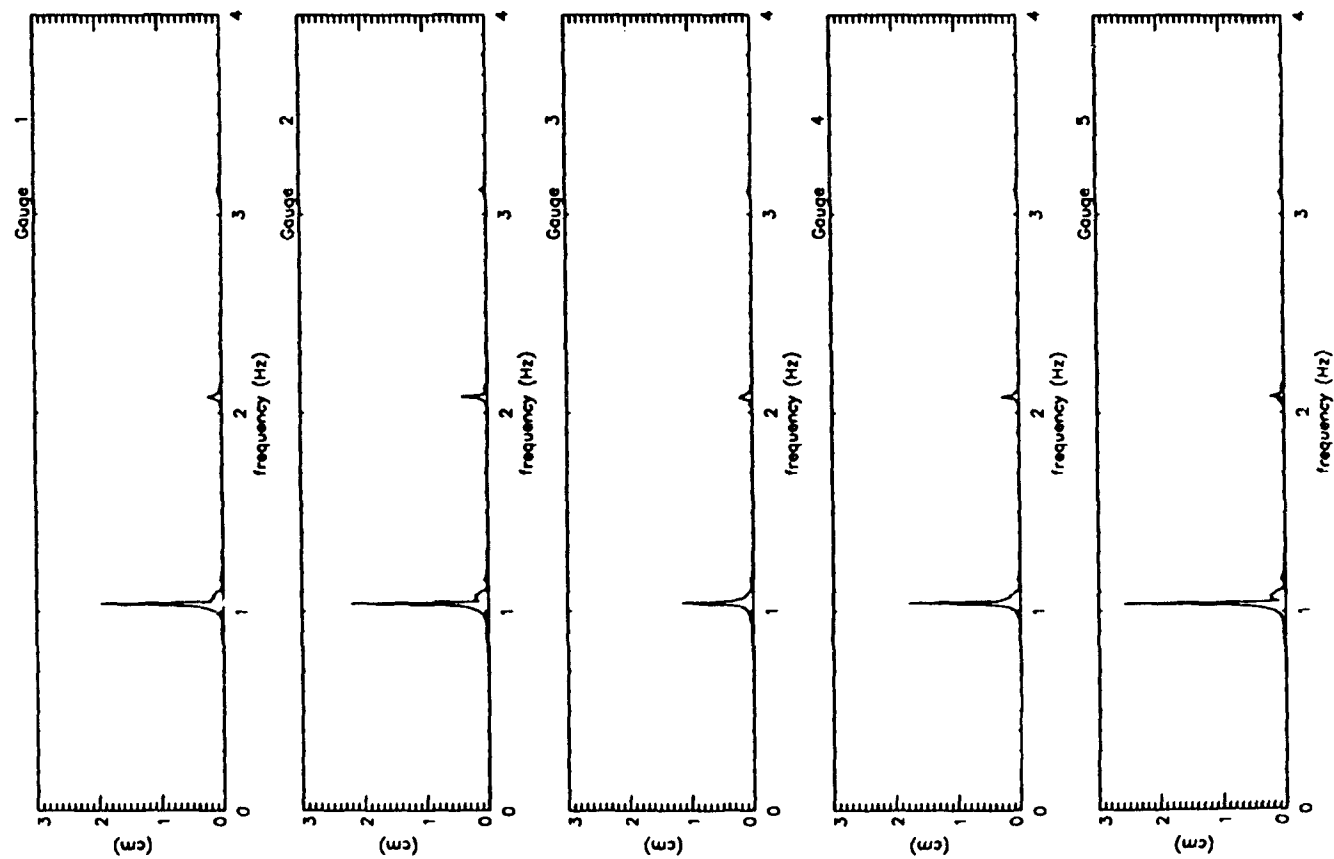
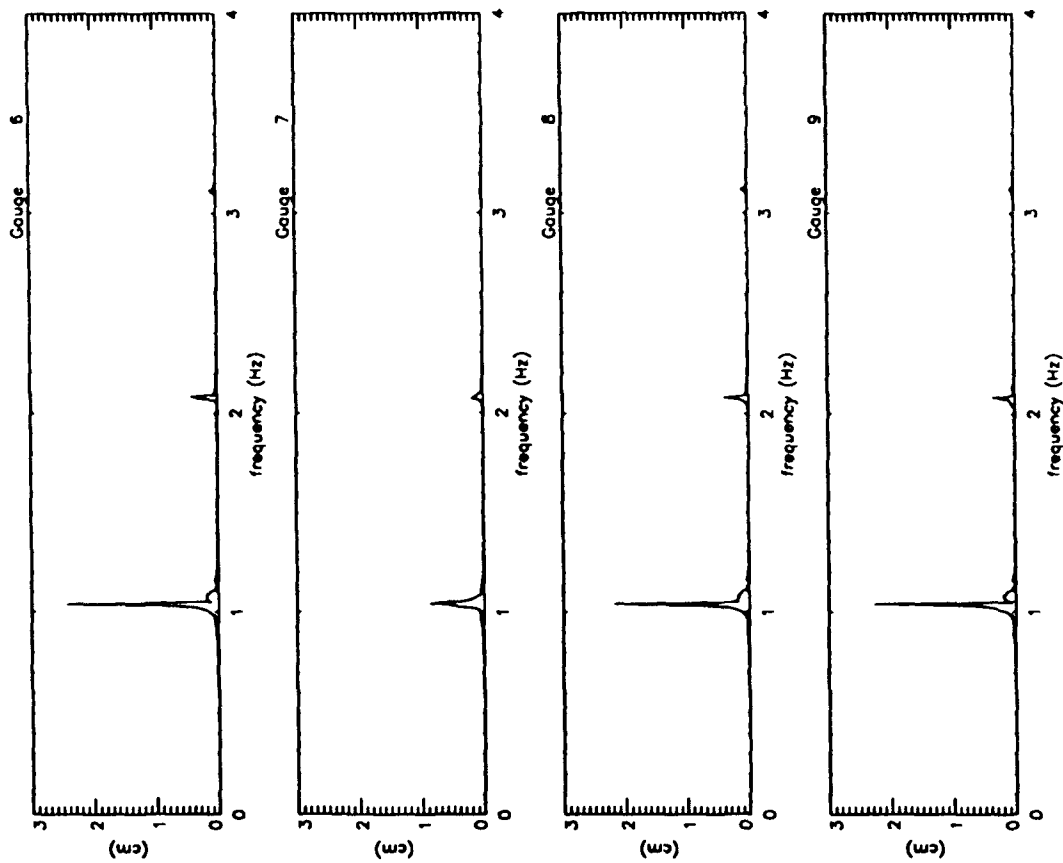


Figure 4c



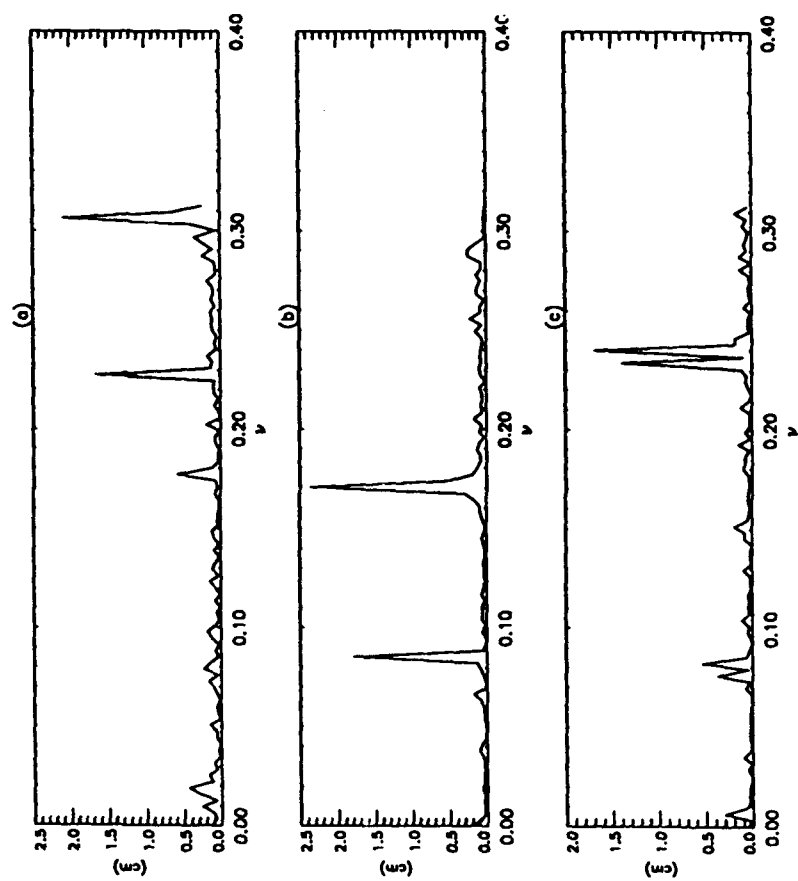


Figure 5

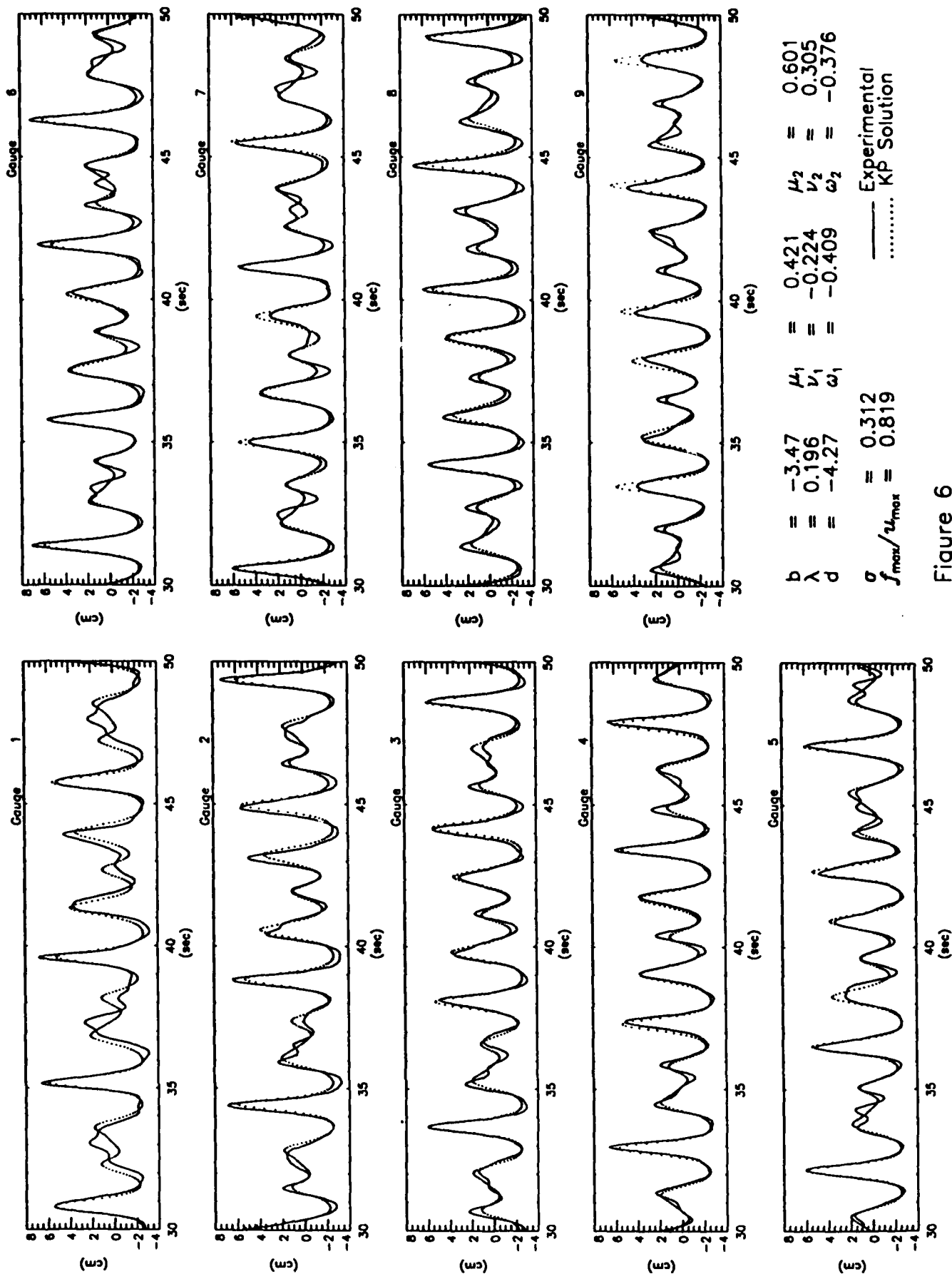


Figure 6

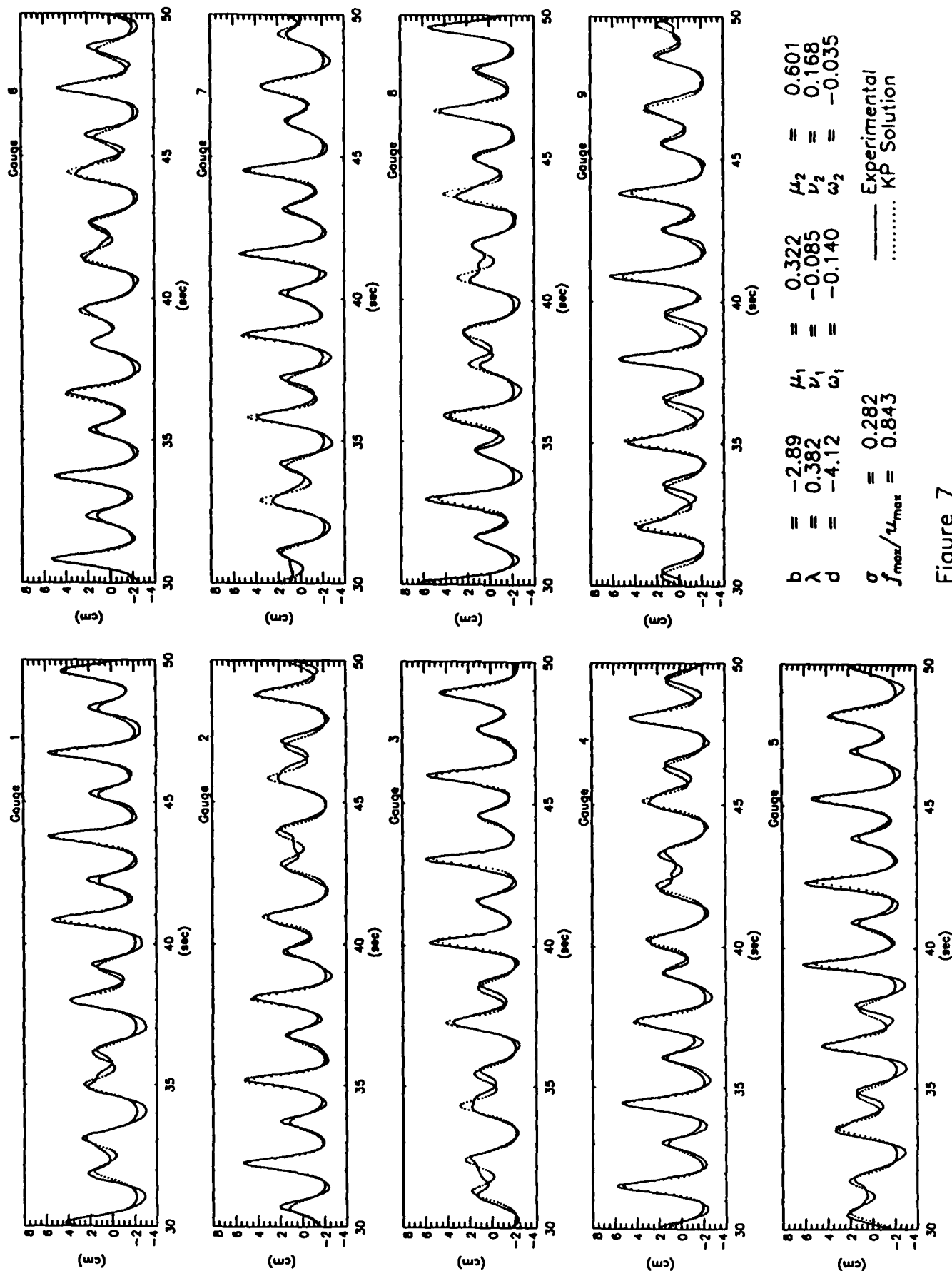


Figure 7



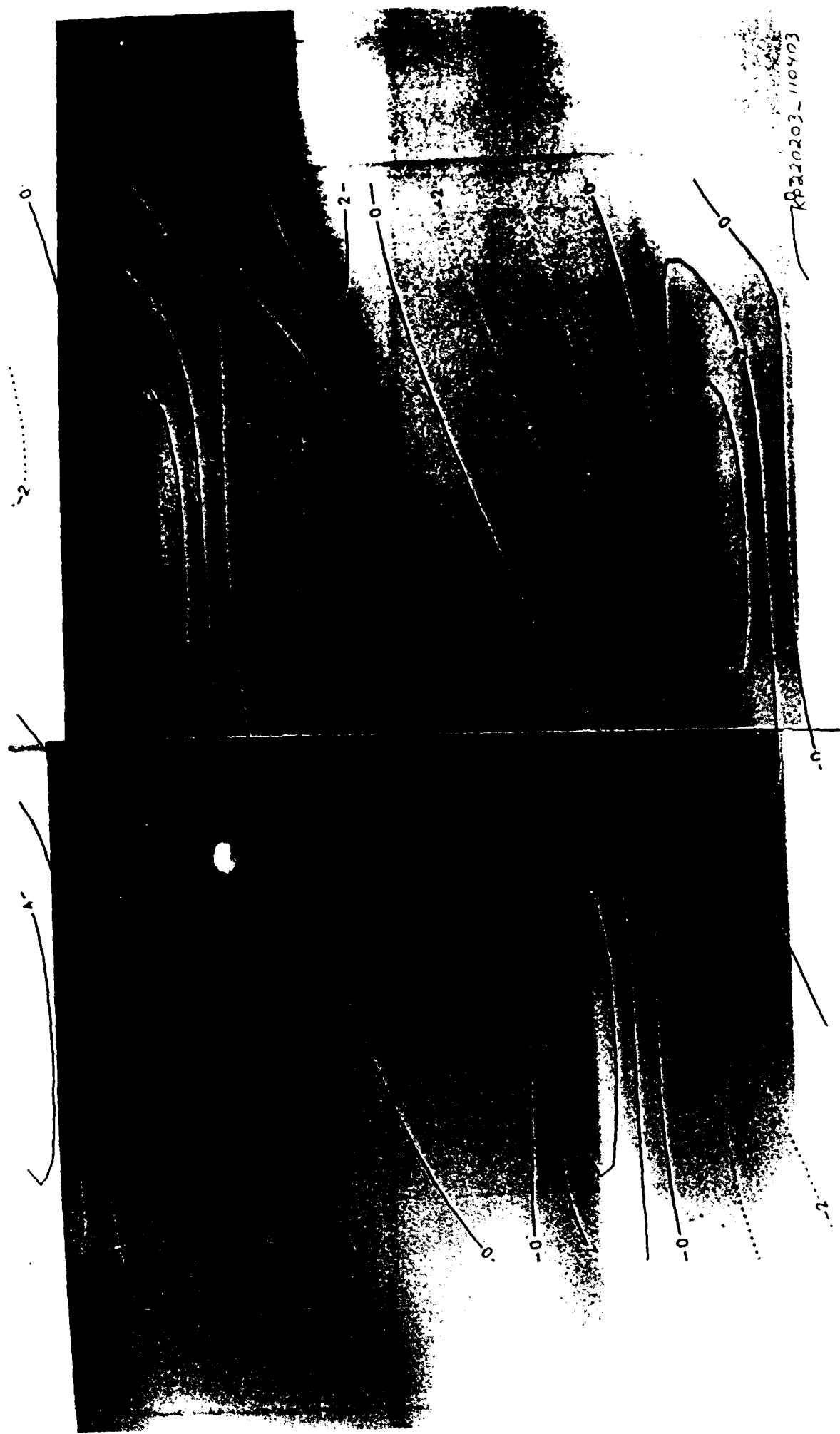
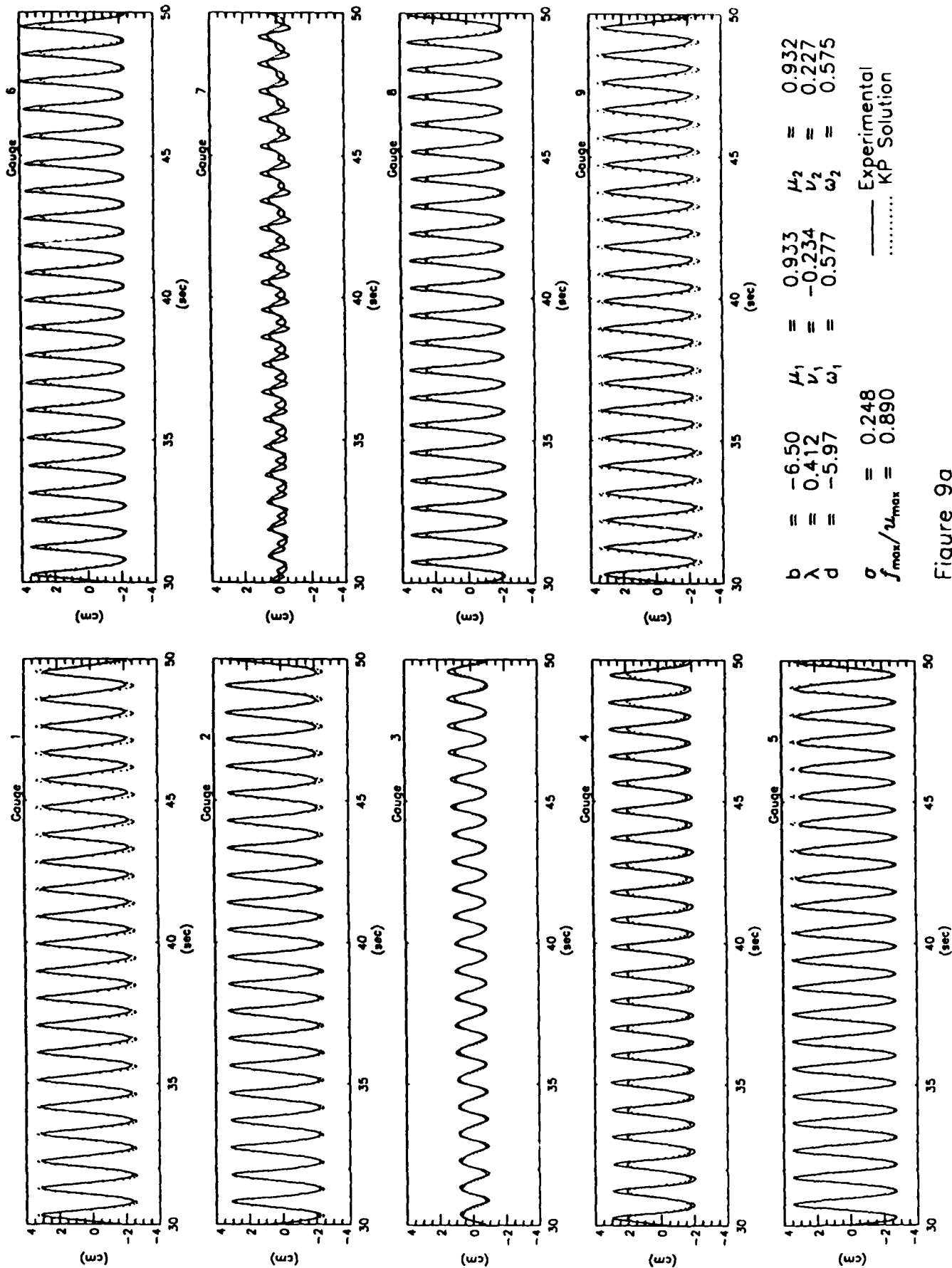
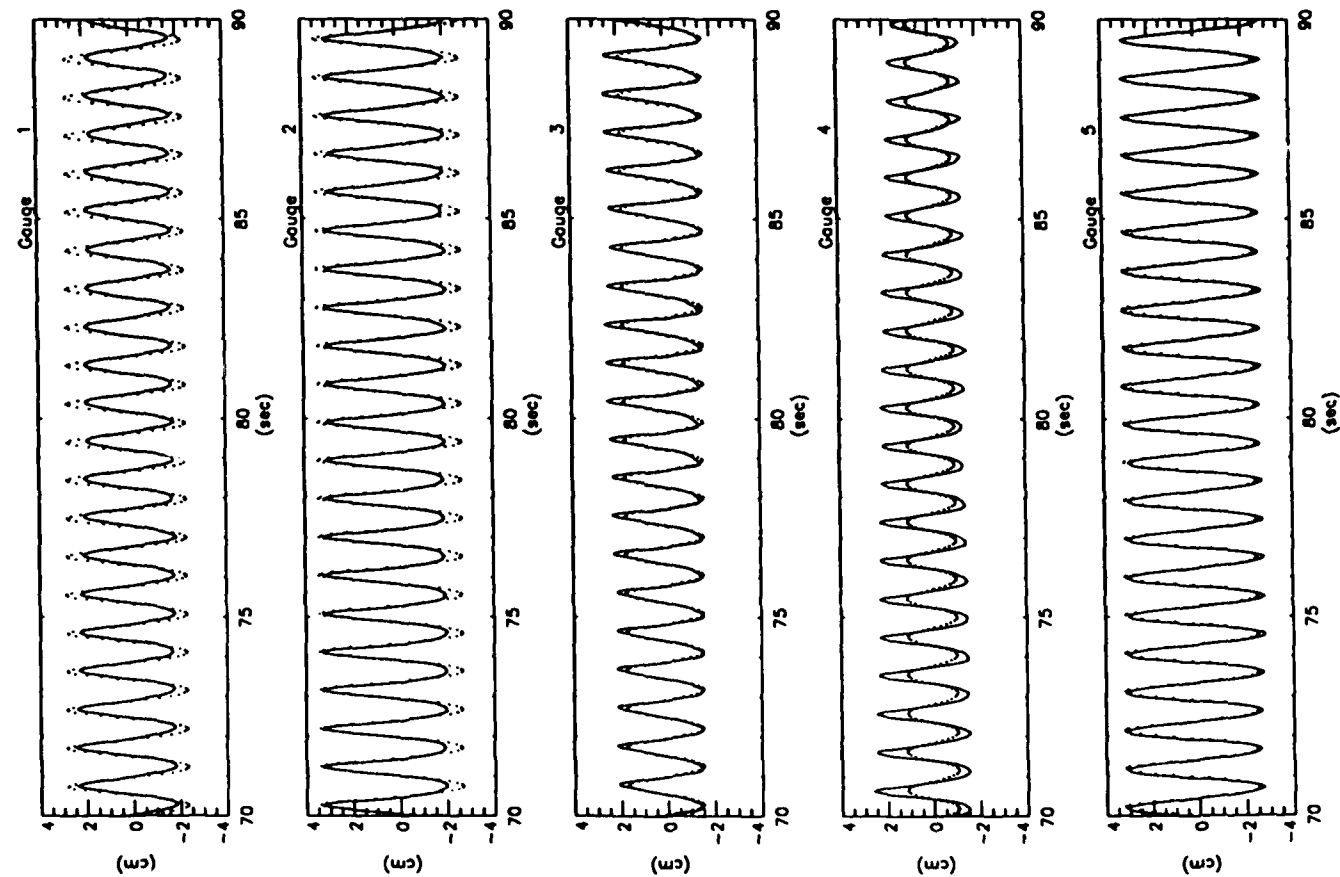


Figure 8 - KP220203\_110403



$$\begin{array}{llll}
 b & = & -6.50 & \mu_1 & = & 0.933 & \mu_2 & = & 0.932 \\
 \lambda & = & 0.412 & \nu_1 & = & -0.234 & \nu_2 & = & 0.227 \\
 d & = & -5.97 & \omega_1 & = & 0.577 & \omega_2 & = & 0.575 \\
 \sigma & & & & & & & & \\
 f_{\max}/2L_{\max} & = & 0.248 & & & & & & \\
 & & 0.890 & & & & & & 
 \end{array}$$

Figure 9a



$b$	$= -6.50$	$\mu_1$	$= 0.933$	$\mu_2$	$= 0.932$
$\lambda$	$= 0.412$	$\nu_1$	$= -0.234$	$\nu_2$	$= 0.227$
$d$	$= -5.97$	$\omega_1$	$= 0.577$	$\omega_2$	$= 0.575$
$\sigma$	$= 0.300$				
$f_{\max}/u_{\max}$	$= 0.902$				

— Experimental  
..... KP Solution

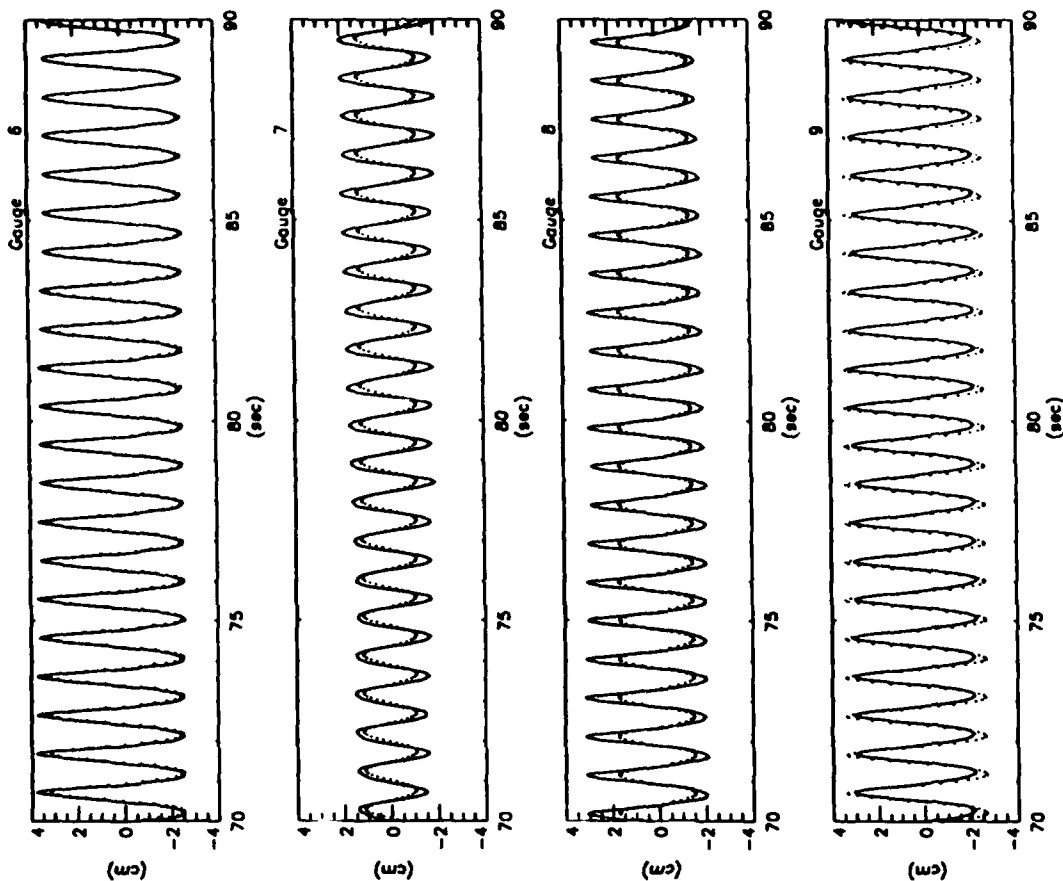


Figure 9b

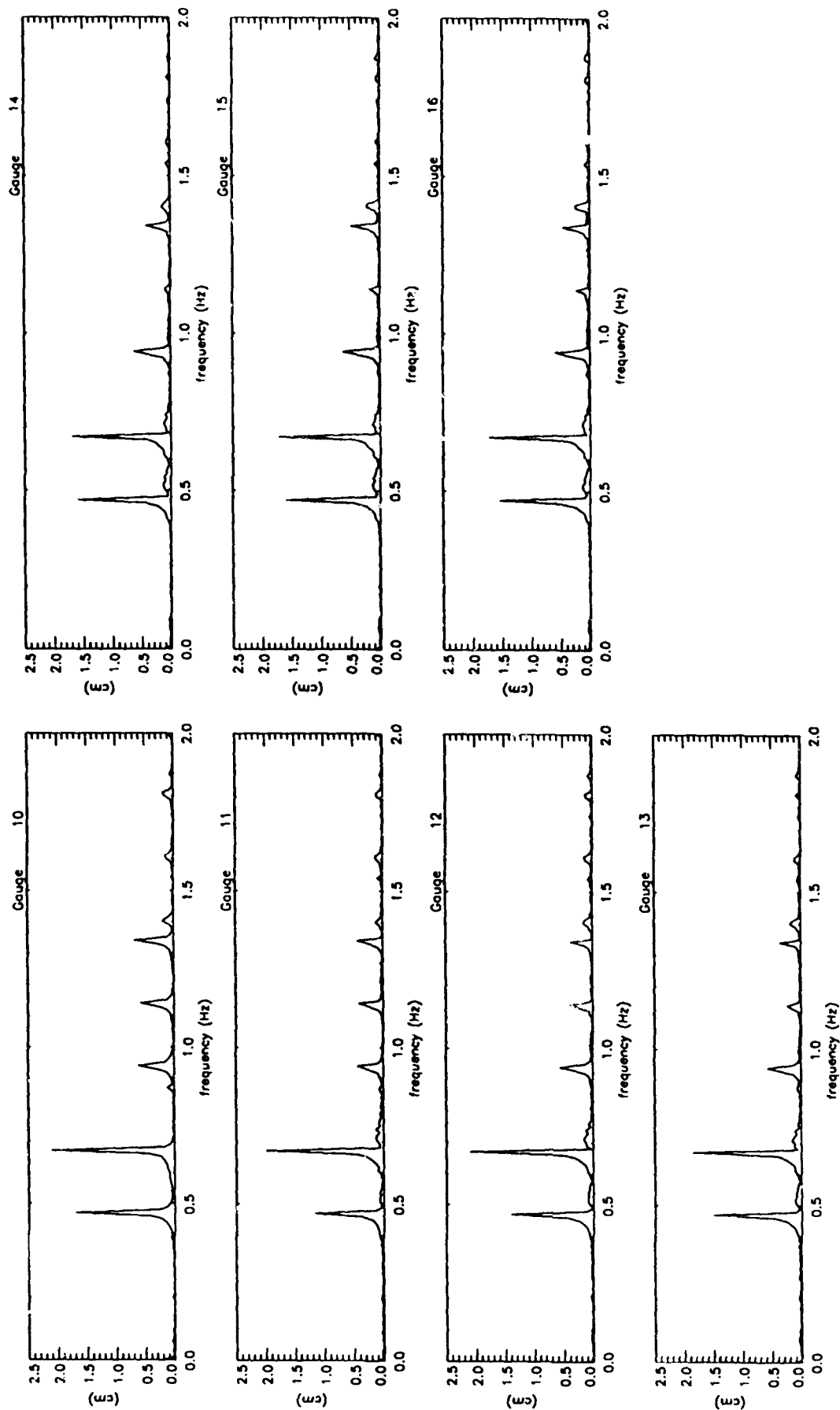


Figure 10a

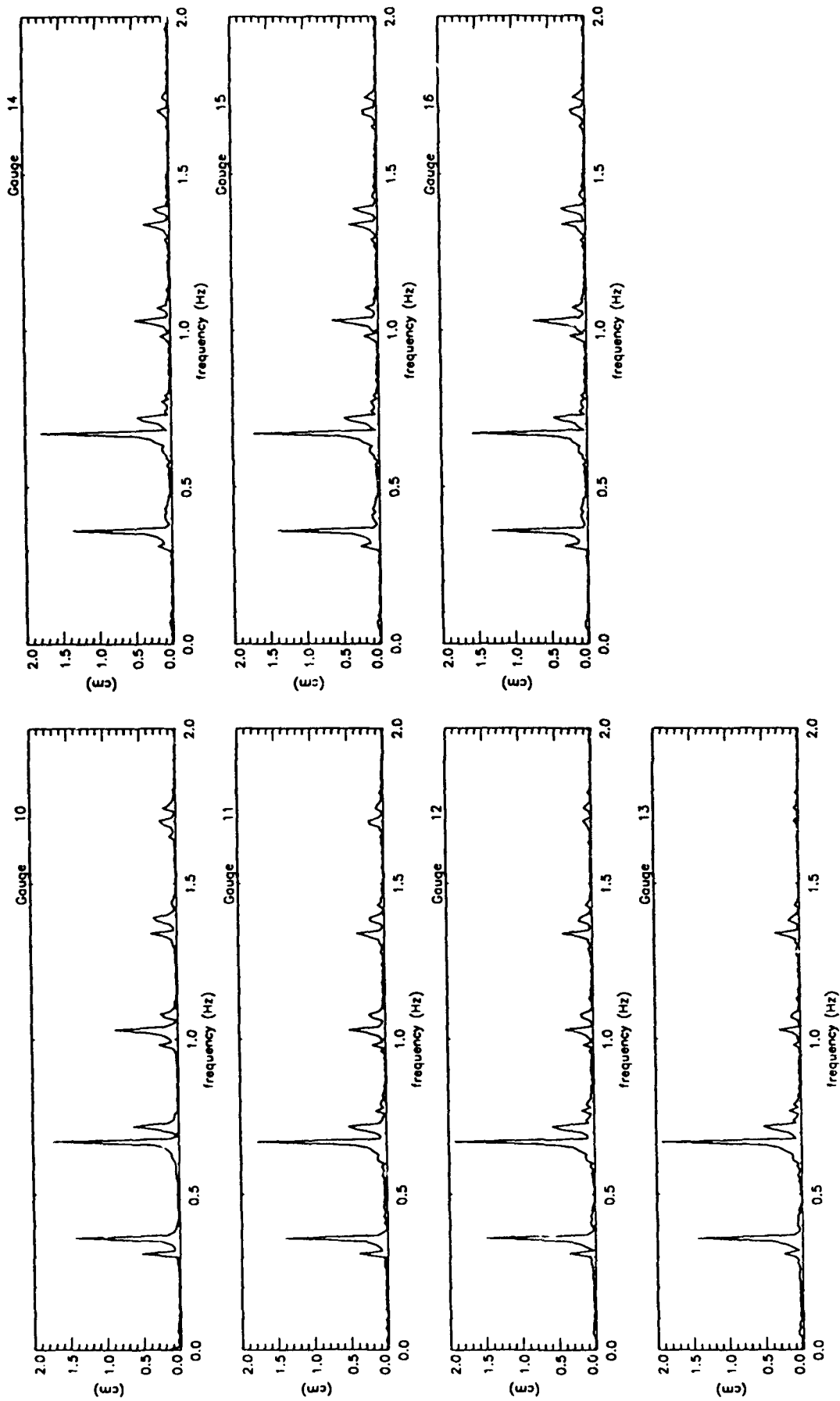


Figure 10b

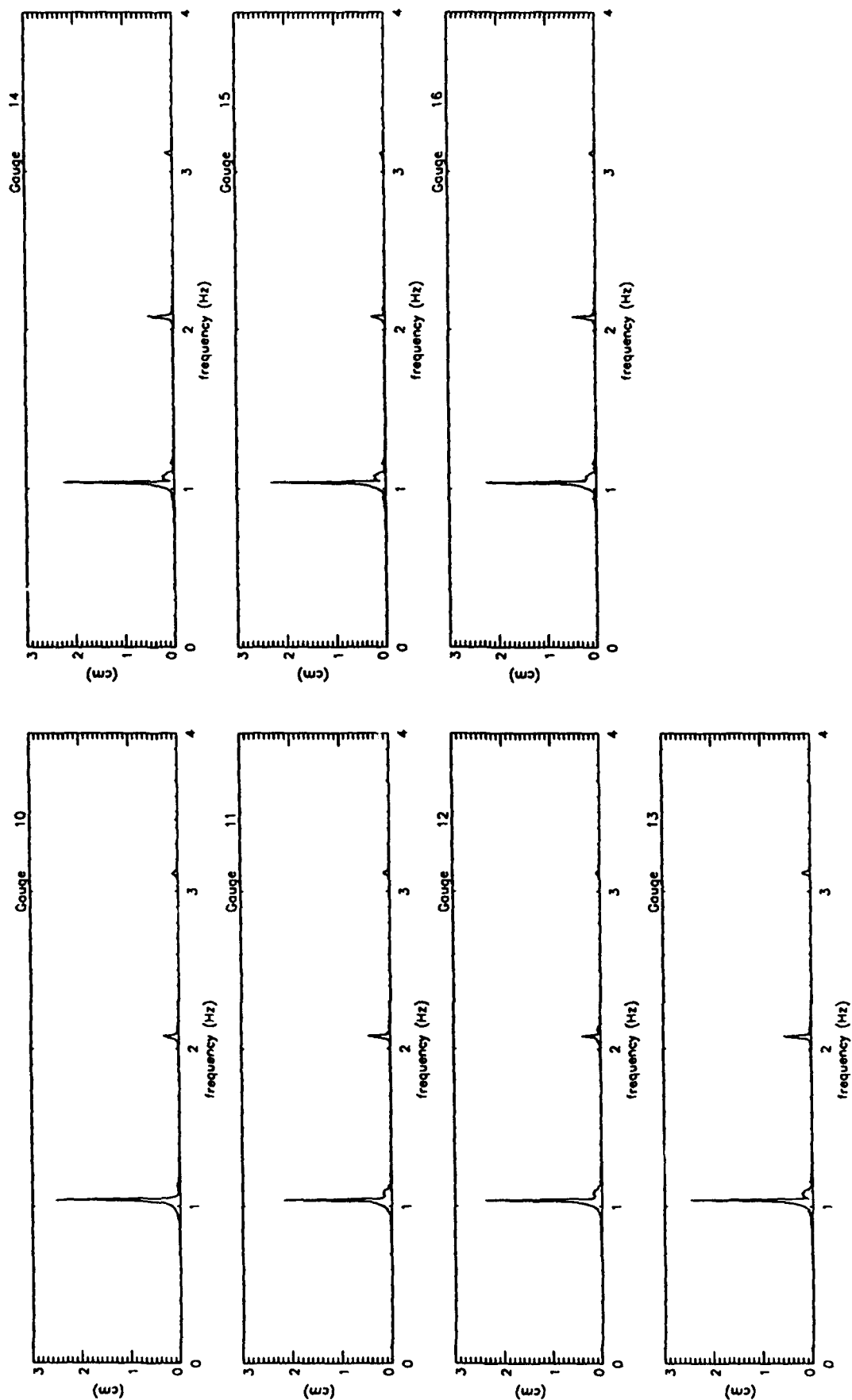


Figure 10c

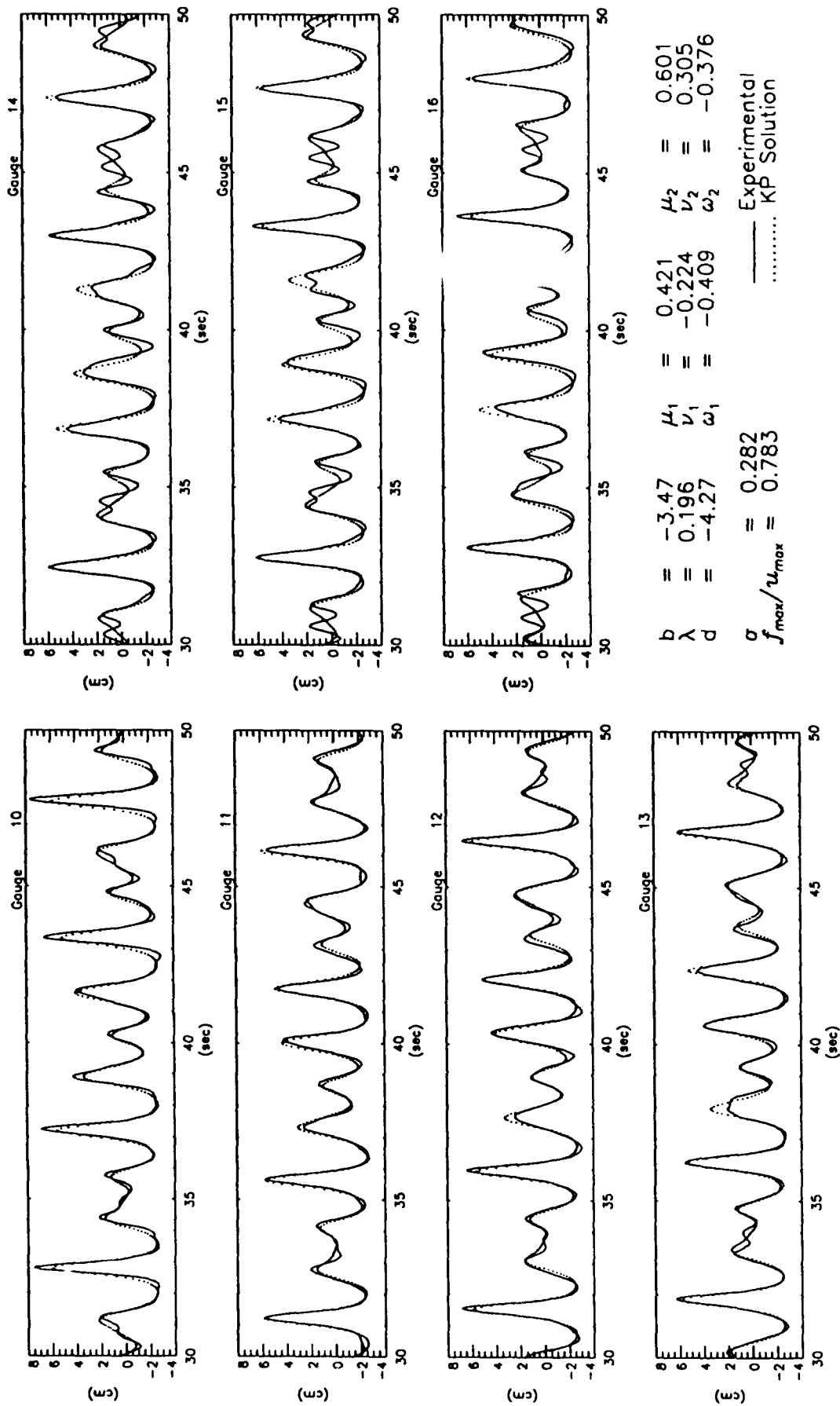


Figure 11a

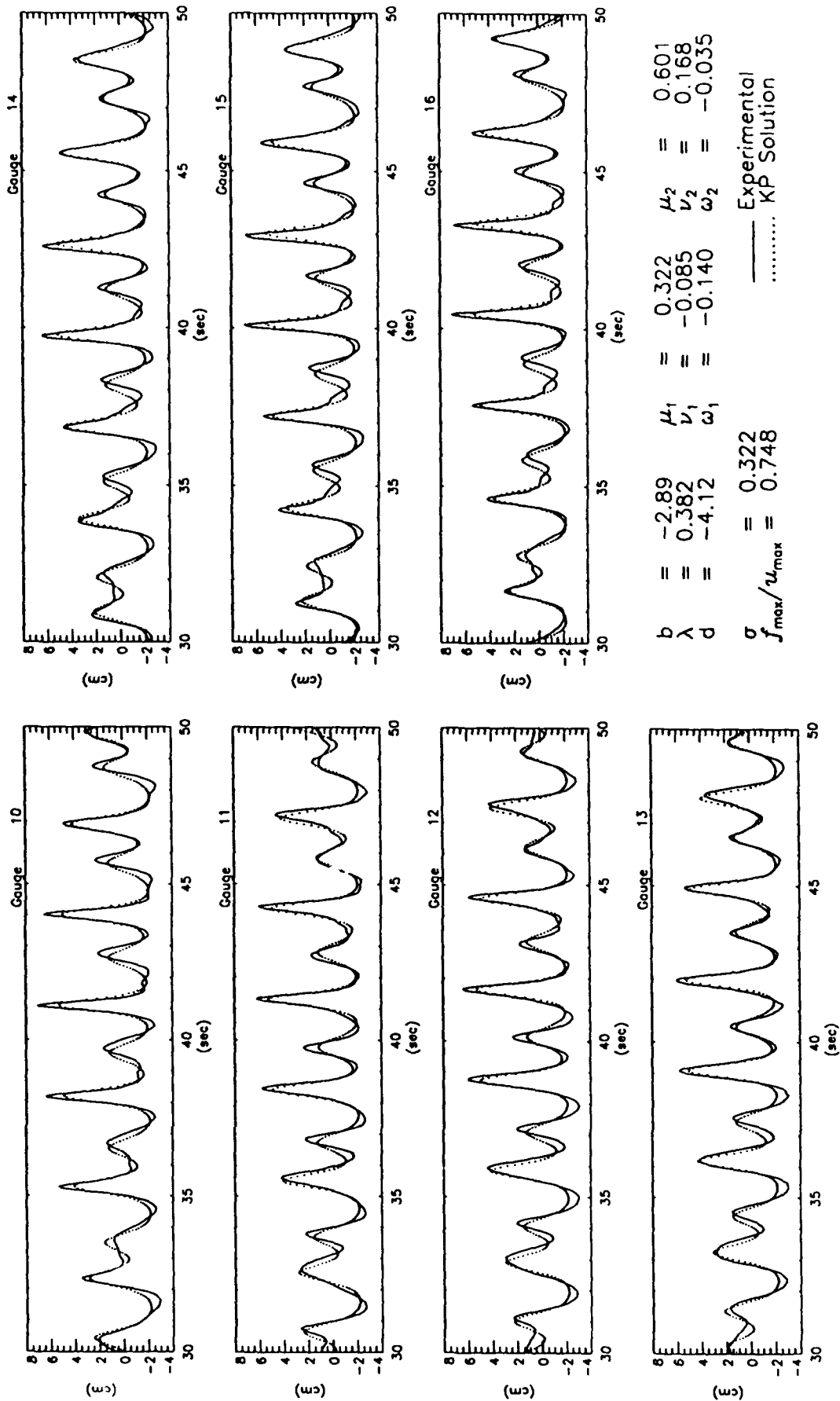
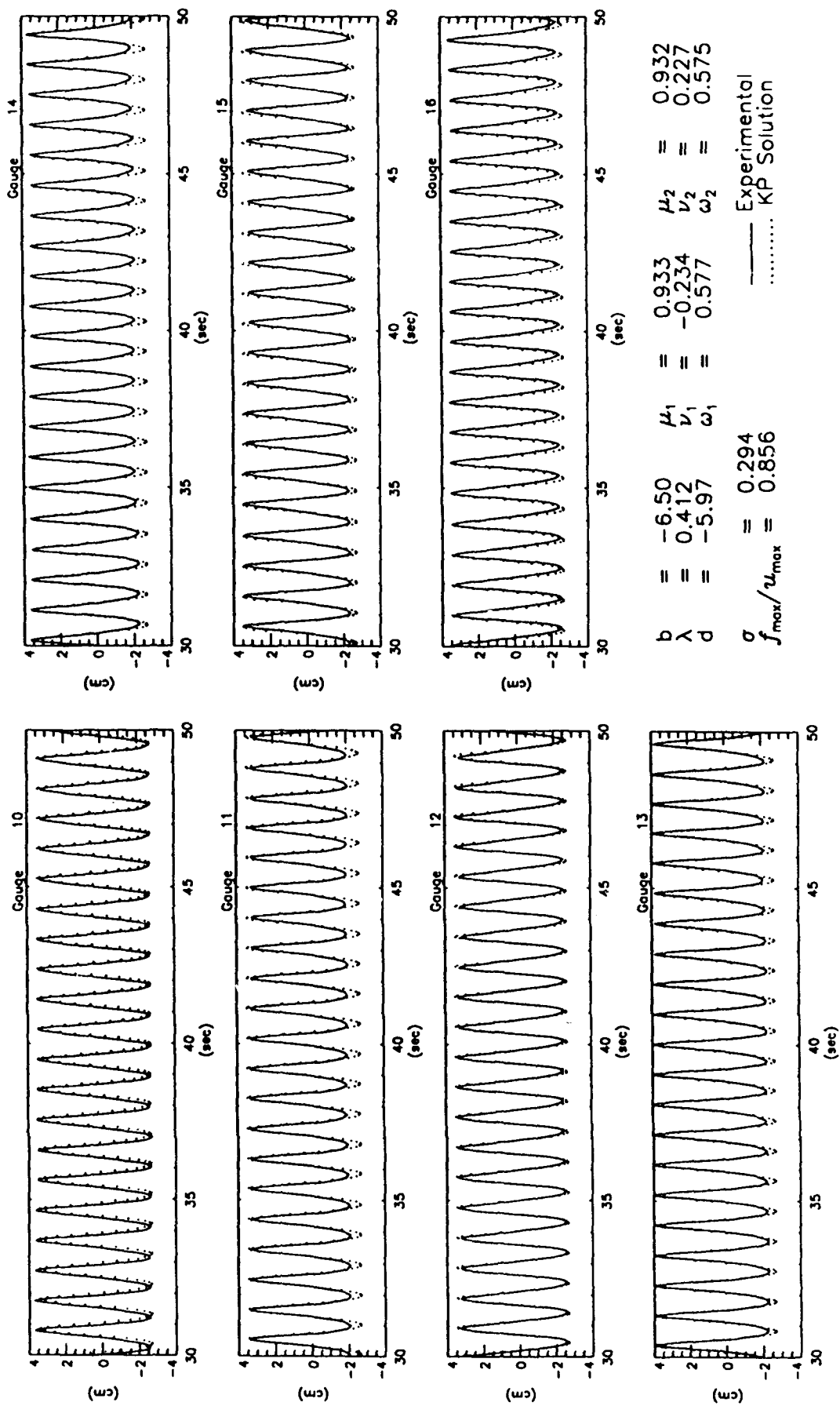


Figure 11b



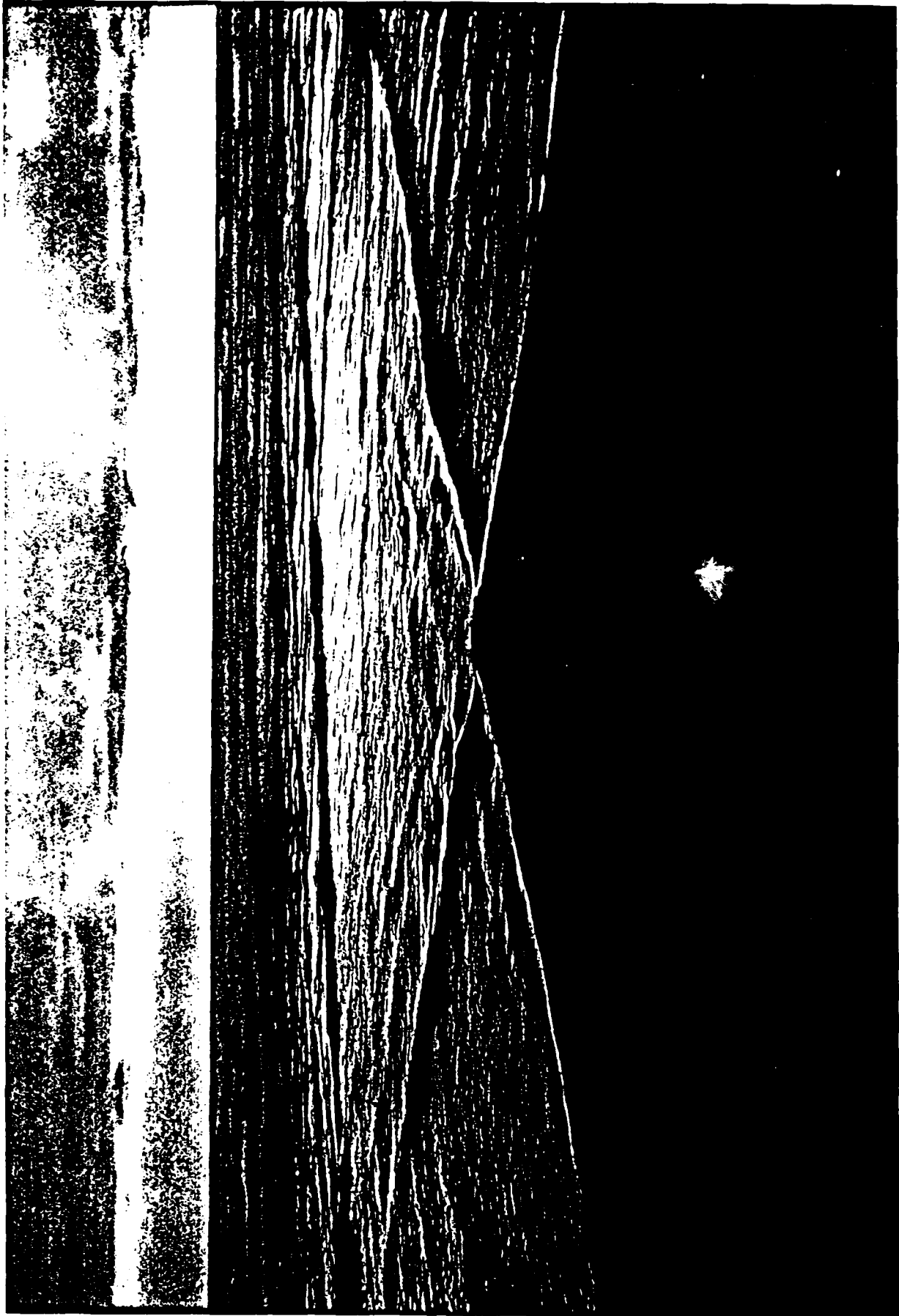


$b = -6.50$        $\mu_1 = 0.933$        $\mu_2 = 0.932$   
 $\lambda = 0.412$        $\nu_1 = -0.234$        $\nu_2 = 0.227$   
 $d = -5.97$        $\omega_1 = 0.577$        $\omega_2 = 0.575$   
 $\sigma = 0.294$   
 $f_{\max}/u_{\max} = 0.856$

— Experimental  
 ..... KP Solution

Figure 11c







## **Appendix B**

**Numerical Chaos, Roundoff Errors, and Homoclinic Manifolds**

**by Mark J. Ablowitz, Constance Schober, and Ben M. Herbst**

*reprinted from Physical Review Letters*  
25 October, 1993

# PHYSICAL REVIEW LETTERS

VOLUME 71

25 OCTOBER 1993

NUMBER 17

## Numerical Chaos, Roundoff Errors, and Homoclinic Manifolds

Mark J. Ablowitz, Constance Schober, and Ben M. Herbst\*

*Program in Applied Mathematics, University of Colorado, Boulder, Colorado 80309*  
(Received 22 March 1993)

The focusing nonlinear Schrödinger equation is numerically integrated over moderate to long time intervals. In certain parameter regimes small errors on the order of roundoff grow rapidly and saturate at values comparable to the main wave. Although the constants of motion are nearly preserved, a serious phase instability (chaos) develops in the numerical solutions. The instability is found to be associated with homoclinic structures and the underlying mechanisms apply equally well to many Hamiltonian wave systems.

PACS numbers: 03.40.Kf, 02.60.-x, 02.70.-c, 02.90.+p

In this Letter we discuss extensive moderate to long time numerical experiments which we have carried out on the focusing nonlinear Schrödinger (NLS) equation with periodic boundary conditions. The NLS equation is a well known Hamiltonian nonlinear wave system which arises in many areas of physics, and is special among such problems since a large class of solutions can be computed via the inverse scattering transform (IST) (e.g., [1]); the NLS equation is said to be "integrable." There are two cases of physical interest—the focusing and defocusing NLS. In the focusing case, when periodic boundary conditions are imposed, the NLS equation has complicated homoclinic structures which under perturbations can produce chaotic dynamics (e.g., [2]). The periodic NLS serves as a useful model describing unstable wave phenomena (e.g., instability in deep water waves) and has been the subject of numerical simulations and laboratory experiments (e.g., [3]).

In our investigations, we employ two numerical schemes which have been used extensively and effectively by researchers studying the NLS equation: (a) the integrable discrete NLS (IDNLS) equation (e.g., [2,4]) and (b) the Fourier split-step (FSS) algorithm (e.g., [5]). The IDNLS equation is an integrable differential-difference equation [4] and is implemented using a high order time discretization. The FSS algorithm, although not integrable, preserves the underlying symplectic structure of the NLS equation and, as such, is in the class of symplectic integrators which have been used as a means of tracking the long time behavior of Hamiltonian systems

(e.g., [6] and references therein). We use two numerical schemes to demonstrate that the results obtained are due to the extreme sensitivity of the periodic focusing NLS equation (in the parameter regime described below) and not the particular details of the numerical schemes employed. To be brief we mainly discuss the calculations of IDNLS. The FSS algorithm yields analogous results.

In earlier work we have shown that initial data which are nearby low dimensional "homoclinic manifolds" trigger numerically induced joint spatial and temporal chaos in nonintegrable numerical schemes at intermediate values of the mesh size [2]. This chaos disappears as the mesh is refined. In this Letter we concentrate on a more troubling aspect of numerically induced chaos. We show that temporal instabilities and chaos can be easily excited by very small perturbations—on the order of roundoff. Although our discussion centers on the NLS equation, we have observed analogous behavior in other problems such as the sine-Gordon and modified Korteweg-de Vries (KdV) equations. We believe that similar results will be found in many other Hamiltonian systems. The NLS equation is an excellent paradigm system to study since we have a great deal of analytical knowledge about this equation, and it is reasonably straightforward to compute.

We begin by summarizing our main observations.

(1) Tiny numerical errors (i.e.,  $10^{-16}$ ) grow rapidly, eventually saturate, but significantly alter the solution after moderate times. For example, spatially even initial values must evolve in an even manner. However, without

imposing evenness as a separate constraint, we find that an odd component is excited and develops into a size comparable with the "main wave." Alternatively, calculating in mathematically but not computationally equivalent ways (e.g., simply by reordering terms in the equation) shows that small errors on the order of roundoff grow rapidly and eventually destroy the "true" solution.

(2) In the Hamiltonian framework, the periodic spectrum (see below) provides the "actions" in an action-angle description and they are constants of the motion. We verify that these constants are preserved by the numerical scheme to very high precision.

(3) The sensitivity is due to the proximity to the underlying homoclinic orbits of the NLS equation. It turns out that for the range of initial values we have chosen the splitting distance between suitable complex eigenvalues of the periodic spectrum is extremely small. Such initial data occur naturally and can be associated with the evolution of nearly elementary plane waves as well as waves which evolve into complicated nonlinear states.

(4) After the growth of the small errors, the corresponding state evolves, but not in a quasiperiodic temporal manner as might have been expected based on the integrability of NLS. The power spectrum of the associated evolution has a slowly decaying "tail" whose size grows as the number of linearly unstable modes (i.e., the suitable complex eigenvalues) increases.

(5) Analogous solutions of the defocusing NLS are stable. They are not sensitive, and we have no difficulty in computing the solution over long times, using either IDNLS or FSS. The power spectrum remains compact and, computationally, the solution is quasiperiodic in time. The inverse scattering theory of the focusing NLS equation with periodic boundary values is significantly different from the defocusing NLS or the KdV equation [7]. Defocusing NLS and KdV are analogous to finite dimensional Hamiltonian systems whose underlying geometric structures are compact tori. In these cases, without homoclinic structures, symplectic integrators are effective.

We consider the NLS equation in the form

$$iu_t + u_{xx} + 2s|u|^2u = 0, \quad (1)$$

where  $s = \pm 1$  (+1 focusing, -1 defocusing), with periodic boundary conditions  $u(x-L/2) = u(x+L/2)$  and initial values  $u(x,0) = g(x)$ . In the focusing case, the plane wave solution,  $u_0(x,t) = a \exp(2i|a|^2 t)$ , is linearly unstable. When considering small perturbations of the form  $u(x,t) = u_0(x,t)[1 + \epsilon(x,t)]$ , one can establish that the perturbation is separated into solutions of the form  $\epsilon(x,t) \propto \exp(i\mu_n x) \exp(\sigma_n t)$ , where  $\mu_n = 2\pi n/L$  and the growth rate  $\sigma_n$  is given by  $\sigma_n = \mu_n \sqrt{4|a|^2 - \mu_n^2}$ . Consequently, the solution is unstable provided  $0 < \mu_n^2 < 4|a|^2$ . The number of unstable modes is the largest integer  $M$  satisfying  $0 < M < |a|L/\pi$ . The fastest growth rate corresponds to a value  $n(\mu_n)$  for which  $\sigma_n$  is maxi-

mal (i.e., closest to  $2|a|^2$ ).

To solve the NLS via IST we use the associated linear scattering problem

$$v_{1x} = -i\lambda v_1 + u(x,t)v_2, \quad (2)$$

$$v_{2x} = i\lambda v_2 - su^*(x,t)v_1, \quad (3)$$

where  $u^*$  is the complex conjugate of  $u$  and the parameter  $\lambda$  is an eigenvalue once boundary values are specified. The spectrum of this linear operator is invariant under the NLS flow and the periodic or antiperiodic eigenvalues  $\{\lambda_i\}_{i=1}^{\infty}$  provide sufficient invariants to establish the integrability of the NLS. The conserved integrals  $\int_{-L/2}^{L/2} T_i \times dx = C_i, i=1,2,\dots$  such as the  $L^2$  norm  $T_1 = |u|^2$ , the momentum  $T_2 = uu_x^*$ , and the Hamiltonian  $T_3 = |u_x|^2 + |u|^4$  are related to the above eigenvalues.

The IDNLS equation is given by [2,4]

$$iu_n + (u_{n+1} + u_{n-1} - 2u_n)/h^2 + s|u_n|^2(u_{n+1} + u_{n-1}) = 0 \quad (4)$$

with  $u_n(t) = u(nh,t)$ ,  $u_{n-N/2}(t) = u_{n+N/2}(t)$ ,  $n=0, 1, \dots, N$  ( $N$  even),  $h=L/N$ ,  $s = \pm 1$ . Since IDNLS is integrable, it possesses the special properties inherent in such systems. As  $h \rightarrow 0$  (4) converges to (1) with accuracy  $O(h^2)$ . In our numerical simulations the time integration of this system of ordinary differential equations is performed by the adaptive Runge-Kutta-Merson routine (D02BBF) in the NAG (numerical algorithms group) software library. We specify an extremely high tolerance to ensure that the results are not dependent upon the time integration. For a description of the FSS algorithm see, for example, [5]. We only remark that in each partial step of the FSS algorithm, the canonical symplectic structure of the NLS equation is preserved, hence the FSS algorithm is a symplectic integrator.

We first discuss our calculations associated with the initial data  $g(x,\epsilon) = a(1 + \epsilon \cos 6\mu x)$ , where  $a=1.5$ ,  $\mu = 2\pi/L$ ,  $L=4\pi\sqrt{2}$ , and  $\epsilon=10^{-12}$ . From the linear theory discussed above, we see that  $g(x,\epsilon)$  contains eight unstable modes. In Fig. 1 we plot the results of IDNLS where we use 512 grid points. In Fig. 1(a) we plot the growth of asymmetry [from (1) note that  $g(x,\epsilon)$  is an even function and should have evolved in an even manner]. The asymmetry is measured by  $\log_{10}|\hat{f}_6 - \hat{f}_{-6}|$  where  $\hat{f}_6$  is the sixth Fourier harmonic [ $u = \sum \hat{f}_m \exp(i\mu_m x)$ ]. The asymmetry grows exponentially fast; for a while the rate of growth is consistent with that predicted by the maximum growth rate of the linearly unstable plane wave (i.e.,  $\sigma_{\max} \approx 4.5$ ). Note that the asymmetry reaches  $O(1)$  before it saturates. In Fig. 1(b) an averaged amplitude of the Fourier transform is depicted. Let  $\hat{u}_j(k)$  be the Fourier transform of  $u_j(t)$  ( $u_j(t)$  is evaluated at every  $\Delta t=0.2$ ); we plot the average:  $\bar{f}_{ave}(k) = \sum_{j=1}^N |\hat{u}_j(k)|/N$  vs  $k$ . We note that the Fourier spectrum has a slowly decaying asymptotic "tail" which is inconsistent with the expectation of a quasiperiodic temporal flow. Note espe-

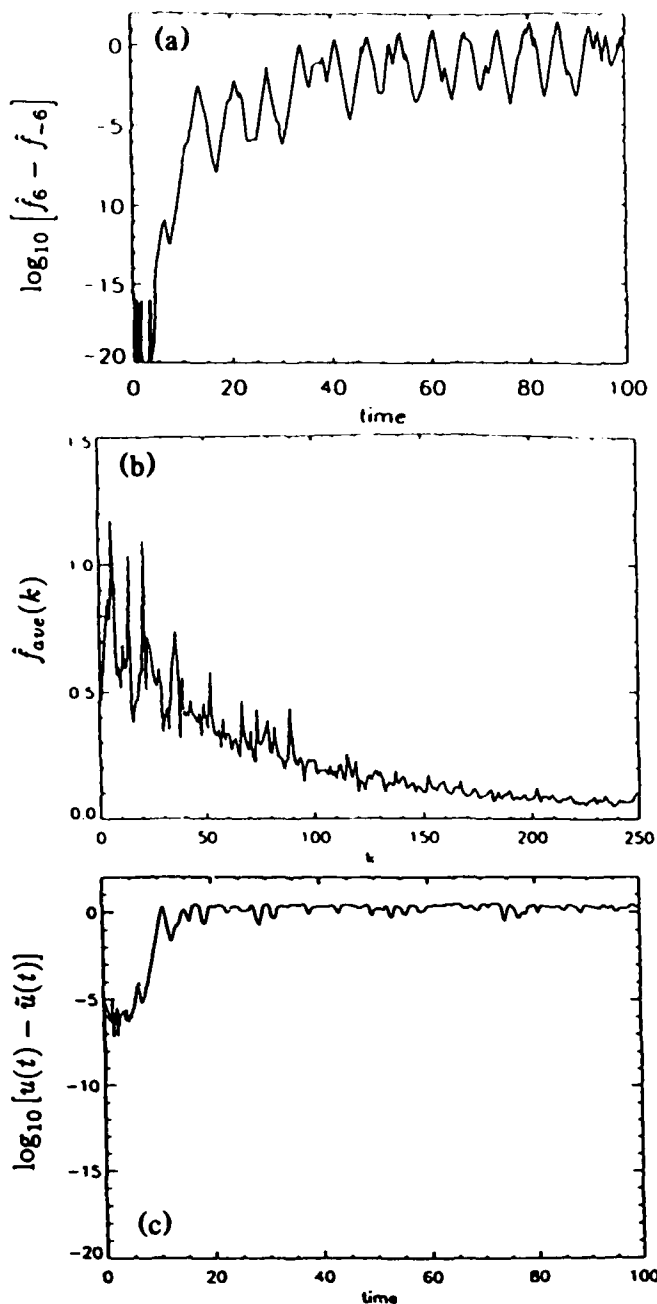


FIG. 1. (a) The asymmetry for IDNLS with  $g(x, \epsilon = 10^{-12})$ . (b) The power spectrum for IDNLS with  $g(x, \epsilon = 10^{-12})$ . (c) The growth in the difference of solutions for IDNLS with  $g(x, \epsilon = 10^{-12})$ .

cially the comparison with the Fourier spectrum of the defocusing NLS equation (Fig. 4). In Fig. 1(c) we plot the logarithm of the averaged difference of two solutions:  $\log_{10} \sum_{j=0}^N |u_j(t) - \tilde{u}_j(t)| / (N+1)$  where  $u_j(t)$  is the solution calculated on  $(-L/2, L/2)$  and  $\tilde{u}_j(t)$  is the solution calculated on  $(0, L/2)$  with symmetry imposed, i.e.,  $u_{-n}(t) = u_n(t)$  (i.e., we calculated on half the lattice). In these calculations the "dominant" complex eigenvalues in the upper half plane were nearly isospectral. The relative change of the first five conserved quantities  $\{C_i\}_{i=1}^5$  was

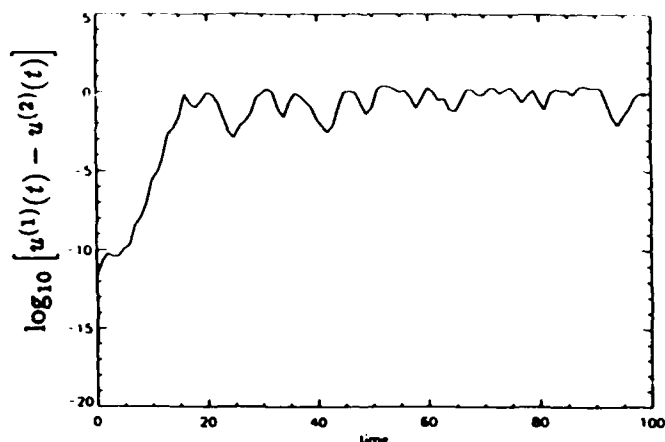


FIG. 2. The growth in the difference of solutions for IDNLS with  $g(x, \epsilon = 10^{-1})$ .

less than 0.01%. As we vary  $\epsilon$  in  $g(x, \epsilon)$  we find similar results; although for significantly larger  $\epsilon$  (e.g.,  $\epsilon = 10^{-1}$ ) it takes longer before the asymmetric perturbations "organize" into rapid growth.

As a crude model of roundoff effects we add to the solution [e.g.,  $g(x, \epsilon)$  with  $\epsilon = 10^{-1}$ ] a small random perturbation at each time step:  $\epsilon_1 r(x, t)$ , where  $0 < r < 1$  ( $r$  is obtained via a random number generator) for a range of  $\epsilon_1$ :  $10^{-8}, 10^{-9}, \dots, 10^{-14}$ . The main features observed before hold: rapid growth of asymmetry, a slowly decaying tail in the power spectrum, etc.

Even if we impose evenness as a constraint, errors on the order of roundoff grow rapidly. For example, consider IDNLS with the initial values  $g(x, \epsilon)$  with  $\epsilon = 10^{-1}$  and  $u_{-n}(t) = u_n(t)$  imposed. We first calculate IDNLS in precisely the way Eq. (4) is specified for  $t=0-100$ —call this solution  $u_n^{(1)}$ . Next we calculate (4) only by distributing the nonlinear terms, i.e., using  $s|u_n|^2 u_{n+1} + s|u_n|^2 u_{n-1}$ . Call this solution  $u_n^{(2)}$ . The logarithm of the averaged difference between the solutions,  $\sum_{j=0}^{N/2} \log_{10} |u_j^{(1)}(t) - u_j^{(2)}(t)| / (N/2+1)$ , grows rapidly (Fig. 2) and, as was the case with asymmetry, the solutions become drastically different. We note that the power spectra of each is broad banded and different from one another as well (not plotted here).

Strongly nonlinear states are unstable and experience the same loss of predictability associated with the above phenomena. For initial data  $g(x, \epsilon)$  with  $\epsilon = 10^{-1}$  we calculate the solution via IDNLS for  $t=0-25$ . At  $t=25$  we are into the fully nonlinear regime and using these values as initial data, we then calculate the two solutions (above):  $u_n^{(1)}(t), u_n^{(2)}(t)$  from  $t=25$  to  $t=225$ . Again (Fig. 3) the solutions deviate significantly, although the growth rate of the difference is smaller than in the previous case. Furthermore, imposing a small random perturbation at each time step (for  $t \geq 25$ ), we find a more rapid growth of the deviation to an  $O(1)$  value.

For defocusing NLS all the difficulties encountered in the focusing case disappear. The power spectrum of a



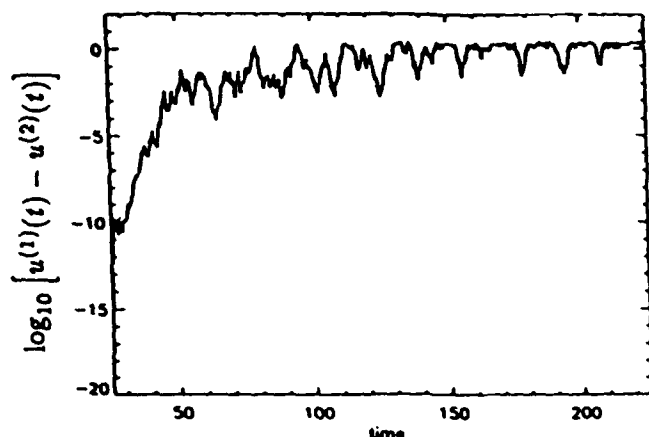


FIG. 3. The growth in the difference of solutions for IDNLS for the nonlinear regime.

typical solution [compare with Fig. 1(b)] is plotted in Fig. 4 where we take  $g(x, \epsilon) = 10^{-1}$ . We observe no growth of asymmetry and both algorithms IDNLS and FSS show no growth in the difference between solutions  $u_n^{(1)}$  and  $u_n^{(2)}$ . Recall that the periodic defocusing NLS does not have homoclinic structures. Small errors do not grow rapidly and IDNLS and FSS are accurate predictors of the long time behavior of the solution.

Since we are studying initial data which are small deviations from a constant, we are able to calculate the periodic or antiperiodic eigenvalues of 2-3 via perturbation analysis (see e.g., [8]). For the initial data  $g(x, \epsilon) = a(1 + \epsilon \cos 6\mu x)$  with  $\epsilon$  small, at leading order there are eight complex eigenvalues which are double points (i.e., eigenvalues of multiplicity 2). Each of these double points corresponds to an unstable mode. We find that under perturbation the double point corresponding to the perturbation  $6\mu$  is split by  $O(\epsilon)$ . The other complex double points, while translating by  $O(\epsilon^2)$  nevertheless have a splitting distance which is smaller than any power of  $\epsilon$ . The splitting distance of the remaining complex eigenvalues is beyond all orders in  $\epsilon$ . Consequently, we are "exponentially close" to the homoclinic manifolds, and small deviations on the order of roundoff can lead to homoclinic crossings and the observed chaos. We have extended our perturbation analysis to predict how modifications in the initial values of earlier numerical simulations [3] could lead to homoclinic crossings under tiny perturbations such as roundoff. We believe that this mechanism can also explain similar difficulties observed, but not understood, in other Hamiltonian equations [9].

The extreme proximity of these data values to the unperturbed homoclinic manifolds prevents us from numerically calculating the "true" solution after moderate time. The calculations are influenced by minuscule errors; computationally the NLS equation is "effectively chaotic" in this range of parameter space despite it being "integrable." Since NLS is so special, we expect an underlying structure to the temporal disorder which may be determined by appropriate statistical studies. Numerical

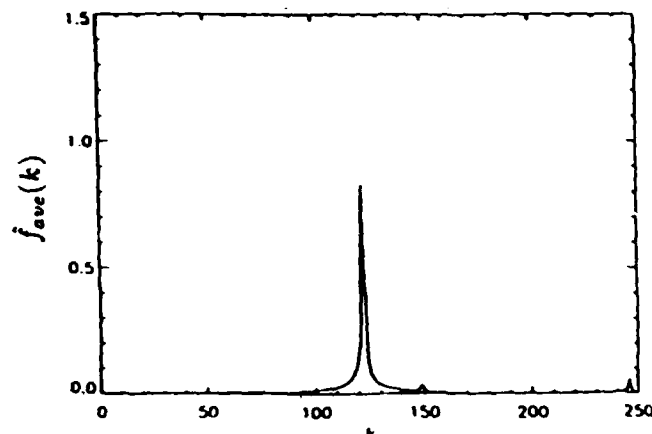


FIG. 4. The power spectrum for defocusing IDNLS with  $g(x, \epsilon = 10^{-1})$ .

simulations which test the stability of small odd perturbations, rearrangements of terms, complex nonlinear states, such as those mentioned in this Letter, can demonstrate the existence of serious underlying numerical instabilities even when known constants of the motion are seemingly well preserved. A more complete account of the work described here will be published in a future paper.

We thank E. Overman for the use of his spectral solver package and R. McLachlan for useful discussions. This work was partially supported by the Air Force Office of Scientific Research under Grant No. AFOSR-90-0039, the NSF Grant No. DMS-9024528, and the Office of Naval Research Grants No. N00014-91-J-4037 and No. N00014-92-J-1274.

\*Present and permanent address: University of the Orange Free State, Bloemfontein 9300, South Africa.

- [1] M. J. Ablowitz and P. A. Clarkson, *Solitons, Nonlinear Evolution Equations and Inverse Scattering* (Cambridge Univ. Press, Cambridge, 1991); A. R. Its and V. P. Kotlanov, Dokl. Akad. Nauk. Ukain. SSR Ser. A, **11**, 965 (1976).
- [2] B. M. Herbst and M. J. Ablowitz, Phys. Rev. Lett. **62**, 2065 (1989); D. W. McLaughlin and C. M. Schober, Physica (Amsterdam) **57D**, 447 (1992); G. Forest, C. Goedde, and A. Sinha, Phys. Rev. Lett. **68**, 2722 (1992).
- [3] H. C. Yuen and W. Fergusen, Jr., Phys. Fluids **21**, 1275 (1978); H. C. Yuen and B. M. Lake, Phys. Fluids **18**, 956 (1975).
- [4] M. J. Ablowitz and J. F. Ladik, J. Math. Phys. **17**, 1011 (1976).
- [5] J. A. C. Weideman and B. M. Herbst, SIAM. J. Numeric. Anal. **23**, 485 (1986).
- [6] P. J. Channel and C. Scovel, Nonlinearity **3**, 231 (1990).
- [7] Y. C. Ma and M. J. Ablowitz, Stud. Appl. Math. **65**, 113 (1982).
- [8] M. J. Ablowitz and B. M. Herbst, in *Proceedings of the CRM, Hamiltonian Systems, Transform Groups and Spectral Transform Methods* (University of Montreal Press, Montreal, 1989).
- [9] B. Fornberg and G. Whitham, Philos. Trans. R. Soc. **289**, 373 (1978).